

**Performance Assessment of Au SERS Substrates Prepared by  
Deposition of Au Nanoparticles on Screen-Printed SiO<sub>2</sub> Particle Films**

by

Raquel E. Simpson

A thesis submitted to the  
School of Graduate and Postdoctoral Studies in partial  
fulfillment of the requirements for the degree of

**Master of Science in Materials Science**

Faculty of Science

University of Ontario Institute of Technology (Ontario Tech University)

Oshawa, Ontario, Canada

February 2023

© Raquel E. Simpson, 2023

## THESIS EXAMINATION INFORMATION

Submitted by: **Raquel E. Simpson**

**Master of Science in Materials Science**

Thesis title:

**Performance Assessment of Au SERS Substrates Prepared by Deposition of Au Nanoparticles on Screen-Printed SiO<sub>2</sub> Particle Films**

An oral defense of this thesis took place on January 24, 2023 in front of the following examining committee:

### **Examining Committee:**

Chair of Examining Committee	Dr. Brad Easton
Research Supervisor	Dr. Liliana Trevani
Research Co-supervisor	Dr. Nisha Rani Agarwal
Examining Committee Member	Dr. Theresa Stotesbury
Examining Committee Member	Dr. Andrew Vreugdenhil
Thesis Examiner	Dr. Olena Zenkina, Ontario Tech

The above committee determined that the thesis is acceptable in form and content and that a satisfactory knowledge of the field covered by the thesis was demonstrated by the candidate during an oral examination. A signed copy of the Certificate of Approval is available from the School of Graduate and Postdoctoral Studies.

## **ABSTRACT**

Surface-enhanced Raman spectroscopy (SERS) is a highly studied technique for simple and rapid trace analysis. Screen-printing, a low-cost fabrication method, has been proposed as a reproducible and affordable approach for the preparation of 3D SERS-active substrates.

In this work, a new solution-based film fabrication method is proposed for the preparation of Au@SiO<sub>2</sub> 3D SERS-active substrates. The procedure involved the synthesis of SiO<sub>2</sub> nanoparticles for the deposition of thin porous SiO<sub>2</sub> films on silica slides using a screen-printing approach. Annealed SiO<sub>2</sub> particle films were subsequently functionalized to promote the adsorption of Au nanoparticles in the SiO<sub>2</sub> matrix. Materials and films were characterized using several methods. The effects of particle properties and paste formulation on the analytical SERS performance of the film were studied using Rhodamine 6G as the target analyte; even though it is difficult to compare between studies, due to the lack of well-established standardization protocols.

**Keywords:** SERS; Au; SiO<sub>2</sub>; Au nanoparticles; Stöber method, Rhodamine 6G

## **AUTHOR'S DECLARATION**

I hereby declare that this thesis consists of original work of which I have authored. This is a true copy of the thesis, including any required final revisions, as accepted by my examiners.

I authorize the University of Ontario Institute of Technology (Ontario Tech University) to lend this thesis to other institutions or individuals for the purpose of scholarly research. I further authorize University of Ontario Institute of Technology (Ontario Tech University) to reproduce this thesis by photocopying or by other means, in total or in part, at the request of other institutions or individuals for the purpose of scholarly research. I understand that my thesis will be made electronically available to the public.

A handwritten signature in black ink, appearing to read 'Raquel E. Simpson', written over a horizontal line.

Raquel E. Simpson

## STATEMENT OF CONTRIBUTIONS

I implemented the methods for the synthesis of materials, preparation of pastes, and methods for the preparation of films. Dhrumik Patel, a research assistant in Trevani's group, performed many technical tasks under my supervision including: the synthesis of solid SiO<sub>2</sub> particles, and the synthesis of textured SiO<sub>2</sub> particles, and the screen-printing deposition of SiO<sub>2</sub> films on silica slides, and preparation of SiO<sub>2</sub> paste.

Dr. Iraklii Ebralidze performed and provided the N<sub>2</sub> adsorption data for solid and textured SiO<sub>2</sub> particles (Chapter 3).

Prof. Theresa Stotesbury provided the HR20 Rheometer required to conduct the viscosity experiments described in Chapter 3. The viscosity experiments were carried out by Prof. Stotesbury's MSc student, Colin Elliot.

TEM images of synthesized Au nanoparticles, solid SiO<sub>2</sub> and textured SiO<sub>2</sub> particles were taken by Dr. Carmen Andrei from the Canadian Centre of Electron Microscopy (CCEM) at McMaster University.

Prof. Franco Gaspari allowed us to use the screen-printing apparatus to create our SiO<sub>2</sub> films. Professors Franco Gaspari, Olena Zenkina, and Brad Easton, provided access to the planetary ball mill used to prepare the pastes.

I hereby certify that I am the sole author of this thesis and that no part of this thesis has been published or submitted for publication. I have used standard referencing practices to acknowledge ideas, research techniques, or other materials that belong to others. Furthermore, I hereby certify that I am the sole source of the creative works and/or inventive knowledge described in this thesis.

## ACKNOWLEDGEMENTS

First of all, I want to express my gratitude to my family and friends for their unwavering support during my graduate studies. Without them supporting me through late hours, I would not have been able to accomplish my goals. Their elation and support were priceless. Additionally, I am very grateful for my new friends made within the Material Science and Graduate School program. They have been an excellent support system, and the bountiful humour add to the welcoming atmosphere.

Without the goodwill of the faculty members who let me use their lab equipment for material characterization and analysis, this research would not have been possible to finish. Having stated that, I would want to thank Dr. E Bradley Easton and Dr. Richard Bartholomew, Dr. Franco Gaspari, Dr. Theresa Stotesbury, Dr. Kevin Coulter, and Dr. Olena Zenkina, Michael Allison, and Genevieve Barnes.

I also want to express my gratitude to Dr. Irakalii Ebralidze for his guidance, kindness, and expertise in using equipment like the SEM, TGA, and BET as well as for doing tests when I was unable to. I also extend a thank you to Colin Elliot for his kind assistance with the viscosity characterisation using the rheometer. I also wish to express my recognition to Edmond Courville for the extensive guidance he has given me especially the for the knowledgeable solutions he has offered to several of my challenges.

My current fellow lab members deserve a special mention. Starting with Muna Abdulaziz, who was always up for a good laugh or to provide sound advice in times of difficulty. My sincere gratitude also extends to our undergraduate student, Dhrumik Patel, for his outstanding effort in the lab during the last year and for assisting me in obtaining

the greatest outcomes. Additionally, I would like to mention the former lab participants who acted as mentors to me when I initially began working on my research. I also thank former lab members who, although were just here momentarily, naturally aided in creating a welcoming atmosphere.

Last but not least, I want to extend my sincerest gratitude to my supervisors, Drs. Liliana Trevani and Nisha Rani Agarwal. I'm grateful for the assignment and chance to work on this project in such a cutting-edge, and expanding sector. They never hesitated in their belief in my capabilities and I've been able to push through these years thanks to their sound advice. They have both served as an inspiration to me in this field, and I have developed numerous talents under their guidance that I will continue to use long after the completion of this project.

## TABLE OF CONTENTS

<b>Thesis Examination Information .....</b>	<b>ii</b>
<b>Abstract .....</b>	<b>iii</b>
<b>Authors Declaration .....</b>	<b>iv</b>
<b>Statement of Contributions.....</b>	<b>v</b>
<b>Acknowledgements .....</b>	<b>vi</b>
<b>Table of Contents .....</b>	<b>viii</b>
<b>List of Tables .....</b>	<b>xi</b>
<b>List of Figures.....</b>	<b>xiii</b>
<b>List of Abbreviations and Symbols .....</b>	<b>xxi</b>
<b>Chapter 1 Introduction .....</b>	<b>1</b>
1.1. Introduction to Vibrational Spectroscopy.....	3
1.2. Infrared (IR) Absorption and Raman Spectroscopy.....	4
1.3. Surface-Enhanced Raman Spectroscopy (SERS).....	9
1.3.1. Theories of SERS Enhancement.....	10
1.4. Progress of SERS-Active Materials.....	17
1.4.1. Synthesis of Metal Nanoparticles in Suspension (Colloidal Systems).....	18
1.4.2. Assembly and Immobilization of Nanoparticles on Solid Substrates (Bottom-up Approach).....	21
1.4.3. Direct Fabrication of Metallic Nanostructures on a Solid Substrate using Thin Film Deposition and Lithography Processes (Top-Down Approach).....	22
1.5. Screen-Printing.....	23
1.6. SERS Characterization .....	24



1.7. Rhodamine 6G as Target Analyte for SERS Characterization.....	27
1.8. Motivation and Thesis Objectives.....	30
<b>Chapter 2 Experimental Section.....</b>	<b>32</b>
2.1. Materials.....	32
2.2. Characterization Techniques.....	32
2.3. Material Synthesis.....	34
2.4. Preparation of 3D SERS Substrates.....	37
2.4.1. Au Nps on Amino-Functionalized Glass Flat Substrates.....	37
2.4.2. Au@SiO <sub>2</sub> /SiO <sub>2</sub> Substrates.....	39
<b>Chapter 3 Nanomaterials and Films Characterization Studies.....</b>	<b>49</b>
3.1 Au Nps and SiO <sub>2</sub> Particles.....	49
3.1.1. SiO <sub>2</sub> Samples Characterization Results.....	49
3.1.2. Au Nps: Particle Size Analysis.....	57
3.2. Rheological Properties of SiO <sub>2</sub> Pastes.....	61
3.3. SiO <sub>2</sub> and Au@SiO <sub>2</sub> Films Physical Characterization Studies.....	64
<b>Chapter 4 Au@s-SiO<sub>2</sub> and Au@t-SiO<sub>2</sub> SERS Evaluation .....</b>	<b>75</b>
4.1. SERS Evaluation of Au@s-SiO <sub>2</sub> /silica and Au@t-SiO <sub>2</sub> /silica substrates.....	75
4.2. SERS Analysis Using R6G - Adsorption time experiments to define the evaluation conditions.....	75
4.3. SERS Substrates Evaluation: Point-To-Point Signal Reproducibility.....	76

4.4. SERS Substrates Evaluation: Signal Repeatability Between Substrates.....	85
4.5. Sensitivity, Limit of Detection and Limit of Quantification Determination for Au@s-SiO <sub>2</sub> and Au@t-SiO <sub>2</sub> .....	87
<b>Chapter 5 Conclusions and Future Work.....</b>	<b>100</b>
<b>Chapter 6 References .....</b>	<b>108</b>
<b>Appendices .....</b>	<b>116</b>
Appendix A .....	116
A1 Monolayer and Multilayer Au/silica films (Method 1).....	116
A2 Surface Topographic images (Profilometry Results).....	118
A3 Permission to Reprint .....	121

## LIST OF TABLES

### CHAPTER 1

<b>Table 1.1.</b> Assignment of R6G vibrational modes.....	30
--	----

### CHAPTER 3

<b>Table 3.1.</b> TGA results of textured and solid SiO <sub>2</sub> synthesized in this work.....	49
--	----

<b>Table 3.2.</b> BET surface area for SiO <sub>2</sub> particles used throughout this study .....	53
--	----

<b>Table 3.3.</b> Composition of the initial SiO <sub>2</sub> paste and with the addition of ethanol.....	64
---	----

<b>Table 3.4.</b> Summary of film topographic morphology for screen-printed two-layer SiO <sub>2</sub> films on glass slides.....	65
---	----

<b>Table 3.5.</b> Summary of film topographic morphology for Au@s-SiO <sub>2</sub> and Au@t-SiO <sub>2</sub> films .....	65
--	----

<b>Table 3.6.</b> EDX composition analysis of 3 sample Au@s-SiO <sub>2</sub> films.....	71
---	----

<b>Table 3.7.</b> EDX composition analysis of 3 sample Au@t-SiO <sub>2</sub> films.....	71
---	----

### CHAPTER 4

<b>Table 4.1.</b> Average absolute intensities of the 613 cm <sup>-1</sup> band measured for a 1 μM R6G solution on multiple Au@s-SiO <sub>2</sub> films.....	79
---	----

<b>Table 4.2.</b> Average absolute intensities of the 613 cm <sup>-1</sup> band measured for a 1 μM R6G solution on multiple Au@t-SiO <sub>2</sub> films.....	79
---	----

<b>Table 4.3.</b> Regression analysis summary for calibration curves collected on both t-SiO <sub>2</sub> and s-SiO <sub>2</sub> systems.....	91
---	----

<b>Table 4.4.</b> Summarized figure of merits acquired by quantitative analysis of the peak height of the 613 cm <sup>-1</sup> band .....	93
<b>Table 4.5.</b> Determination of LoD, LoQ with extrapolated standard deviation values....	95
<b>Table 4.6.</b> Visual limit of detection concentrations determined in literature on Au-based substrate films.....	95
<b>Table 4.7.</b> Reproducibility, Sensitivity, LoD, and LoQ for Au@s-SiO <sub>2</sub> and Au@t-SiO <sub>2</sub> .....	99

## LIST OF FIGURES

### CHAPTER 1

<b>Figure 1.1.</b> Scheme of the potential applications demonstrated for SERS.....	2
<b>Figure 1.2.</b> Potential vibrational modes of molecules.....	4
<b>Figure 1.3.</b> Schematic energy diagram of traditional Infrared absorption, Rayleigh and Raman scattering. Vibrational levels in the ground ( $S_0$ ) and excited ( $S_1$ ) electronic states are indicated as $\nu_i$ . The virtual Raman states are indicated as broken lines.....	5
<b>Figure 1.4.</b> Vibrational modes of water and carbon dioxide represented as (A) spring-and-ball model and (B) electron cloud model .....	8
<b>Figure 1.5.</b> Schematic diagram of the established SERS method .....	11
<b>Figure 1.6.</b> Enhanced localized electric field that occur around the metal nanostructures in the highly localized nano-sized regions within a metal colloid .....	12
<b>Figure 1.7.</b> SERS charge-transfer mechanism for a plasmonic metal object forming a surface complex with a molecule (adsorbate) .....	16

**Figure 1.8.** Timeline of SERS substrate development since discovery (a) The first SERS effect discovered on roughened Ag electrode, (b) SERS of Ag or Au colloids, of (c) silver nanoislands on n-GaAs electrode demonstrating “borrowing” strategy also highlighted by (d) deposited transition metal on roughened Au electrode, (e) single molecule SERS, (f) silica core-Au shell nanoparticle, (g) UPD and redox replacement transition metal on Au nanoparticles, (h) SERS tag, (i) Au core-transition metal shell nanoparticles, (j) Ag film on nanosphere (AgFON) substrates with an alumina layer, (k) silica shell isolated nanoparticles (SHINERS), and (l) graphene shell isolated nanoparticles. Reprinted (adapted) with permission from {Li, J.F., et al., *Core-Shell Nanoparticle-Enhanced Raman Spectroscopy*. Chem. Rev., 2017. **117**(7): p. 5002-5069} . Copyright {2017} American Chemical Society. .... 18

**Figure 1.9.** Simulation of maximum SERS enhancement for planar monolayers of particles with different morphology: Au Nanostars (GNS), Au Nanorods (GNR), Au Nanospheres (GNP). Dashed curves for GNPs and GNSs correspond to 633 nm and 900 nm, respectively, solid curves are derived at 785 nm laser wavelength. Reprinted (adapted) with permission from {Solís, D.M., et al., *Optimization of Nanoparticle-Based SERS Substrates through Large-Scale Realistic Simulations*. ACS Photonics, 2017. **4**(2): p. 329-337}. Copyright {2017} American Chemical Society. The image was obtained from <https://pubs.acs.org/doi/10.1021/acsphotonics.6b00786>. Further permissions related to the material excerpted should be directed to the ACS..... 20

**Figure 1.10.** SERS spectra collected on Au thin films soaked in aqueous R6G solutions from  $1 \times 10^{-4}$  to  $1 \times 10^{-10}$  M. Au film were prepared via pulsed laser ablation using a KrF

excimer laser ( $\lambda = 248$  nm, pulse width 25 ns, repetition rate 10 Hz) in the presence of controlled Argon and pressure value of 100 Pa. Reprinted from Appl. Surf. Sci., **258**, N. R. Agarwal, F. Neri, S. Trussoc, A. Lucotti and P. M. Ossi, Au nanoparticle arrays produced by Pulsed Laser Deposition for Surface Enhanced Raman Spectroscopy, p. 9148-9152, Copyright (2012), with permission from Elsevier..... 28

**Figure 1.11.** Chemical Structure of Rhodamine 6G..... 29

**Figure 1.12.** SERS Spectra of R6G ( $10^{-6}$  M) on different substrates coated with and without Au. Red: Granular Au-sputtered horizontally aligned multiwalled carbon nanotube (Au-HA-CNT) (3000 nm x 50 nm). Reprinted from Nanotechnology, X. N. He, Y. Gao, M. Mahjouri-Samani, P. N. Black, J. Allen, M. Mitchell, et al., *Surface-enhanced Raman spectroscopy using gold-coated horizontally aligned carbon nanotubes*, **23**, p. 205702, 30 April 2012; <http://dx.doi.org/10.1088/0957-4484/23/20/205702> © IOP Publishing. Reproduced with permission. All rights reserved..... 29

## CHAPTER 2

**Figure 2.1.** TGA curves for t-SiO<sub>2</sub> (orange) and s-SiO<sub>2</sub> (blue) powders retrieved under air in this thesis. Flow rate: 10 mL/min. Heating rate: 20 °C/min..... 36

**Scheme 2-1.** Steps for the development of a Au Nps films on glass slides ..... 37

**Scheme 2-2.** Sequential steps involved in the procedure used for Au@SiO<sub>2</sub> nanoparticles using s-SiO<sub>2</sub> and t-SiO<sub>2</sub>..... 40

**Figure 2.2.** Heat treatment applied to the screen-printed SiO<sub>2</sub> films during calcination..... 43

<b>Figure 2.3.</b> TGA and DSC curves obtained under air (20 mL/min) at a temperature scan rate of 20 °C/min for paste containing ethanol, $\alpha$ -terpineol, ethyl cellulose and TiO <sub>2</sub> . Reproduced from Donald McGillivray's Thesis Dissertation, 2013.....	43
<b>Figure 2.4.</b> PEI functionalization of SiO <sub>2</sub> particle and Au Nps adsorption. a) SiO <sub>2</sub> particle film after annealing, b) PEI functionalized SiO <sub>2</sub> particle film, c) adsorption of citrate capped Au Nps on PEI functionalized SiO <sub>2</sub> particle films.....	45
<b>Figure 2.5.</b> UV-Visible spectra of Au Nps solution used in the adsorption step (pink), PEI solution (black line), and solutions containing PEI after each washing step.....	47
<b>Figure 2.6.</b> UV-Visible spectra of Au Np solution used for the preparation of Au@SiO <sub>2</sub> substrates (broken grey line) and after a first (red) and second (blue) adsorption step .....	48

### CHAPTER 3

<b>Figure 3.1.</b> Nitrogen adsorption isotherm for samples of (A) s-SiO <sub>2</sub> and (B) t-SiO <sub>2</sub> at 77 K .....	51
<b>Figure 3.2.</b> BET plot of the nitrogen adsorption on (A) s-SiO <sub>2</sub> on (B) t-SiO <sub>2</sub> at 77 K .....	53
<b>Figure 3.3.</b> (A) TEM images of s-SiO <sub>2</sub> ; Scale bar: 1 $\mu$ m, and (B) particle size distribution analysis of synthesized s-SiO <sub>2</sub> particles using ImageJ software.....	55
<b>Figure 3.4.</b> TEM images of t-SiO <sub>2</sub> ; Scale bars: (A) 1 $\mu$ m, (B) 100 nm .....	56
<b>Figure 3.5.</b> TEM images of (A) s-SiO <sub>2</sub> , (B) t-SiO <sub>2</sub> , Scale bars: (A) 100 nm, (B) 50 nm.....	57



<b>Figure 3.6.</b> (A) TEM image of colloidal Au Nps sized (3-5 nm); Scale bar: 20 nm. (B) PSD analysis of Au Nps in TEM image completed with 53 spherical particles on the ImageJ software .....	58
<b>Figure 3.7.</b> UV-Vis absorption spectrum of aqueous colloidal Au Nps sized 3-5 nm....	59
<b>Figure 3.8.</b> Average particle size for Au Nps in solution obtained using TEM images (pink), and Eq. 3-2 with experimental $C_1$ and $C_2$ parameters (blue) and optimized $C_1$ and $C_2$ constants (green). Particles obtained from three independent synthesis.....	61
<b>Figure 3.9.</b> Viscosity vs. shear rate curve for literature paste systems containing 50 wt% of filler (3 $\mu\text{m}$ $\text{SiO}_2$ , 3 $\mu\text{m}$ silane-functionalized $\text{SiO}_2$ , or a dielectric powder) and the same binding agent (ethyl cellulose), and organic solvent ( $\alpha$ -terpineol) used in this work at 6 wt% and 44% respectively. Reprinted from J. Mater. Process. Technol., <b>197</b> , Lin, H.C., C.; Hwu, W.; Ger, M., <i>The Rheological Behaviors Of Screen-Printing Pastes</i> , p. 7., Copyright (2007), with permission from Elsevier.....	62
<b>Figure 3.10.</b> Viscosity vs. shear rate curve for paste systems prepared with 20% t- $\text{SiO}_2$ particle filler (Orange) and 20% Commercial fumed $\text{SiO}_2$ (0.2-0.3 $\mu\text{m}$ ) (Black).....	63
<b>Figure 3.11.</b> SEM images of the a s- $\text{SiO}_2$ film surface before (left) and after Au adsorption (right).....	67
<b>Figure 3.12.</b> SEM images of the t- $\text{SiO}_2$ film surface before (left) and after Au adsorption (right).....	68
<b>Figure 3.13.</b> Surface morphology and elemental mapping of the Au@s- $\text{SiO}_2$ nanostructured film. Top: (A) Electron SEM image (B) EDX layered image and bottom: corresponding elemental mapping via energy-dispersive X-ray spectroscopy semi-quantitative analysis.....	69

**Figure 3.14.** Surface morphology and elemental mapping of the Au@t-SiO<sub>2</sub> nanostructured film. Top: (A) electron SEM image (B) EDX layered image and Bottom: corresponding elemental mapping via energy-dispersive X-ray spectroscopy semi-quantitative analysis..... 70

**Figure 3.15.** UV-visible absorption spectrum of aqueous colloidal Au Nps (sized 3-5 nm) and a representative Au@SiO<sub>2</sub> film..... 73

#### CHAPTER 4

**Figure 4.1.** (A) SERS signal at 613 cm<sup>-1</sup> vs immersion time for R6G (1 μM R6G) and (B) SERS spectra for R6G (1 μM) at increasing immersion times (10, 30, 60, 120, and 300 s)..... 77

**Figure 4.2.** SERS spectra collected for 1 μM of R6G at 8 randomly selected sites close to the centre of a representative Au@s-SiO<sub>2</sub> film. Acquisition parameters: 50 mW of 532 nm excitation at 0.5% power, and 10 second integration for 10 accumulations 50x magnification..... 78

**Figure 4.3** SERS spectra collected for 1 μM of R6G at 8 randomly selected sites close to the centre of a representative Au@t-SiO<sub>2</sub> film. Acquisition parameters: 50 mW of 532 nm excitation at 0.5% power, and 10 second integration for 10 accumulations 50x magnification..... 78

**Figure 4.4.** SERS mapping of R6G (10 μM) on (A) Au@s-SiO<sub>2</sub> and (B) Au@t-SiO<sub>2</sub> substrates. Analysis was completed on an area of 21 x 21 μm<sup>2</sup>..... 81

**Figure 4.5.** 21 x 21  $\mu\text{m}$  square area SERS mapping of R6G coated on Au@s-SiO<sub>2</sub> film SERS substrates, at the associated concentration. Analysis was completed to the absolute intensity of the 613  $\text{cm}^{-1}$  R6G band. 441 spectra were obtained with 1  $\mu\text{m}$  steps, 1 accumulation, and 10 second exposure time ..... 82

**Figure 4.6.** SERS Mapping of R6G coated on Au@t-SiO<sub>2</sub> film SERS substrates: (left) 0.1 and 1  $\mu\text{M}$  on a 21 x 21  $\mu\text{m}^2$  area (1  $\mu\text{m}$  steps, 1 accumulation) and (right) 0.5  $\mu\text{M}$  on a 50 x 50  $\mu\text{m}^2$  area (5  $\mu\text{m}$  steps, 4 accumulations) 1 second exposure time. Analysis was completed to the absolute intensity of the 613  $\text{cm}^{-1}$  R6G band..... 84

**Figure 4.7.** Waterfall SERS spectra of 1  $\mu\text{M}$  R6G from 8 sample films of Au@t-SiO<sub>2</sub> (A), and Au@s-SiO<sub>2</sub> (B). Each spectrum is an average of 8 measurements taken on each film. Spectra obtained with following Raman parameters: 50 mW of 532 nm excitation at 0.5% nominal power and 10 second integration time for 10 accumulations 50x magnification..... 86

**Figure 4.8.** Comparison of SERS spectra collected with the Au@t-SiO<sub>2</sub> (orange) and Au@s-SiO<sub>2</sub> (blue) systems at 0.1  $\mu\text{M}$ . Black line corresponds to the Au@t-SiO<sub>2</sub> film. The SERS intensity scale bar is 500 A.U. Laser  $\lambda$ : 532 nm; laser power: 25 mW..... 88

**Figure 4.9.** (A) SERS spectra of R6G measured at increasing concentrations (0.1  $\mu\text{M}$  to 1000  $\mu\text{M}$ ) on Au@s-SiO<sub>2</sub> films. Calibration curve for R6G analyzed on Au@s-SiO<sub>2</sub> films at a concentration range of 1000  $\mu\text{M}$  to 1  $\mu\text{M}$  obtained using (B) Peak height at 613  $\text{cm}^{-1}$  and the respective (C) peak integration area ..... 90

**Figure 4.10.** (A) SERS spectra of R6G measured at increasing concentrations (0.05  $\mu\text{M}$  to 10  $\mu\text{M}$ ) on Au@t-SiO<sub>2</sub> films. Calibration curve for R6G analyzed on Au@t-SiO<sub>2</sub> films at a concentration range of 0.1  $\mu\text{M}$  to 10  $\mu\text{M}$  obtained using (B) Peak height at 613  $\text{cm}^{-1}$  and the respective (C) peak integration area ..... 91

**Figure 4.11.** Average roughness as a function of SERS intensity of band at 1649 and 613  $\text{cm}^{-1}$  on Au@t-SiO<sub>2</sub> and Au@s-SiO<sub>2</sub> ..... 97

## CHAPTER 5

**Figure 5.1.** (A) Typical 3D scanned surface topography of a Au@s-SiO<sub>2</sub> film (250 x 200  $\mu\text{m}$  square area compared to (B) a characteristic SEM image of a Au@s-SiO<sub>2</sub> film (25 x 17  $\mu\text{m}$  square area), and resulting (C) SERS map of a smaller area (21 x 21  $\mu\text{m}$  square area) indicated by the black square..... 103

**Figure 5.2.** Au@t-SiO<sub>2</sub> film displayed as (A) a SEM image (25 x 17  $\mu\text{m}$  square area), and (B) a typical SERS map of a similar area (21 x 21  $\mu\text{m}$  square area) from this substrate. (C) A 3D scanned surface topography image of Au@t-SiO<sub>2</sub> (4000 x 4000  $\mu\text{m}$ ), and size comparison (orange box within) to the a (D) SEM image obtained at a larger scale (965 x 680  $\mu\text{m}$ )..... 104

**Figure 5.3.** SEM images of (Left) Au@s-SiO<sub>2</sub> and (Right) Au@t-SiO<sub>2</sub>; Scale bar: 10  $\mu\text{m}$ ..... 105

## LIST OF ABBREVIATIONS AND SYMBOLS

A	The geometrical area of the laser spot
AEF	Analytical Enhancement Factor
ANOVA	Analysis of Variance
$A_{\text{spr}}$	SPR absorbance of the nanomaterial
Au	Gold
A.U.	Arbitrary Units
Au@s-SiO <sub>2</sub>	Au Nps layer-solid SiO <sub>2</sub> substrate
Au@t-SiO <sub>2</sub>	Au Nps layer-textured SiO <sub>2</sub> substrate
BET	Brunauer-Emmett-Teller
c	The speed of light
C <sub>1</sub> , C <sub>2</sub>	Empirical parameters
$c_{\text{Au}}$	The initial concentration of Au in a synthetic procedure
CM	Chemical mechanism
CMC	Critical Micellar Concentration
C <sub>RS</sub>	Analyte concentration during normal Raman spectroscopic analysis
C <sub>SERS</sub>	Analyte concentration during SERS analysis
CT	Charge-Transfer
CTAB	Cetrimonium Bromide
CVD	Chemical Vapour Deposition
d	Estimated diameter size of the Au nanoparticles
DSC	Differential Scanning Calorimetry
e	Electron charge
E <sub>0</sub>	Incident electromagnetic field
E <sub>loc</sub>	Enhanced localized Field
EM	Electromagnetic mechanism

$G_{SERS}^{EM}$	Theoretical electromagnetic SERS enhancement
$h$	Planck's constant
HOMO	Highest Occupied Molecular Orbital
ICP-MS	Inductively Coupled Plasma - Mass Spectrometry
$I_{SERS}$	Overall SERS enhancement intensity
IR	Infrared
$I_{Raman}$	Raman scattering intensity
IUPAC	International Union of Physical and Applied Chemistry
$\log(b)$	y-intercept of a log-log regression curve
LSPR	Localized Surface Plasmon Resonance
LUMO	Lowest Occupied Molecular Orbital
$m$	Slope of a log-log regression curve
m-SiO <sub>2</sub>	Commercial mesoporous SiO <sub>2</sub> particles
$m_e$	Effective mass of electrons
$M_{Loc}^Z$	Enhanced Radiated power as a result of a localized electromagnetic field
$N$	Electron density of the metal
$N_{cast}$	The number of molecules initially cast on a SERS substrate or during a Raman analysis
$N_E$	Effective number of probed molecules during SERS/Raman analysis
$N_{ps}$	Nanoparticles
$N_{Raman}$	Number of molecules present in the scattering volume, contributing to a normal Raman signal
$N_{SERS}$	Number of molecules adsorbed on the SERS substrate surface
$P$	Power radiated by a dipole
$P/P_0$	Relative pressure
PEI	Polyethyleneimine
PEI@SiO <sub>2</sub>	Polyethyleneimine functionalized SiO <sub>2</sub>

PSD	Particle Size Distribution
PVD	Physical Vapour Deposition
q	Normal coordinates of atomic motion during vibration
R <sup>2</sup>	Correlation coefficient
Ra	Arithmetic average deviation
% RSD	Coefficient of variation/ Percent Relative Standard Deviation
S	Geometrical area of the analyte layer on a SERS substrate or during Raman analysis
s-SiO <sub>2</sub>	Solid surface SiO <sub>2</sub> particle
$\overline{S}_{bl}$	Average signal in the blank
s <sub>bl</sub>	Standard deviation in the signal of several blank measurements
SD <sub>0</sub>	Extrapolated value of standard deviation at 0 M of analyte
SEM	Scanning Electron Microscopy
SERS	Surface-enhanced Raman Spectroscopy
SERS-EF	Surface-enhanced Raman Spectroscopy-Enhancement Factor
S <sub>m</sub>	Signal obtained at the LoD
SP	Surface Plasmons
sr	Steradian
SSEF	SERS Substrate Enhancement Factor
t-SiO <sub>2</sub>	Textured surface SiO <sub>2</sub> particle
TEM	Transmission Electron Microscopy
TEOS	Tetraethyl orthosilicate
TGA	Thermogravimetric Analysis
v/v	Volume of solvent/Volume of solution
WLI	White Light Interferometry
wt%	Weight%
λ	Wavelength

$\alpha_m$	Molecular polarizability
$\sigma_r$	Cross-section of solid angle
$\Omega$	Solid angle for collection
$\mu$	Induced molecular dipole moment
$\nu_R$	Raman frequency
$\nu_{\text{vib}}$	Scattered frequency
$\nu_{\text{inc}}$	Incident frequency of the laser
$\epsilon_0$	Dielectric constant
$\epsilon_\infty$	High frequency dielectric constant



## Chapter 1: Introduction

Surface-enhanced Raman spectroscopy (SERS) is a label-free vibrational technique that utilizes inelastically scattered radiation energy by molecules for qualitative detection [1]. As discussed in the following section, SERS, like conventional Raman, can provide unique vibrational information from scattered radiation by a particular analyte [2-4]. The difference between the two methods is the greatly enhanced signal observed due to analyte adsorption on SERS-active surfaces. This is expected to be realized on substrates with texturized or roughened, nanostructured noble metals, such as Au, Ag, and Cu [3]. This type of substrate and metal nanoparticles (Nps), efficiently generate localized surface plasmon excitation sites within 1-2 nm inter/intra-particle gaps, which are essential to the SERS effect [5, 6].

Like Raman, some advantages of SERS include facile sample preparation and manipulation, rapid analysis time, and in situ analyte identification [7]. However, the high sensitivity of SERS enables multicomponent analysis at the single-molecule level [8]. Articles about the development and optimization of SERS substrates have grown significantly in the last 20 years [9-13]. Innovative SERS substrate designs have been developed to efficiently detect many chemical and biological species in applications such as environmental analysis [14], pharmaceutical detection [8, 15], biochemistry [16, 17], forensic chemistry [18], and food safety [19] (Figure 1.1).

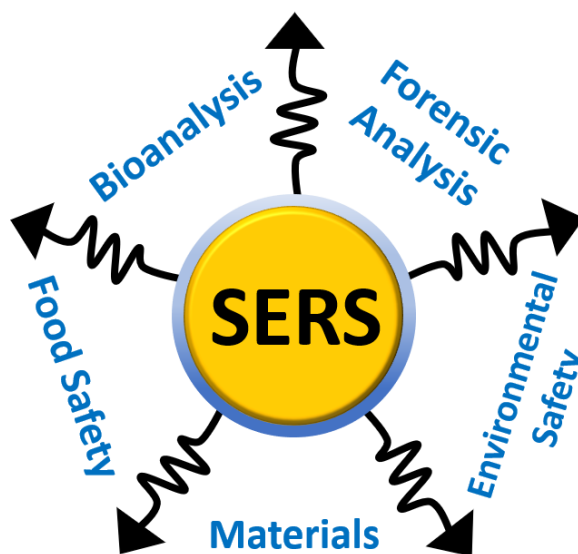


**Figure 1.1.** Scheme of the potential applications demonstrated for SERS.

Despite the growing success of the SERS field and the implementation of low-cost substrates that have been one key aspect that is turning SERS into a more accessible tool for chemical analysis, there is still a significant hindrance to adopting this technique as a standard quantification tool in analytical laboratories [6, 20]. A central issue is the lack of SERS intensity reproducibility amongst substrates [20-22]. It is important to note that SERS is a morphologically-dependent technique and structural properties play a crucial role in the electromagnetic enhancement. Furthermore, macroscale inhomogeneity can potentially alter the SERS enhancement factor (SERS-EF) [23]. For this reason, several methods have been explored for the preparation of thin films including pulsed laser ablation, physical vapour deposition, chemical vapour deposition, nanolithography, layer-by-layer deposition, electrodeposition etc. [24].

## 1.1. Introduction to Vibrational Spectroscopy

Absorption spectroscopy is based on the absorption of electromagnetic radiation by atoms and molecules. Two extensively used absorption spectroscopic methods in qualitative and quantitative analysis are UV-visible and infrared absorption spectroscopies; the former is associated with electronic transitions, and the latter involves energy transitions between vibrational energy levels. However, the energy of infrared radiation can excite vibrational and rotational transitions, but it is insufficient to excite electronic transition levels. The number of ways a molecule can vibrate is related to the number of bonds (atoms), and it is given by  $3N-6$  ( $3N-5$  for linear molecules) with  $N$  equal to the number of atoms in the molecule [8]. Therefore, the number of vibrational modes is generally large, for instance for a simple non-linear molecule like  $\text{H}_2\text{O}$  with only three atoms, the number of fundamental vibrational modes is equal to three, bend, symmetric stretch and antisymmetric stretch bands centered at  $1595\text{ cm}^{-1}$ ,  $3657\text{ cm}^{-1}$ , and  $3756\text{ cm}^{-1}$ , respectively.

Figure 1.2 illustrates common vibrational modes found in polyatomic molecules. Stretching (symmetric and asymmetric) defined as a periodic movement along the bond axis with increasing and decreasing bond length, in-plane bending (rocking and scissoring) defined as changes of bond angles while bond lengths remain almost fixed, and out-of-plane bending (twisting and wagging).

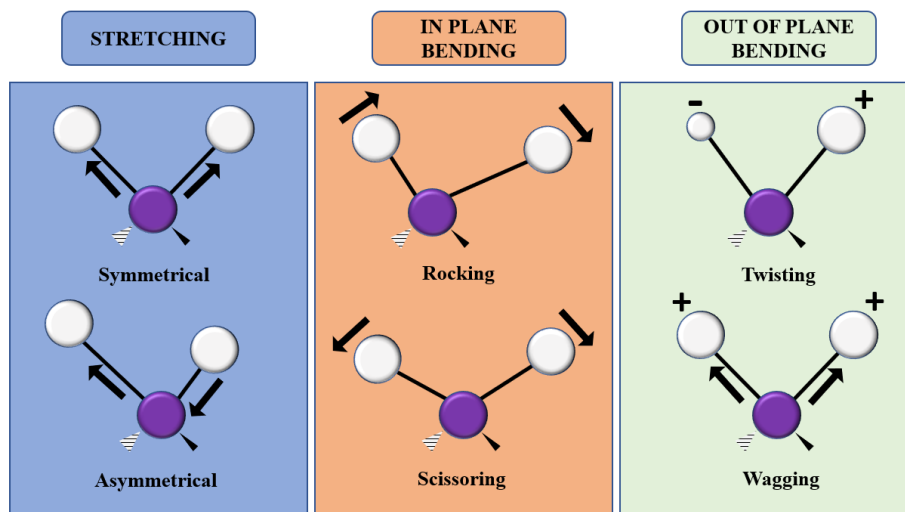


**Figure 1.2.** Potential vibrational modes of molecules

The vibrational degrees of freedom can be used to estimate the number of vibration modes; this does not indicate the IR or Raman active modes in a molecule, as it will be discussed in the following section, as molecule-electromagnetic interaction proceeds differently in both techniques giving very distinct patterns, essentially providing complementary spectra of molecular vibrations.

## 1.2. Infrared (IR) Absorption and Raman Spectroscopy

Raman and Infrared (IR) absorption spectroscopy are two non-destructive techniques extensively used for solving analytical problems, including structural analysis and molecular identification. Infrared and Raman spectroscopy are complementary techniques with different selection rules. Infrared spectroscopy is associated with vibrational transitions in molecules and materials via dipolar interaction with electromagnetic radiation [1]. In contrast, Raman spectroscopy is associated with the inelastic scattering of monochromatic light, as illustrated in Figure 1.3, where the virtual states are short-

lived states, not real vibrational states belonging to the molecule. These states are generated upon laser interaction with electrons that causes polarization.

As shown in Figure 1.3, in the case of Raman, depending on the type of interaction between the incident radiation and matter (elastic or inelastic), the energy of the scattered photon could be equal to that of the incident light (Rayleigh scattering—elastic interaction), or lower or higher than that of the incident light due to inelastic interaction resulting in Stokes bands for which the frequency of the scattered photon,  $\nu_{\text{vib}}$ , is smaller than the frequency of the incident light,  $\nu_{\text{inc}}$ , and anti-stokes Raman bands, for which the inverse is valid.

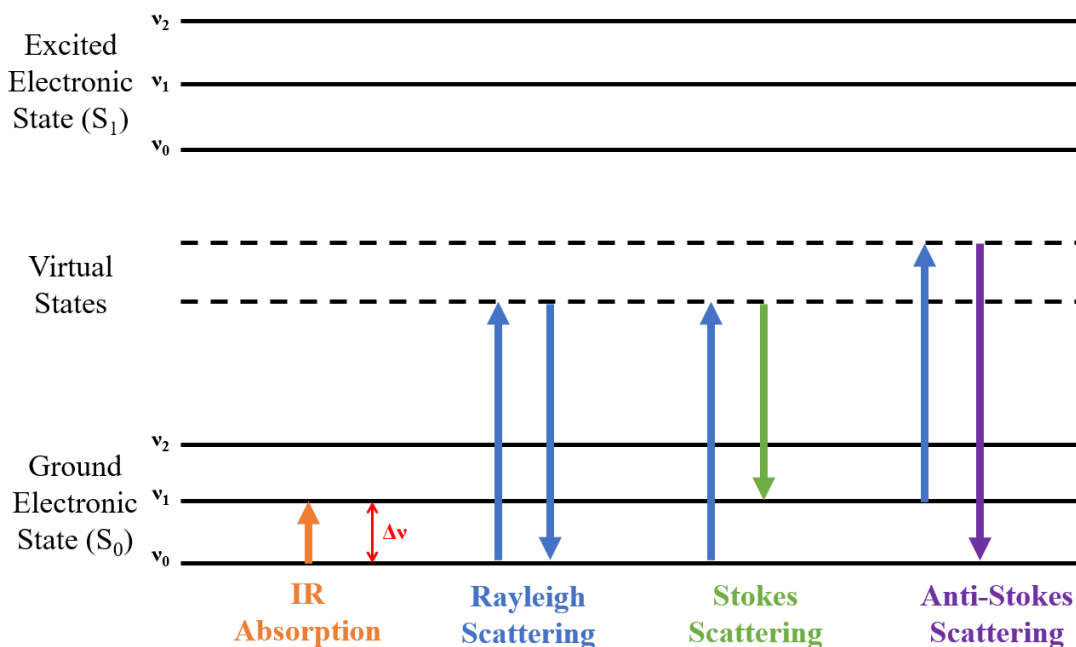


**Figure 1.3.** Schematic energy diagram of traditional Infrared absorption, Rayleigh and Raman scattering. Vibrational levels in the ground ( $S_0$ ) and excited ( $S_1$ ) electronic states are indicated as  $\nu_i$ . The virtual Raman states are indicated as broken lines.

With  $h$ , representing Planck's constant, the Stokes and anti-Stokes Raman shift are therefore equal to:

$$\text{Stokes Raman band: } \Delta E = h (\nu_{\text{inc}} - \Delta \nu) \quad (1-1)$$

Energy from incident laser photons is transferred to the analyte, resulting in emitted photons that are shifted to lower frequencies.

$$\text{Anti-Stokes Raman band: } \Delta E = h (\nu_{\text{inc}} + \Delta \nu) \quad (1-2)$$

Energy from the analyte is transferred to the incident laser photons.

The inelastic scattering induces three dipole components;  $\mu_{\text{ind}}(\nu_{\text{inc}})$ ,  $\mu_{\text{ind}}(\nu_{\text{inc}} - \nu_{\text{vib}})$  and  $\mu_{\text{ind}}(\nu_{\text{inc}} + \nu_{\text{vib}})$  where each corresponds to Rayleigh, Stokes and Anti-Stokes, respectively [14, 15].

The intensity of the Raman scattering bands is inversely proportional to the fourth power of the excitation wavelength ( $I \propto 1/\lambda^4$ ), therefore, the signal intensity strongly depends on the laser excitation wavelength.

For a given molecule, IR radiation interaction is possible if the electric field vector oscillates with a frequency matched to the molecular dipole moment. If  $q$ , represents the normal coordinates of atomic motion during vibration, IR activity and Raman activity can be described by Eq. 1-3 and Eq. 1-4, respectively. If the corresponding normal vibration by the molecule modifies the molecular dipole moment,  $\mu$ , then it is said to be IR active and will generate an absorption band in the IR region [25]:

$$\left(\frac{\partial\mu}{\partial q}\right)_o \neq 0 \quad (1-3)$$

Here, the subscript o, denotes that the derivative is taken at equilibrium configuration. A Raman-active molecular vibration will cause a modulation to the molecular polarizability [25]:

$$\left(\frac{\partial\alpha}{\partial q}\right)_o \neq 0 \quad (1-4)$$

Therefore, in a molecule with a centre of symmetry, the Raman active modes are IR inactive, and vice versa); the rule of mutual exclusion. A linear diatomic molecule, has one vibration by fact. Using O<sub>2</sub> as an example, the molecule is symmetrical and has an intense Raman band, while this vibration is not observed in the IR spectrum (Figure 1.4). Spring and ball representation of triatomic molecules demonstrate 3 modes of vibration: symmetrical stretch, bending or deformation, and asymmetrical stretch. The symmetric stretches exhibited by CO<sub>2</sub>, result in a bond stretch for both bonds that allows for both to be polarizable, changing the overall molecular polarizability. The H<sub>2</sub>O molecule exhibits a symmetric stretch that results in a weak overall change in the molecular polarizability, because there is stretching occurring in opposite directions essentially limiting the polarizability change, hence no Raman-active band.

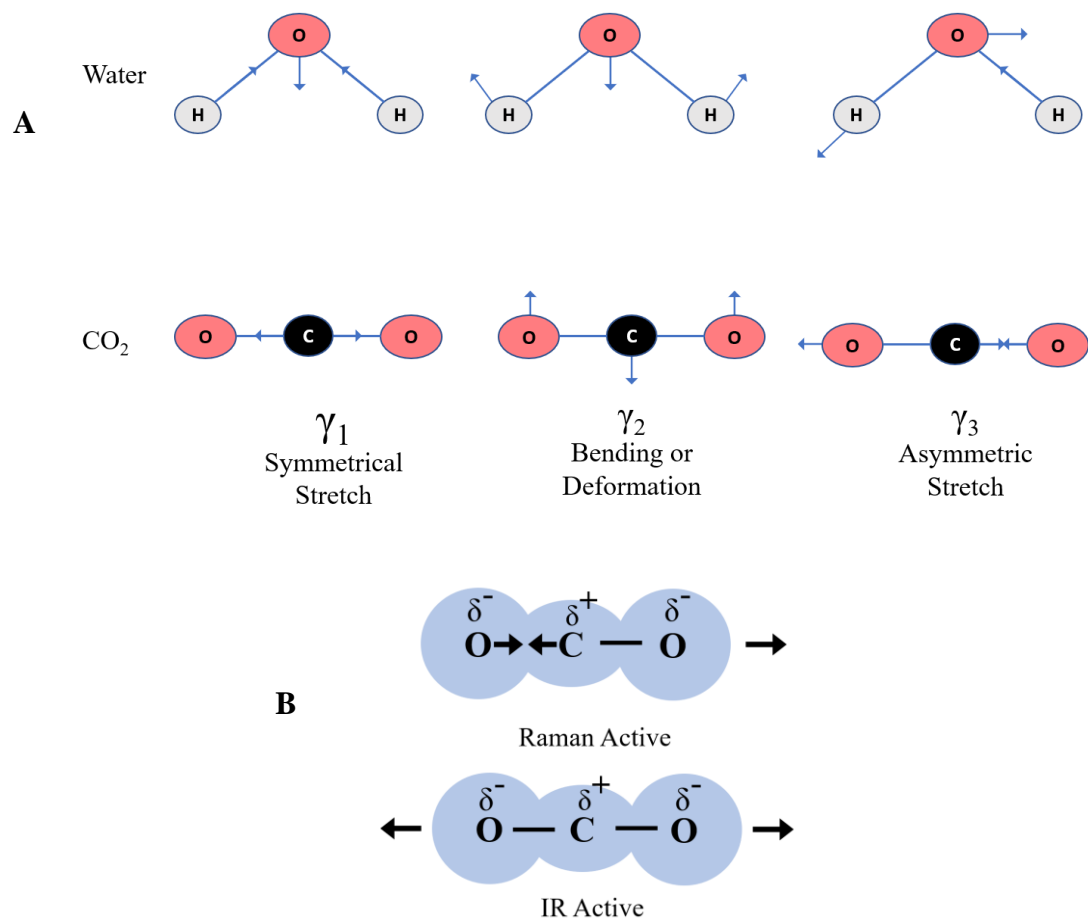


**Figure 1.4.** Vibrational modes of water and carbon dioxide represented as (A) spring-and-ball model and (B) electron cloud model

Raman and IR spectroscopy are both used in a wide range of applications. Despite the fact that IR spectroscopy is more common for molecular identification studies, Raman spectroscopy is advantageous as sample preparation is non-tedious and analysis can take place without interference from water, like it is the case in IR spectroscopy where the broad band of water interfere with other bands [7].

The efficiency of any scattering process is dependent on the scattering cross-section, which depends on the vibrational mode of the analyte molecule. This varies amongst differing scattering methods, and in general, Raman signals exhibit relatively



low cross-sections per molecule. The typical range of cross-sections ascertained with Raman ( $\sim 10^{-31}$  to  $10^{-29}$   $\text{cm}^2 \text{sr}^{-1}$ ) is substantially lower than that of fluorescence spectroscopy ( $\sim 10^{-16}$   $\text{cm}^2 \text{sr}^{-1}$ ) explains why the Raman scattered signals are intrinsically weak for most molecules [26]. One photon will experience inelastic scattering out of  $10^6$  -  $10^9$  incident photons in Raman spectroscopy, highlighting how weak Raman signals can be [27].

### **1.3. Surface-Enhanced Raman Spectroscopy (SERS)**

Surface-enhanced Raman Spectroscopy enhances the Raman signals of target analytes to single molecule detection. The technique is gaining momentum, and applications are now expanding to numerous fields [8]

The first recorded observation of SERS occurred in 1974 by Fleischmann [28] and the SERS phenomenon was first recognized in 1977 by Jeanmaire and Van Duyne [29]. Jeanmarie and Van Duyne studied the Raman sensitivity of aromatic amines adsorbed on the surface of roughened silver electrodes as a function of applied electrode potential. The experiment confirmed the role of the surface properties on the enhancement of the “weak” Raman scattering signal for molecules with a small Raman cross-section. SERS possesses all of the advantages of Raman spectroscopy while enabling sensitive detection of ultra-low concentrations, exceeding the limitations of Raman spectroscopy. This enhancing effect of SERS is dependent on the characteristics of the surface and requires the adsorption of the analytical molecule onto that surface. Generally, efficient SERS requires a nanostructured surface composed of one of the noble metals; Au, Ag, and Cu

due to their highly plasmon-resonant optical scattering properties in the visible region of the electromagnetic spectrum.

### **1.3.1. Theories of SERS Enhancement**

Signal amplification occurs on a SERS-active surface which is either a metal or a semiconductor. A plasmonic surface bears the localized surface plasmon resonance (LSPR) properties which will enable the underlying electromagnetic mechanism (EM) that contributes to the resulting Raman enhancement. The extent of the enhancement is largely dependent on the morphological properties and positioning of the metallic nanostructures along the substrate surface [6]. A chemical mechanism (CM) is also accepted as an underlying contribution to the overall enhancement, mainly in the case of metal oxide semiconductors, and materials with two-dimensional morphology can be employed alternatively to noble metals [30, 31]. These mechanisms will be explained with more detail in following sections. Considering that the CM contributes a maximum of 2-3 orders of magnitude towards the enhancement, and EM has demonstrated over 10 orders, it can be concluded that the other materials may not be as effective in comparison [32].

As shown in Figure 1.5, analyte detection by SERS is significantly impacted by the substrate roughness, molecular adsorption on it, the incident laser wavelength, and the analyte-substrate interaction [13].



**Figure 1.5.** Schematic diagram of the established SERS method

Currently, the EM and the CM are both considered the dominating underlying mechanisms behind the observed Raman enhancement. The fundamentals associated to both mechanisms are discussed below.

### *Electromagnetic enhancement mechanism*

Enhancement derived from the EM, is mainly applicable to the explanation of enhancement on metal substrates. In metals, the collective oscillations of the conduction band electrons are known as surface plasmons (SPs); SPs are the key driving force of the SERS EM [33]. Under resonance excitation, interaction with the incident oscillating electromagnetic field and the conduction band electrons will activate charge separation; the diagram in Figure 1.6 represents this phenomenon [8].

Figure 1.6 illustrates the dipole-dipole oscillations regulated by coulombic interactions between the high density of electrons in the metal nanoparticles that induce localized resonance LSPRs which can be defined under random phase approximation:

$$LSPR = \frac{4\pi N e^2}{\epsilon_{\infty} m_e} \quad (1-5)$$

where  $N$ , represents the electron density of the metal,  $\epsilon_\infty$  refers to the high frequency dielectric constant of the media,  $e$  and  $m_e$ , are the electron charge and the effective mass of electrons, respectively [8]. The LSPR mode can be excited by incident light, at resonance frequency, resulting in EM enhancement (Figure 1.6). For Au, Cu, and Ag this is observed in the visible or near UV region where local dipoles can be induced.

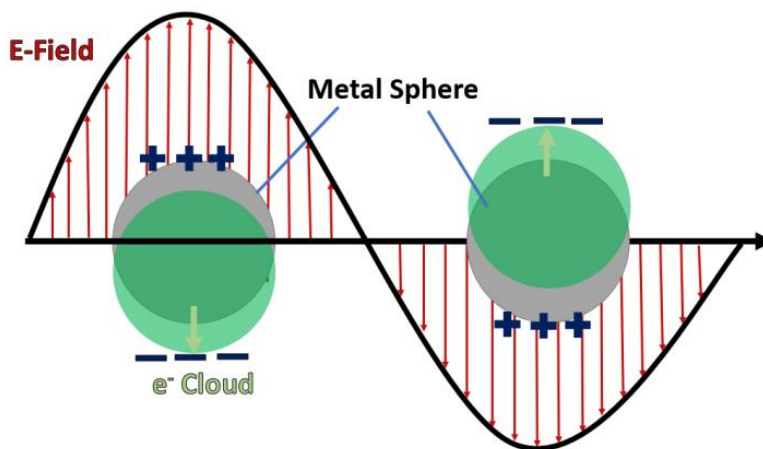


**Figure 1.6.** Enhanced localized electric field that occur around the metal nanostructures in the highly localized nano-sized regions within a metal colloid.

Maximum electromagnetic field enhancement is found where LSPR are prominent and this is in narrow-gap regions also known as “hot-spots” found between nanometallic objects or in junctions on them. Intense Raman signal amplification is produced for molecules at or in proximity to these nano-sized special sites. Currently, justified attention is put towards optimizing the generation of hot spots with a uniform distribution on a SERS substrate surface as it is a priority in SERS sensor fabrication [23, 34].

The development of efficient SERS substrates depends on good knowledge of the strong coupling between the plasmon and molecular exciton resonances. The following equations have been used for EM enhancement factor (EF) in computational calculations

such as finite-difference time-domain (FDTD) and COMSOL simulation to determine the enhanced electric field amplitude  $E_0$  shown by a substrate. Typically, this is evaluated at different molecular positions [6].

The underlying principle of Raman spectroscopy is associated with the detected inelastic scattering that occurs when incident electromagnetic field (or photon) interacts with the analyte molecule. This interaction generates a shift in the molecular polarizability that is directly proportional to the magnitude of the simultaneously induced dipole moment. Eq. 1-6 may be used to represent the Raman emission from a molecule that has been stimulated by a laser [35].

$$\mu(\nu_R) = \alpha_m(\nu_R, \nu_{inc})E_0(\nu_{inc}) \quad (1-6)$$

$\mu(\nu_R)$  is the induced dipole of the molecule, oscillating at the Raman frequency  $\nu_R$ , and  $E_0(\nu_{inc})$  is the incident field amplitude of the laser, oscillating at frequency  $\nu_{inc}$ ,  $\alpha_m$  is the molecular Raman polarizability.

According to classical theory of electromagnetic radiation, the power (P) radiated by a dipole in a vacuum is proportional to the square modulus of the dipole itself and to the 4<sup>th</sup> power of the Raman frequency [35]:

$$P = \frac{\nu_R^4}{12\pi\epsilon_0 c^3} |\alpha_m(\nu_R, \nu_{inc})E_0(\nu_{inc})|^2 \quad (1-7)$$

where  $c$  is the speed of light and  $\epsilon_0$  as the dielectric constant in a vacuum.

In SERS a localized electromagnetic field,  $E_{Loc}$ , is generated upon plasmon excitation within a SERS substrate at a specific frequency,  $\nu_{inc}$ . The presence of this localized field results in an enhancement of the radiated power,  $M_{Loc}^Z$ , as described by the following equation [36]:

$$M_{Loc}^Z = \frac{|E_{Loc}(\nu_{inc})|^2}{|E_0(\nu_{inc})|^2} \quad (1-8)$$

Therefore, as an approximation for the SERS enhancement of illuminated molecules the following equation is often used [35, 37]:

$$G_{SERS}^{EM} = [M_{Loc}^Z]^2 = \left[ \frac{|E_{Loc}(\nu_{inc})|}{|E_0(\nu_{inc})|} \right]^4 \quad (1-9)$$

Eq. 1-9 ignores the Stokes shift, which may be considered in a more complex expression [6].

$$G_{SERS}^{EM} = \frac{|E_{Loc}(\nu_{inc})|^2 |E_{Loc}(\nu_{vib})|^2}{|E_0(\nu_{inc})|^4} \quad (1-10)$$

### *Chemical enhancement mechanism (CM)*

The plasmon frequency in semiconductor materials lies in the infrared region due to the low density of electrons in the conduction band, and enhancement is mostly due to a CM. The CM enhancement is the result of several factors, including charge transfer between the analyte and the substrate, non-resonant charge in the molecular polarization, and molecular excitation resonances [8]. This mechanism results in mild Raman signal amplification between 10 and  $10^2$  [38]. The excitation laser wavelength can lead to signal amplification, when in resonance with the surface plasmon resonance (SPR) of the substrate takes place [32]. Molecular excitation resonances are generated when Raman scattering occurs by an electronic transition within analytes electronic states of the analyte as opposed to its virtual states [38]. Theoretical efforts have been put forward to identify the main effect that contributes to the CM. Nonetheless, for metal substrates, it is generally accepted that the CM is a result of an analyte-dependent charge-transfer (CT) excitation transition [39]. To expand, upon analyte adsorption, the analyte and the metallic surface may covalently bond (chemisorption), forming a surface complex; as a result, the polarizability of the molecule is affected. The process of the CT mechanism is displayed in Figure 1.7.

Excitation transitions from the Fermi level of the metal to the lowest unoccupied molecular orbital (LUMO) of the analyte and the electro-donation between the highest occupied molecular orbital (HOMO) of the analyte and the fermi level of the metal.

Under particular laser conditions, the electronic transition between the HOMO and LUMO can generate resonance processes that improve the Raman signal in a fashion called surface enhanced resonance Raman spectroscopy (SERRS) [40].

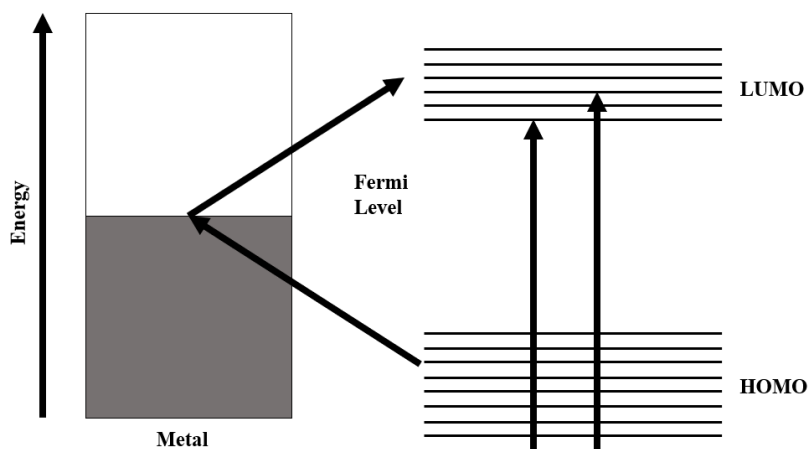


**Figure 1.7.** SERS charge-transfer mechanism for a plasmonic metal object forming a surface complex with a molecule (adsorbate).

### *SERS Selection Rules*

Selection rules have been applied to explain intensity strength of SERS peaks and reveal why SERS substrates may have a non-linear relationship with low analyte concentration; basically, the orientation of the molecule can change with concentration. According to the electromagnetic surface selection rules, a vibrational mode with its normal mode parallel to the metal surface, will experience less enhancement than a perpendicular arrangement, due to lack of scattering [15]. At increasing concentrations, the molecules are more likely to pack and force the plane of the molecule into a perpendicular orientation to the plane, increasing SERS intensity [41]. Perpendicular orientation is also heightened on a roughened surface [1, 7].

Simplified selection rules have been proposed by Creighton [42]. This involves considering the molecule as a distinct entity; although this is against principle as the



metal-analyte complex is expected to exist, this practice has shown to be valid in most cases. Assuming that this is the only effect of the metal atoms, the centre of symmetry is said to be disrupted as the molecule adsorbs to the surface, thus the IR-active bands can start to appear in the SERS spectrum.

#### **1.4. Progress of SERS-Active Materials**

Critical elements that contribute to the performance of a SERS substrate includes: the material's dimension size, shape, interparticle distance, dielectric properties, and surface roughness [31]. As shown in Figure 1.8, since the discovery of SERS, a broad variety of metallic and semiconducting substrates have been reviewed for SERS studies [31, 43]. SERS substrates can be categorized into one of three divisions based on the preparation methodology:

- 1) Synthesis of metal Nps in suspension (colloidal systems),
- 2) Assembly and immobilization of Nps on solid substrates (bottom-up approach), and
- 3) Direct fabrication of metallic nanostructures on a solid substrate using thin film deposition and lithography processes (top-down approach).

The convergence of SERS, analytical applications, photonic materials development, and nanotechnology has triggered tremendous growth in the development and exploration of innovative SERS-active substrate designs [13]. Figure 1.8 summarizes major contributions to substrate compositions that were discovered and applied from earliest 1970s to the present. For the sake of this work, a few relevant examples from Figure 1.8 will be discussed.

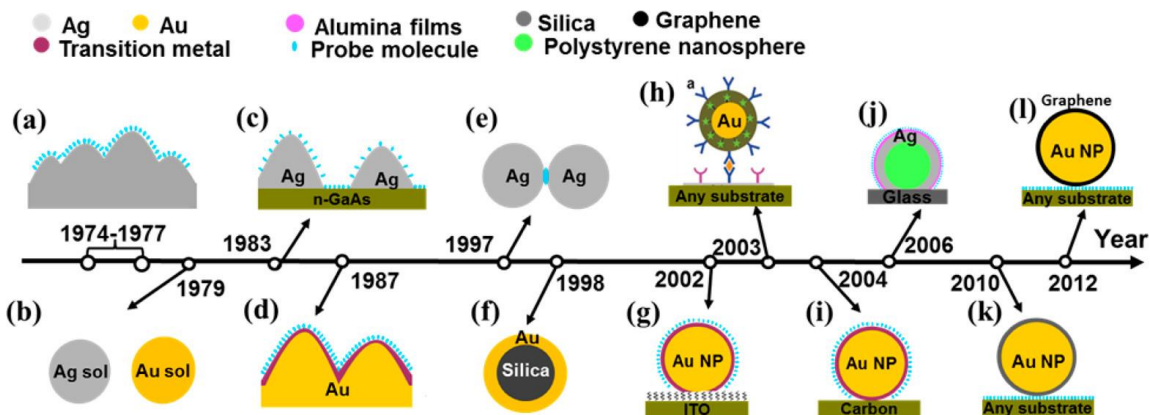


**Figure 1.8.** Timeline of SERS substrate development since discovery (a) The first SERS effect discovered on roughened Ag electrode, (b) SERS of Ag or Au colloids, of (c) silver nanoislands on n-GaAs electrode demonstrating “borrowing” strategy also highlighted by (d) deposited transition metal on roughened Au electrode, (e) single molecule SERS, (f) silica core-Au shell nanoparticle, (g) UPD and redox replacement transition metal on Au nanoparticles, (h) SERS tag, (i) Au core-transition metal shell nanoparticles, (j) Ag film on nanosphere (AgFON) substrates with an alumina layer, (k) silica shell isolated nanoparticles (SHINERS), and (l) graphene shell isolated nanoparticles. Reprinted (adapted) with permission from {Li, J.F., et al., *Core-Shell Nanoparticle-Enhanced Raman Spectroscopy*. Chem. Rev., 2017. **117**(7): p. 5002-5069}. Copyright {2017} American Chemical Society.

#### 1.4.1. Synthesis of Metal Nanoparticles in Suspension (Colloidal Systems),

Immediately after Van Duyne and Jeanmaire [29] discovered SERS, the origin of the SERS was linked to plasmon resonances on the roughened grooves of noble metals [44, 45]. Synthesized monodisperse Au, Ag and Cu colloidal nanoparticles (Figure 1.8b) were explored as SERS substrates. Colloidal Au, Ag, and Cu plasmonic Nps are of the first platforms investigated in pioneer studies, and are still relevant in current studies as the fabrication is relatively simple, and the systems offer excellent SERS efficiency with a high ratio of surface atoms [46, 47]. The earliest example of nanoparticle-based SERS substrates appears in 1979, where Ag and Au colloids were synthesized via sodium borohydride reduction to successfully detect pyridine molecules in solution [46]. The development of nanotechnology re-opened avid interest into SERS in the 1990s and since

then the morphological characteristics of the metal Nps and size of the colloidal particles and Nps aggregation have been a point of major interest and it is also the centre of modern developments as stated in SERS-focused reviews [43]. Au and Ag colloids can be prepared via wet-chemistry by a reduction ( $\text{NaBH}_4$ , or trisodium citrate etc.) method or the more chemically pure alternative, laser ablation. Shape/size control (5-100 nm) allows for governing the plasmonic resonance properties and ultimately, enhancing performance of the substrate. This type of substrate is advantageous in that the preparation is relatively simple, and inexpensive; although the experiments would fail at the hand of less than pure glass vessels, and poor time stability [24]. Controlled colloidal aggregation introduces Np-Np junctions and lower spatial and sample-sample variability, however this is difficult to achieve in suspension [48].

For the first time, in 1995, SERS activity was achieved using immobilized Au and Ag Nps on a solid supports functionalized with monolayers of molecules with thiol, amino, and cyanide groups [49]. This study demonstrated controlled colloidal self-assembly with good structural reproducibility by ways of functionalizing a solid support, however the sensitivity of the substrate was not assessed by the limit of detection as it was not reported. Subsequently, new methods for Np shape and surface modification have emerged for systems such as plasmonic 3D nanostars (Figure 1.9) and core-shell particles (Figure 1.8f). As shown in Figure 1.9, the shape of the metal Nps has a significant impact on the SERS-enhancement; being significantly higher at the single-particle level for complex gold nanostars (GNS) and gold nanorods (GNR) when compared with Au nanospheres; the effect of the excitation laser wavelength on the SERS enhancement is also demonstrated in this image [50].

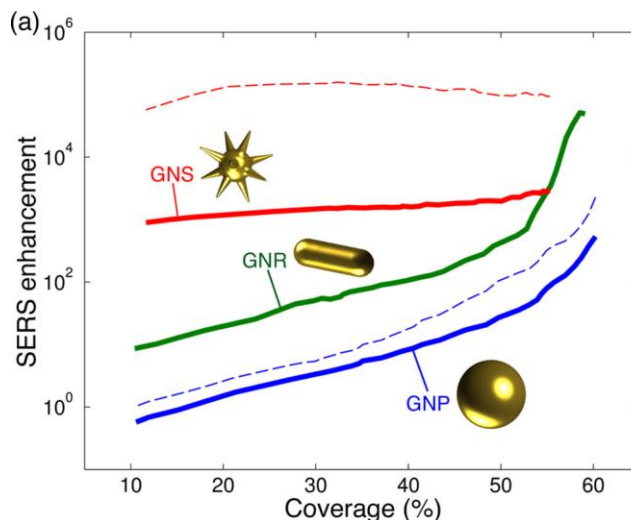


**Figure 1.9.** Simulation of maximum SERS enhancement for planar monolayers of particles with different morphology: Au Nanostars (GNS), Au Nanorods (GNR), Au Nanospheres (GNP). Dashed curves for GNPs and GNSs correspond to 633 nm and 900 nm, respectively, solid curves are derived at 785 nm laser wavelength. Reprinted (adapted) with permission from {Solís, D.M., et al., *Optimization of Nanoparticle-Based SERS Substrates through Large-Scale Realistic Simulations*. ACS Photonics, 2017. **4**(2): p. 329-337}. Copyright {2017} American Chemical Society. The image was obtained from <https://pubs.acs.org/doi/10.1021/acsp Photonics.6b00786>. Further permissions related to the material excerpted should be directed to the ACS.

Core-shell particles have also been investigated as SERS platforms. Results have shown that this type of structure can have some advantages over a single component-substrate. Wang et al. [51] investigated the formation of a Au shell deposited on SiO<sub>2</sub> microspheres via polyethyleneimine (PEI)-assisted seed-mediated growth method and controlled the thickness of the plasmonic shell by adjusting the Au<sup>3+</sup> concentration in solution. In a similar line, Jiang and co-workers [48] investigate the impact of the SiO<sub>2</sub> core surface properties on the SERS enhancement of a shell of Ag Nps. Specifically, mesoporous textured SiO<sub>2</sub> cores were synthesized using cetyltrimethylammonium bromide (CTAB) and compared to solid surface SiO<sub>2</sub> cores, where the mesoporous texture established a significantly higher SERS-EF ( $9.20 \times 10^6$ ) than the solid particle ( $4.39 \times 10^6$ ).

### **1.4.2. Assembly and Immobilization of Nanoparticles on Solid Substrates (Bottom-Up Approach)**

Colloidal systems very easily suffer aggregation in solution, however as shown in literature, this drawback can be overcome by immobilizing the Nps onto solid supports via bottom-up techniques. Bottom-Up methods are designed to overcome aggregation problems, by combining smaller units (smaller particles, atoms, molecules) on solid supports [24]. Colloidal metallic Nps deposited on a solid support is known to provide an element of rigidity that aids in producing superior SERS activity, intensity reproducibility, and Np stability, while maintaining simple tactics [6].

Recent advances in SERS include developing new methods for depositing plasmonic material over large areas ( $> 1\text{cm}^2$ ) for potential SERS applications. A larger substrate area also has a better probability of capturing species of dilute solutions and increases sample size for quantification statistics by providing more sites for analysis [22]. Bottom-up preparation procedures that have been demonstrated to result on active thin film SERS substrates include: colloidal self-assembly by chemical attachment of NPs via small molecules or bifunctional polymers [49], inverse micelle polymer film [52], layer-by-layer assembly [12, 53], colloidal self-assembly by electrostatic interaction between NPs and surface [54], and liquid-liquid interface Langmuir-Blodgett (LB) assembly [55]. These solution-phase methods require liquid media element at some part of the procedure and are easily scalable.

Solid state bottom up methods also exist for the production of thin films. Chemical vapour deposition (CVD) achieves deposition of a thin film on a planar surface by ways of a chemical reaction between gaseous molecules that inhabit suitable atoms to form

Nps. Three techniques—photoinitiated, plasma-enhanced, and thermally active chemical vapour deposition—can be used for sample deposition [24]. Physical vapour deposition (PVD) for thin film fabrication is practiced with highly controlled vacuum techniques such as sputtered deposition and thermal evaporation to vaporize a material that will then be condensed onto the planar surface as a thin film. Farling et al. [56] effectively prepared Ag SERS substrates by depositing thin Ag films using PVD on commercial screen-printed carbon electrode (SPE) for electrochemical-SERS (EC-SERS). SEM magnification of the SPE revealed a rough carbon surface that served as an excellent template during Ag deposition and promoted the formation of hot spots. This work further highlights that SERS enhancement is achievable with substrates inhabiting a high density of small nanogaps [57, 58].

#### **1.4.3. Direct Fabrication of Metallic Nanostructures on a Solid Substrate using Thin Film Deposition and Lithography Processes (Top-Down Approach).**

The top-down approach reduces bulk starting material into nanosized particles by ways of a chosen physical or chemical treatment. The associated methods produce highly ordered metallic structures on planar solid supports.

Such substrates avoid the challenge of irreproducible structure leading to the substrate generating similar SERS-EF values [8, 23]. The methods under this umbrella include popular nanolithographic methods, including ion-beam milling, electron-beam lithography, interference lithography, photolithography, nanoimprint lithography, nanostencil lithography and nanosphere lithography [24]. Advanced methods such as these, manufacture substrates that exhibit precisely controlled shape, size, and relative

orientation of Nps. Despite being extremely reproducible, these methods tend to be expensive and tedious to operate. It is often a challenge to fabricate Nps of a desired shape and below a specific size. It is also a difficult to alter the physicochemical properties and surface chemistry of the resulting Np [24].

Some reports have claimed that nanolithography-based fabrication methods can be complex, while multiple solution-based deposition methods such as, colloidal self-assembly tend to contain many steps and can be time-consuming [59].

### **1.5. Screen-Printing**

Printing technology is a common technique that is relatively cheaper than high-vacuum methods, and it can be also used to form patterned arrays on a variety of solid supports in a few steps [60]. The screen-printing process involves using a porous mesh screen with a uniform pattern to create a film using a thixotropic paste or ink that is forced through the fine screen fabric with the help of a squeegee movement.

Printing methods also improved quality control, enabling controlled deposition of ink with reproducible thickness. The process does not require extensive preparation, utilizes affordable instrumentation, and applies to scalable printing for many substrates. Screen printing is a method under printing technology frequently used to produce conductive lines and electrodes on a large scale. Currently, only a few published works describe the use of screen-printing in creating reproducible SERS substrates such as Ag dot arrays or potentiometric cells [59-61].

## 1.6. SERS Characterization

The results for the theoretical SERS-EF are described in section 1.3.1. Due to the complexity of experimental conditions and SERS nanostructured systems, the theoretical results rarely agree with the actual SERS-EF, and a clear definition for SERS-EF must be defined [37].

There are several procedures for calculating the enhancement factor of a SERS substrate [62]. The analytical enhancement factor (AEF) is a simple way for researchers to define the enhancing performance of a substrate. Assuming that signal intensity exhibits linear behavior with respect to power density and analyte concentration, AEF can be given by:

$$AEF = \frac{I_{SERS}}{I_{RS}} \frac{C_{RS}}{C_{SERS}} \quad (1-11)$$

where  $I_{SERS}$  is the SERS signal intensity of a specific band at a concentration of  $C_{SERS}$  and  $I_{RS}$  is the intensity of the normal Raman signal of the same analyte at the same concentration,  $C_{RS}$ . If the same solution is used, the AEF is just the ratio of the intensities.

The average SERS-EF acknowledges that the SERS signal is a response to only adsorbed molecules and is considered a better estimate than AEF. The most common way to describe the average value of the SERS-EF is as follows: [62]:

$$SERS - EF = \frac{I_{SERS}}{I_{RS}} \frac{N_{Raman}}{N_{SERS}} \quad (1-12)$$



where  $N_{Raman}$  denotes the number of probed molecules contributing to the normal Raman signal in the scattering volume.  $N_{SERS}$  relates to the number of adsorbed molecules on the substrate.

Gupta and Weiner reported another adoptive estimation of the SERS-EF [63].

Assuming the analyte is adsorbed on the SERS substrate as a monolayer, the average number of probed molecules is related to the laser spot area,  $A$ , the geometrical area of the analyte layer,  $S$ , and the number of molecules initially casted on the substrate,  $N_{cast}$ , as follows:

$$N_{E,i} = A * N_{cast,i} / S \quad (1-13)$$

$i = Raman \text{ or } SERS$

To specify the effective number of probed molecules,  $N_E$  for a SERS experiment,

Eq. 1-13 can be re-written as:

$$N_E = A * N_{cast} / S \quad (1-14)$$

The  $N_{cast}/S$  ratio has the units of *molecules/cm<sup>2</sup>*. The final SERS-EF formula is

defined as follows:

$$SERS - EF = \frac{I_{SERS} * S_{SERS} * N_{cast,Raman}}{I_{Raman} * S_{RAMAN} * N_{cast,SERS}} \quad (1-15)$$

where  $N_{cast,Raman}$ , refers to molecules initially casted during Raman analysis, and  $N_{cast,SERS}$  is that during SERS analysis. In this equation,  $A$ , is cancelled out in the ratio of SERS intensity to Raman intensity [64].

Variations of the SERS-EF (including the modified expressions previously mentioned) are used extensively to report the performance of new substrates; however, it is not the ideal metric for comparison of analytical significance between substrates and even very difficult to implement in the case of the Au@SiO<sub>2</sub> substrate in this work. Direct comparison of the EF between substrates overlooks the varying characteristics each might possess that will give different EF values, not only based on the amplifying ability of the substrate but based on other factors, such as morphology or phase that are not accounted for in the calculation. Also, the number of surface adsorbed molecules is calculated based on an assumption, which may lead to final values that are misleading and cannot be compared to others with accuracy.

Additionally, as researchers in SERS continue to innovate novel systems for sensitive SERS detection, comparing studies becomes more complicated. To elaborate, there are many established variables that affect the SERS enhancement factor (SERS-EF) of a typical SERS measurement: 1) the analyte species under study, 2) the number of analyte molecules present in the enhanced probing region of the substrate, 3) the extent of enhancement achievable by the substrate, and 4) the parameters and performance of the Raman instrument [20, 65]. Moreover, a few literature reviews have moved against using the substrate SERS-EF as a means to study analytical significance. Although there are classic papers that report multiple procedures for calculating SERS-EF for a general substrate, the proposed calculations include assumptions that invite potential for error,

and cannot be applied to substrates that exhibit different characteristics to compare them directly [22]. With SERS-specific standardized analytical protocols, the extent of these issues can be limited [20]. For instance, substrates' performance can be evaluated by comparing their sensitivity, limit of quantification (LoQ), and limit of detection (LoD) using specific analytes. In this case, the studies were carried out with Rhodamine 6G (R6G) a common analyte used for evaluation of new SERS substrates.

### **1.7. Rhodamine 6G as Target Analyte for SERS Characterization**

Several molecules have been used for SERS substrate evaluation studies; some were considered in this study, including R6G, Nile blue A, methylene blue, 5,5-dithio-bis-(2-nitro-benzoic acid), and 4-mercaptobenzoic acid [51, 53, 66, 67].

R6G is an inexpensive fluorescent dye that exhibits maximum sensitivity at 532 nm attributed to its molecular absorption band at 525 nm [68]. It is commonly used to test the SERS enhancement efficiency of various nanostructured substrates. As an example, SERS spectra reported for aqueous R6G solutions from  $1 \times 10^{-4}$  to  $1 \times 10^{-10}$  M on Au thin films deposited via pulsed laser ablation are shown in Figure 1.10 [69]. When excited by a 532 nm visible laser, R6G becomes a strong fluorophore that fluoresces and absorbs in the visible region. R6G can strongly adsorb to a roughened Au surface (ultimately quenching the fluorescence emission), and can participate in SERRS, enhancing the SERS signal intensity. As seen in Figure 1.11, R6G is an unsaturated aromatic molecule with planar rings of atoms. By comparison with molecules with a similar structure [15], it is proposed that chemisorption interaction of R6G with the gold surface can be

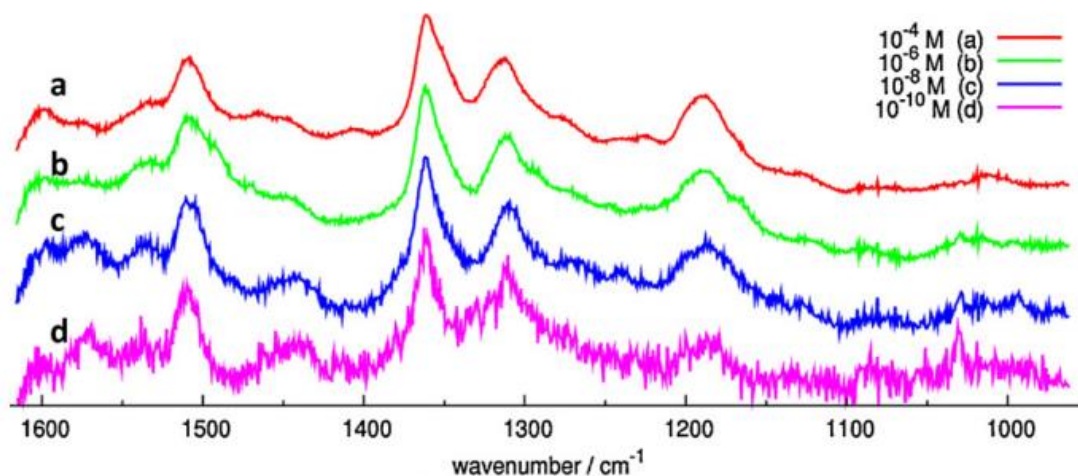


**Figure 1.10.** SERS spectra collected on Au thin films soaked in aqueous R6G solutions from  $1 \times 10^{-4}$  to  $1 \times 10^{-10}$  M. Au film were prepared via pulsed laser ablation using a KrF excimer laser ( $\lambda = 248$  nm, pulse width 25 ns, repetition rate 10 Hz) in the presence of controlled argon at 100 Pa. Reprinted from Appl. Surf. Sci., **258**, N. R. Agarwal, F. Neri, S. Trussoc, A. Lucotti and P. M. Ossi, Au nanoparticle arrays produced by Pulsed Laser Deposition for Surface Enhanced Raman Spectroscopy, p. 9148-9152, Copyright (2012), with permission from Elsevier

established through the lone pair electrons of the oxygen and nitrogen atom(s) from the pyran ring, ester, and secondary amino groups; or through the  $\pi$  electrons of the rings. In the case of SERS, the enhancement factors are highly dependent on the substrate. Figure 1.12, where the SERS spectra for R6G on Au on two different substrates, horizontally-aligned carbon nanotubes (HA-CNT) and  $\text{SiO}_2$  on silicon substrates are shown. Table 1.1 summarizes the main vibrational bands for R6G observed on Figure 1.12.

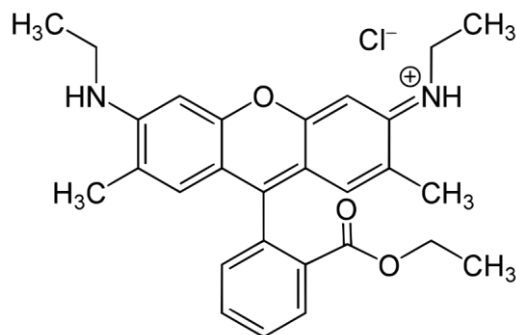


**Figure 1.11.** Chemical Structure of R6G

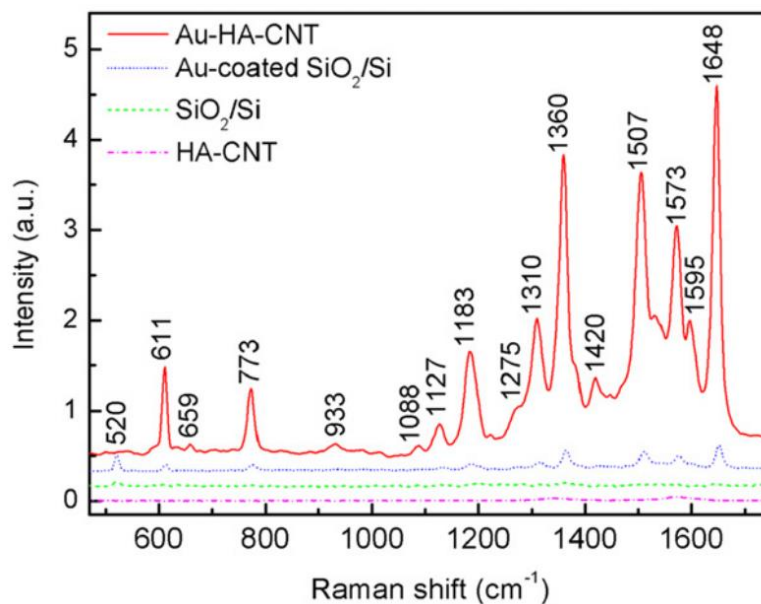


**Figure 1.12.** SERS Spectra of R6G ( $10^{-6}$  M) on different substrates with and without Au. Red: Granular Au-sputtered horizontally aligned multiwalled carbon nanotube (Au-HA-CNT). Reprinted from Nanotechnology, X. N. He, Y. Gao, M. Mahjouri-Samani, P. N. Black, J. Allen, M. Mitchell, et al., *Surface-enhanced Raman spectroscopy using gold-coated horizontally aligned carbon nanotubes*, **23**, p. 205702, 30 April 2012; <http://dx.doi.org/10.1088/0957-4484/23/20/205702> © IOP Publishing. Reproduced with permission. All rights reserved

**Table 1.1.** Assignment of R6G vibrational modes [70-72]

<b>R6G Raman Shift (cm<sup>-1</sup>)</b>	<b>Assignment</b>
612	C–C ring in-plane bending in xanthene/phenyl rings
659	C-C-C ring in-plane bending
772	C–H out-of-plane bending
1088	C–H out-of-plane bending
797	Hybrid mode (xanthene/phenyl rings and NHC <sub>2</sub> H <sub>5</sub> group)
1127	C–H in-plane bending in xanthene/phenyl rings
1187	C–H in-plane bending in xanthene ring
1204	Hybrid mode (xanthene/phenyl rings)
1275	C–O–C stretching in COOC <sub>2</sub> H <sub>5</sub> group on phenyl ring
1312	Hybrid mode (xanthene/phenyl rings and NHC <sub>2</sub> H <sub>5</sub> group)
1363	C–C stretching in xanthene ring
1420	C-C stretching
1449	C–N stretching in NHC <sub>2</sub> H <sub>5</sub>
1509	C–C stretching in xanthene ring
1575	C–C stretching in phenyl ring
1595	Hybrid mode (phenyl ring with COOC <sub>2</sub> H <sub>5</sub> )
1651	C–C stretching in xanthene ring

Some vibrational modes are very weak and therefore are not observed at low concentration. The bands observed at 611-613 and 1648-1649 cm<sup>-1</sup> are strong, and therefore many studies involving R6G have used these bands for performance assessment of new substrates. These two bands will be also used for statistical analysis in this thesis.

### 1.8. Motivation and Thesis Objectives

High fabrication cost and the lack of signal reproducibility amongst solution-based substrates are hindering factors to the integration of SERS into analytical applications. Although nanolithographic methods are highly reproducible and convenient for this application, they are expensive and may not be readily accessible. Assessing and optimizing low-cost fabrication methods can aid to overcome these obstacles as long as the method is scalable and reproducible. Screen-printing technology has gained interest in

the SERS field for preparing low-cost and uniform SERS-active films and following that up with spatial, and sample-sample signal variability assessment [59].

The aim of this thesis was to extend the scope of current cost-effective screen-printing methods for the preparation of highly sensitive and reproducible SERS substrates by using pastes formulated with uniform-sized SiO<sub>2</sub> particles to create a controlled distribution of nano-gaps on silica slides, and then using this as a template for the adsorption of Au plasmonic nanoparticles. The method is easily scalable for large-scale production.

Extensive work has been dedicated to the synthesis and characterization of materials, formulation of paste for screen printing, film deposition, SiO<sub>2</sub> particle functionalization, and SERS characterization studies. Some specific objectives include:

- Synthesis of citrate-capped Au Nps (3-5 nm) via borohydride reduction reaction, and synthesis of smooth surface (s-SiO<sub>2</sub>) and textured surface SiO<sub>2</sub> (t-SiO<sub>2</sub>) particles (300-400 nm)
- Characterization studies of SiO<sub>2</sub> particles with different surface texture and pore properties.
- Application of SiO<sub>2</sub> thin films on silica glass slides under controlled screen-printing conditions (film thickness and noble metal interparticle distance) with as-prepared SiO<sub>2</sub>-based paste.
- Probe the impact of film surface properties on SERS performance of the Au@SiO<sub>2</sub> substrates with Rhodamine 6G
- Evaluation of the analytical performance of Au@s-SiO<sub>2</sub>, and Au@t-SiO<sub>2</sub>, SERS enhancement, sample-sample reproducibility, and spatial reproducibility

## Chapter 2: Experimental Section

### 2.1. Materials

The following chemicals were purchased and used as received for preparing Au@SiO<sub>2</sub> film SERS substrates. Tetrachloroauric(III) acid trihydrate (HAuCl<sub>4</sub>·3H<sub>2</sub>O; ≥49.0 %, Sigma-Aldrich), trisodium citrate dihydrate (≥99.0 %, Sigma-Aldrich), sodium borohydride (NaBH<sub>4</sub>; 99%, ReagentPlus), isopropyl alcohol (99.9%, Fisher Scientific), ammonium hydroxide solution (28.0-30%, Sigma-Aldrich), tetraethyl orthosilicate (TEOS; 98%, Sigma-Aldrich), ethyl alcohol anhydrous (Greenfield), polyethyleneimine (branched, Mw 25 kDa, Sigma-Aldrich),  $\alpha$ -terpineol (96%, Sigma-Aldrich), ethyl cellulose (Viscosity 10 cP, Sigma-Aldrich), acetone (99.5%, ReagentPlus), 3-aminopropyltrimethoxysilane (APTMS; 97%, Sigma-Aldrich), rhodamine 6G (95%, Sigma-Aldrich), silica (200 nm nanoparticles, mesoporous, pore size 4 nm), polyvinylpyrrolidone, (PVP; Mw 360 kDa, Sigma-Aldrich), white spirit (~17% aromatics basis, Sigma-Aldrich), 2-(2-butoxyethoxy)ethyl acetate (BCA; ≥99.2%, Sigma-Aldrich). Water used throughout these experiments was deionized using a Milli-Q deionization system (Millipore Q-Gard T2, Millipore Quantum TEX); and it met the requirements for ASTM Type 1 water, with a resistivity of 18 M $\Omega$ .cm. Gases used throughout were purchased from Praxair: extra dry air (AI0.0XD-T), and nitrogen (99.995%, Ni5.0UH-T).

### 2.2. Characterization Techniques

UV-Vis spectroscopy (liquid and solid samples) was used for the characterization of Au in aqueous media and thin films containing Au nanoparticles since the absorption spectra of nanoparticles strongly depend on the size of the particles. UV-visible



absorption studies were carried out in an Agilent Technologies Cary 60 UV-visible spectrometer, and studies on film performed with a Perkin Elmer Lambda 750 S 60 mm sphere UV/Vis/NIR Spectrometer (250-800 nm).

Surface area of synthesized SiO<sub>2</sub> nanoparticles (diameters ~ 200-400 nm) were obtained from N<sub>2</sub> adsorption/desorption isotherms. These studies were carried out with the Quantachrome Nova 1200e Surface Area and Pore Size Analyzer. SiO<sub>2</sub> samples (~ 0.8 g) were degassed at 200 °C for 6 hours.

Synthesized SiO<sub>2</sub> nanoparticles and the sequentially produced SiO<sub>2</sub> pastes contain organic material from their respective synthetic procedures. To determine the sample SiO<sub>2</sub> content, thermogravimetric analysis (TGA) was used to observe the weight change of the material as the temperature is increased under well-defined conditions. This technique also provides information on the decomposition temperatures of the different components in the sample. TGA was performed with a TA instruments SDT Q600 under a flow of dry air at 10 mL/min and a temperature scan rate of 20 °C/min from 25 °C to 1000 °C.

The particle size distribution of Au@SiO<sub>2</sub>, SiO<sub>2</sub> films and SiO<sub>2</sub> powder were analyzed using nanoparticle imaging with a scanning electron microscopy (SEM). In SE (secondary electron) mode, the SEM microscope can reach a resolution of 4 nm if coupled with a high accelerating voltage; thus, it is capable of detecting SiO<sub>2</sub> particles estimated to be around 200-400 nm in diameter. SEM studies were completed with a Hitachi FlexSEM 1000 scanning electron microscope. Semi-quantitative elemental analysis was also done with this instrument using a Peltier-cooled energy dispersive X-ray detector for energy dispersive x-ray analysis (EDX). The details on the SEM

conditions used for each image may change from sample to sample and are provided in other sections.

Transmission electron microscopy (TEM) is a different imaging technique that has a better resolution than SEM ( $<0.37$  nm), providing a particle size distribution (PSD) and particle size details for nanoparticles less than 10 nm in size. TEM was used to obtain microscopic images of the SiO<sub>2</sub> particles, and the Au Nps (~3-5 nm). TEM images were collected by Dr. Carmen Andrei from the Canadian Centre for Electron Microscopy at McMaster University on a Talos L120C Transmission electron microscope.

Surface roughness and thickness of SiO<sub>2</sub> films with and without the deposited Au Np layer were acquired using a Profilm3D profilometer at the micrometer level. The instrument uses non-contact white light interferometry (WLI) to distinguish surface depth changes and generate a measured surface profile.

For the preparation of thin films using the screen-printing approach, the rheological properties of the pastes were studied using an HR20 rheometer with a 40 mm parallel plate. Viscosity measurements were performed at increasing shear rates, 0 s<sup>-1</sup> to 500 s<sup>-1</sup>, and the shear-thinning ability was analyzed where the paste decreases in viscosity at higher shear rates.

### **2.3. Material Synthesis**

#### ***SiO<sub>2</sub> particles (200-400 nm)***

To synthesize the SiO<sub>2</sub> microspheres, the Stöber method was followed as reported by Greasley et.al [73]. With this method, the size of the final spherical particles can be controlled by simply adjusting reaction parameters such as the reactant concentrations

and pH. The procedure begins with the addition of deionized water (6 M) and ammonium hydroxide (0.57 M) to absolute ethanol. The mixture was sonicated at room temperature for 10 minutes, and TEOS (0.28 M) ( $\text{SiO}_2$  precursor) was added to the solution and stirred overnight. Finally, the solution was centrifuged to recover the solid  $\text{SiO}_2$  particles. The solid product was dried at 80 °C in a conventional oven. To obtain a textured surface particle, CTAB (4.12 mM) was added to the precursor solution as a cationic surfactant [48]. The recovered  $\text{SiO}_2$  particles synthesized with CTAB were subjected to three washes in acetone with a centrifugation step between washes to remove residual CTAB from the particle surface. Figure 2.1 shows the thermograms for the t- $\text{SiO}_2$  and s- $\text{SiO}_2$  samples. The mass loss observed in the case of t- $\text{SiO}_2$  clearly indicates that even after several acetone washes (3) and centrifugation steps, there is still ~ 10 wt% of CTAB adsorbed on the surface of the particles. A further analysis of the thermograms in Figure 2.1, indicates that the overall combustion process involves several steps. Literature shows that, the reduction of the silanol tends to occur over a wide temperature range (200 °C - 1000 °C) [74]. In the study completed by Mueller et al. [75], it was found that dehydroxylation on pure synthesized silica occurs at a rate of 0.4-1 OH surface group for each  $\text{nm}^2$  of  $\text{SiO}_2$ . Considering this, dehydroxylation is miniscule, the combustion of CTAB to  $\text{CO}_2$  and  $\text{H}_2\text{O}$  is the main process responsible for the observed mass loss.

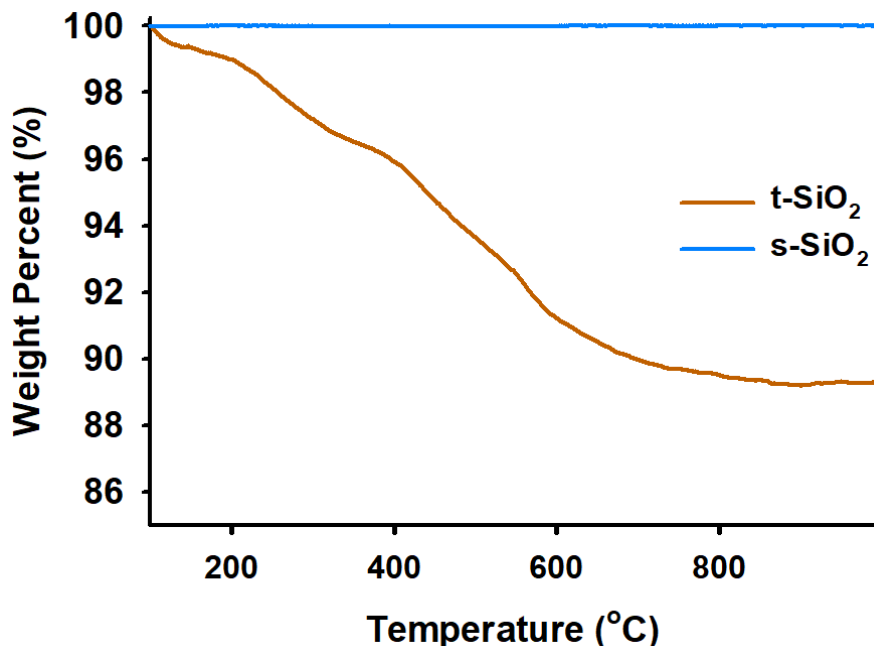


**Figure 2.1.** TGA curves for t-SiO<sub>2</sub> (orange) and s-SiO<sub>2</sub> (blue) powders retrieved under air in this thesis. Gas flow rate: 10 mL/min and heating rate: 20 °C/min.

### *Au Nps (3-6 nm)*

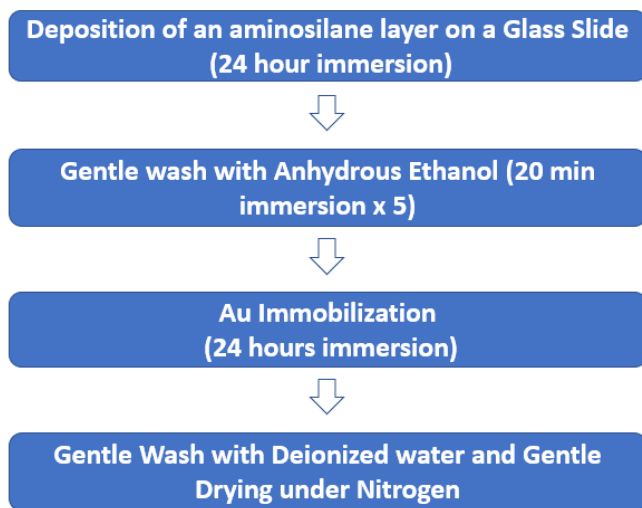
For the preparation of the Au Nps, 500 mL of an aqueous solution containing HAuCl<sub>4</sub> (0.33 mM) and trisodium citrate (0.33 mM) as capping ligand was placed under vigorous stirring for 5 minutes, after that 20 mL of freshly prepared 1 mM NaBH<sub>4</sub> solution was added to the initial solution. As the HAuCl<sub>4</sub> is reduced, the Au Nps began to form, and the solution turn dark pink. The solution was allowed to stir while protected from light for approximately 24 hours and then stored at room temperature while protected from external light.

## 2.4. Preparation of SERS Substrates

Two approaches were studied for the fabrication of three-dimensional (3D) Au SERS-active thin films (Scheme 2-1 and 2-2). In this section, the steps involved in both approaches are summarized and described in detail.

### 2.4.1. Au Nps on Amino-functionalized Glass Flat Substrates

More than one experimental preparation method was attempted in this work. The following method involved the self-assembly of an aminosilane (APTMS) layer prior to the deposition of the Au Nps according to a method previously reported by Brito-silva et al [76]. The main steps for this method are outlined in Scheme 2-1.



**Scheme 2-1.** Steps for the development of a Au Nps films on glass slides

The glass slides were cleaned with aqua regia to remove any organic residue from the glass slide surface preceding functionalization. The APTMS layer is covalently bonded to the SiO<sub>2</sub> glass slide and yields free amino groups which improve the surface affinity of

Au Nps during immobilization as well as Au Np adherence to the glass. By altering the surface charge of the substrate, the APTMS compensates for the negative charge provided by the silanol groups on the glass. It has been reported that the protonation of the APTMS amino groups drastically alters the charge distribution on the functionalized surface [76]. The positive charge distribution enhances the interaction of the citrate capped Au Nps to the glass surface. APTMS is a moisture and air-sensitive chemical that is highly reactive with water, making the procedure slightly tedious as each APTMS assembly was done under nitrogen gas. Anhydrous ethanol was used as the solvent in the subsequent slide washing steps to avoid uncontrolled SiO<sub>2</sub> formation on the slide and reaction with the Au Nps during immobilization; multiple washes were required to ensure excess silane was removed.

### ***Aminosilane functionalization***

Aminosilane functionalization was performed with a solution of (APTMS) in toluene (19% v/v) prepared using dry glassware, dry toluene, and minimizing the contact with air. Slides (25 x 13 x 1.0 mm) were immersed in 7 mL aliquots of APTMS solution for 24 hours in closed vials; this amount of solution was enough to cover the entire slide. After functionalization, the slides were washed by immersion in ~7 mL of anhydrous ethanol to remove the excess of APTMS. The washing was assisted with 15 minutes of orbital stirring at a gentle rotation speed and repeated five times with fresh anhydrous ethanol. For a schematic of this procedure please refer to Appendix A1.

### ***Au Np layer***

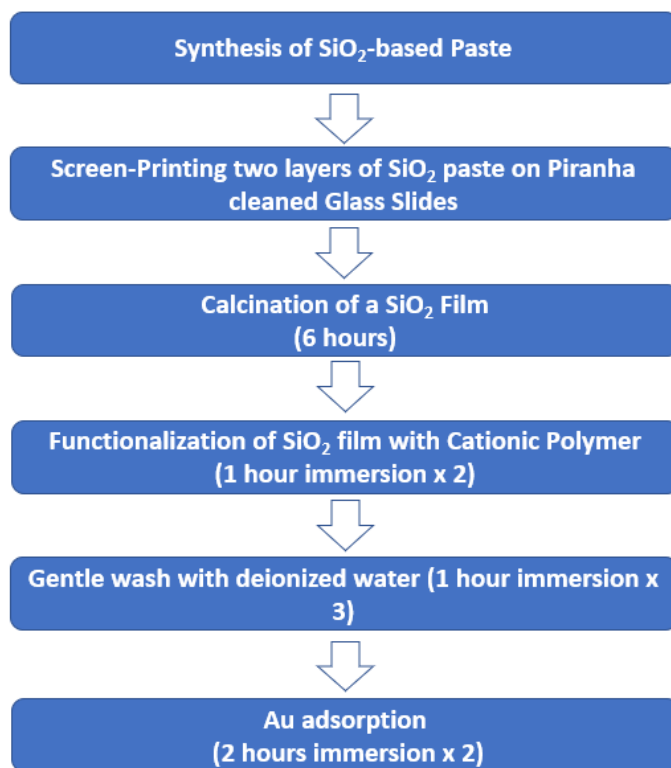
A sonicated solution of previously prepared Au Nps was used for the deposition of a self-immobilized Au layer on the functionalized glass slides. Prior sonication was required to ensure a uniform colloidal solution of Au Nps. The functionalized glass slides were immersed in 7 mL of Au Nps solution and after 24 hours, the glass slides were gently washed with deionized water and dried under nitrogen to reveal a dry, thin film of Au Nps characterized by a faint purple colour.

### **2.4.2. Au@SiO<sub>2</sub>/SiO<sub>2</sub> Substrates**

It was found that the previous approach was simple, however it was highly time-consuming with steps that required 24 hours to complete. The resulting Au layer showed signs of uneven Np distribution with dark and light areas along the glass surface thus, it was challenging to obtain reproducible substrates using the previous method. In addition, the SERS enhancement factor was low for single layer films, and the preparation of multilayer substrates with increased plasmonic material was extremely time consuming as multiple layer-by-layer depositions are required to observe a high SERS enhancement. In an attempt to control the deposition of material onto the film, screen-printing was pursued as a way to create a reproducible and uniform template for functionalization and Au layer deposition while maintaining simplicity and cost-effectiveness.

Scheme 2-2 illustrates the main steps required for the fabrication of Au@SiO<sub>2</sub> films involving: (1) Slides and paste preparation, (2) Screen printing of 2 layers of silica paste onto piranha cleaned glass slides with a drying step on a hot plate between layers, (3) Calcination of the silica film to remove volatile components from the paste and improve

the adherence to the silica slide, (4) Functionalization with a stable cationic polymer (PEI) that electrostatically interacted with the silica film/slide, (5) Removal of excess PEI molecules via washing in Milli-Q water, and (6) Au Nps adsorption



**Scheme 2-2** Sequential steps involved in the procedure used for Au@SiO<sub>2</sub> nanoparticles using s-SiO<sub>2</sub> and t-SiO<sub>2</sub>

### *Paste preparation*

The screen-printing approach requires the preparation of a paste/ink that will be applied over a woven mesh with pre-determined pattern, a 1 cm x 1 cm square area in the case of this thesis, to produce a uniform thin film on a clean glass slide. The paste composition will dictate the properties of the film, such as the thickness, the silica content, and the porosity of the material after annealing at high temperatures. The



rheological properties of the pastes can be adjusted to produce reproducible and uniform films. As a result of several trials with different paste composition, it has been found that the ideal composition for these experiments is as follows: 18 wt% SiO<sub>2</sub> Nps, 64 wt%  $\alpha$ -terpineol, 9 wt% ethyl cellulose, and 9 wt% ethanol [77]. Ethyl cellulose was used as an organic binding agent to aid in the stability of the paste by keeping the SiO<sub>2</sub> filler and the solvent ( $\alpha$ -terpineol) held together as well as providing an adequate viscosity.

To generate the paste, the SiO<sub>2</sub> filler is added to the  $\alpha$ -terpineol and ethyl cellulose according to the assigned weight percentages and magnetically stirred for 2 hours. Approximately 50 mL of ethanol is added to the mixture to facilitate favourable interaction amongst the paste components in the solution while stirring. After 2 hours, the solution is sonicated for 1 hour, and then stirred again for 2 more hours. The mixture is transferred to two 100 mL yttrium stabilized zirconium oxide grinding jars containing 100 (5 mm) and 16 (10 mm), grinding balls of the same material. Then the paste solution was further dispersed with an Across International PQ-N04 Planetary Ball Mill rotating at 25 Hz for 20 hours.

Ethanol must be removed to obtain a mixture with appropriate viscosity. It has been found experimentally that ~ 9 to 10 % ethanol is required for obtaining smooth and uniform silica thin films. For this reason, after recovering the paste solution from the ball mill, the excess of ethanol is removed by rotary evaporation under vacuum at 70 °C. By tracking the weight of the paste product and the contents of the initial mixture, the ethanol content was monitored. The main solvent,  $\alpha$ -terpineol, is less volatile than ethanol therefore during evaporation,  $\alpha$ -terpineol remains in the paste material. The produced SiO<sub>2</sub> paste is used the same day.

### ***Preparation of films***

Microscopic glass slides from FisherBrand™ (25 mm x 75 mm x 1.0 mm) were cut to ~ 25 mm x 13 mm x 1.0 mm. The slides as well as the vials that inhabit the slides, were cleaned with a basic piranha solution, and then washed with Milli Q water and isopropanol. Drying was done at 100 °C in a conventional oven. In basic piranha solution, silanol groups are also introduced on the surface of the glass slides. Ultimately the adhesion of the SiO<sub>2</sub> paste is improved after annealing by forming Si-O-Si bonds. Screen-printing of the silica paste described in the previous section on these substrates, after two applications and with a drying step on a hot plate (~ 100 °C) for 10 seconds between layers, the method resulted in films (1.0 cm<sup>2</sup>) with a thickness of ~ 4 to 6 μm after annealing at 600 °C. It is worth noting that the mesh needs to be properly cleaned before and after completing the deposition of the silica pastes with a white spirit solvent; and it should be fully dry before starting screen-printing the pastes. The process is repeated again to create a 2-layers film.

### ***Calcination and annealing***

Figure 2.2 shows the heat treatment adopted for annealing the SiO<sub>2</sub> films and it is based on previous thermogravimetric data obtained for the combustion of α-terpineol and ethyl cellulose mixtures by a former student, Donald McGillivray, in our group (Figure 2.3) [78].



Despite the different mass content because the paste formulation is different, the thermogram in Figure 2.3 obtained under air (20 mL/min) at a heating rate of 20 °C/min can be used to identify the main mass loss steps in the ethyl cellulose, terpineol, and metal oxide system. As shown, the mass loss vs. temperature plot shows a slight mass loss before 140 °C assigned to ethanol evaporation (boiling point 78 °C) and a nearly 50% decrease in mass at ~200 °C attributed to the vaporization of  $\alpha$ -terpineol (boiling point 217 °C). As shown, the combustion of ethyl cellulose with formation of CO<sub>2</sub> and H<sub>2</sub>O takes place between ~360 °C and 400 °C. The remaining 20% of mass is the filler that in the case of McGillivray thesis was TiO<sub>2</sub> [78]. This analysis demonstrates that the slides prepared in this study must be exposed to temperatures above 400 °C for sufficient combustion of the undesired paste components.

The mass loss for the t-SiO<sub>2</sub> sample occurs around 200-600 °C further demonstrating the need to calcine the sample films around 600 °C. Exposing the film to such high temperatures also improves the film's adherence to the glass. This was confirmed by a tape test: the annealed film was immersed in water for a short period of time and failure to remove a significant amount of the film with tape adhesion was the result. Alternative flat support substrates to silica, such as quartz, could be used to increase the annealing temperature if desired.

### ***SiO<sub>2</sub> surface functionalization (PEI@SiO<sub>2</sub>)***

Previous experiments showed that the adherence of the negatively-charged citrate-capped Au Nps to the SiO<sub>2</sub> particle films was low due to the alike surface charge of SiO<sub>2</sub>. In previous studies, this problem has been solved by adsorbing a cationic surfactant (PEI)



film adherence to the glass slide. Each immersion contained an excess amount of PEI and was done twice to ensure surface saturation. After two immersions in fresh PEI solution, the slides were gently washed with deionized water. Further washing was done via immersion in deionized water three times with fresh deionized water each time and 1 hour for each step. Washing is necessary to remove non-adsorbed PEI from the porous films and avoid Au Np aggregation during the Au Np deposition step. UV-vis spectroscopy was used to monitor the presence of PEI after multiple washes of the functionalized SiO<sub>2</sub> film (PEI@SiO<sub>2</sub>).

In solution, Au Nps and PEI molecules interact with each other to form a PEI-Au aggregate that absorbs radiation in the UV-visible region and it can be used as an indication of PEI. As shown in Figure 2.5, after adding Au Np solution to the first wash generates a solution that exhibits a clear shift in the peak for Au to longer wavelengths, consistent with the presence of PEI in the washing solution, after three washing steps, the peak absorbance wavelength of Au in the water washing solution resembled that of the original Au NPs.

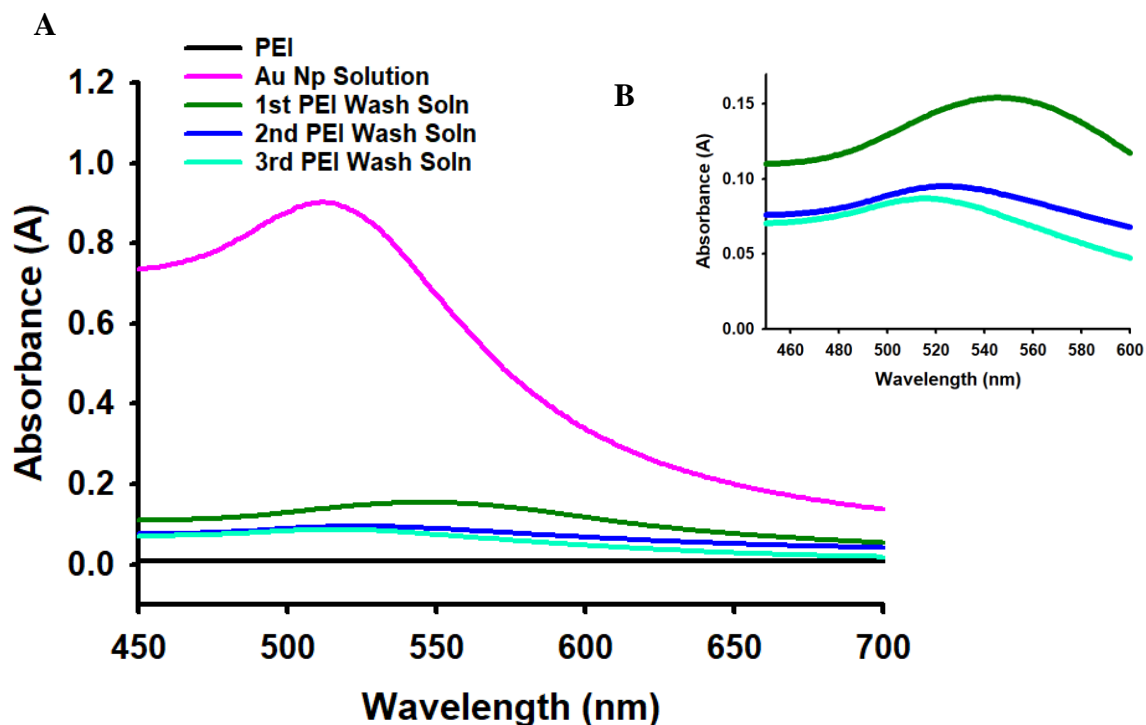


**Figure 2.5.** UV-Visible spectra of Au Nps solution used in the adsorption step (pink), PEI solution (black line), and solutions containing PEI after each washing step

#### *Au Np adsorption (Au @SiO<sub>2</sub> films)*

To prepare the Au@SiO<sub>2</sub> films, the washed PEI@SiO<sub>2</sub> films were twice immersed in 7 mL of as-prepared aqueous Au Np solution for 2 hours each immersion. Au Np adsorption occurs while protected from light and is assisted with orbital stirring in fresh Au Np solution at each step. The produced Au@SiO<sub>2</sub> films were then gently washed to remove excess gold, and then dried under nitrogen gas. UV-visible spectroscopy was also used to optimize the number of steps required to saturate the surface of the modified PEI@SiO<sub>2</sub> film. After each step, an aliquot of the Au Np solution was removed from the immersion and analyzed with UV-Vis absorbance, assuming that the peak curve for the Au Nps before and after immersion will be similar (Figure 2.6).

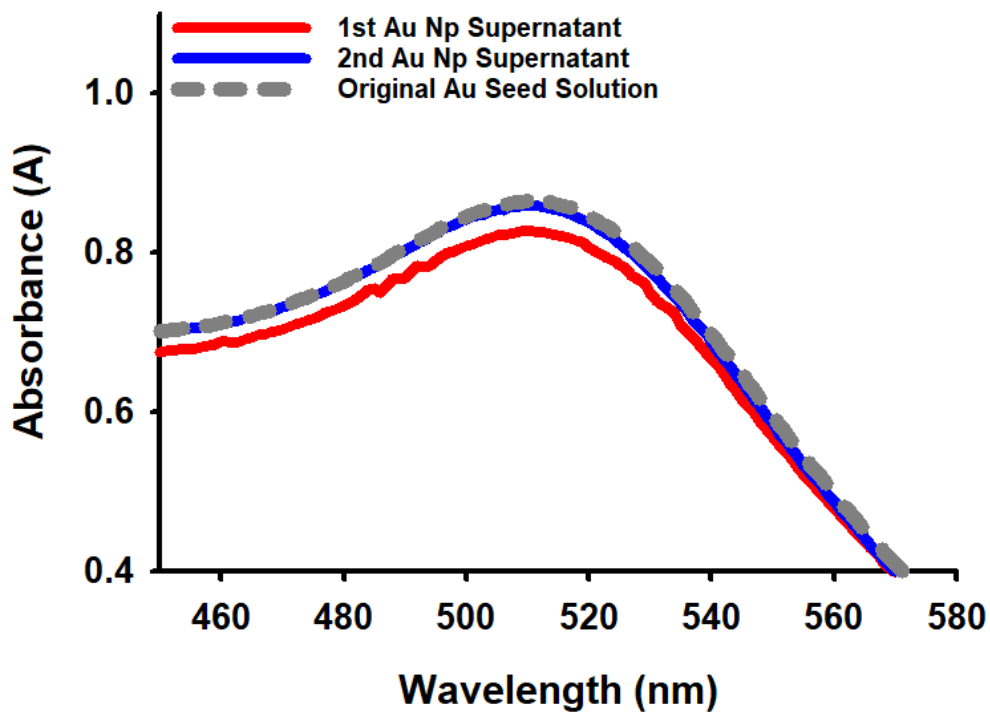


**Figure 2.6.** UV-Visible spectra of Au Np solution used for the preparation of Au@SiO<sub>2</sub> substrates (broken grey line) and after a first (red) and second (blue) adsorption step.

As shown in Figure 2.6, after two immersions, there is minimal variance in the absorbance in comparison to the Au Np solution. Similar results were obtained with three different substrates. To simply show the proof of concept, Figure 2.6 only shows this process for one sample.



## Chapter 3: Nanomaterials and Films Characterization Studies

SiO<sub>2</sub> particles and Au Nps were synthesized using the methods described in Chapter 2. The as-synthesized materials after characterization were used to prepare SiO<sub>2</sub>-based pastes to fabricate Au@s-SiO<sub>2</sub> and Au@t-SiO<sub>2</sub> thin films. Pastes were prepared and applied using a screen-printing approach the same day that the paste was prepared and annealed at high 600 °C. PEI functionalized SiO<sub>2</sub> films were immersed in colloidal Au Nps solutions to produce Au@SiO<sub>2</sub> Au decorated SiO<sub>2</sub> particle films. The results of the characterization studies described in Chapter 2 are discussed below.

### 3.1. Au Nps and SiO<sub>2</sub> Particles

#### 3.1.1. SiO<sub>2</sub> Samples Characterization Results

As described in Chapter 2, SiO<sub>2</sub> particles were synthesized via a base-catalyzed Stöber method to generate material with two types of textures, solid (s-SiO<sub>2</sub>) and textured (t-SiO<sub>2</sub>) particles. A surfactant, CTAB, was added to the reaction media to inhibit the growth of the SiO<sub>2</sub> particles and introduce a textured surface on the SiO<sub>2</sub> particles. The samples of t-SiO<sub>2</sub> went through multiple washes in acetone to remove the surfactant and maintain access to surface pores. The residual masses for s-SiO<sub>2</sub> and t-SiO<sub>2</sub> after combustion of organic capping ligands (Figure 2.1) are summarized in Table 3.1 along with a representative value from the literature.

**Table 3.1.** TGA results for textured and solid SiO<sub>2</sub> synthesized in this work.

Material	Mass Loss (%) at 1000 °C
s-SiO <sub>2</sub>	2 to 3
t-SiO <sub>2</sub>	10.7 (5.64 [77])

Gundanna et al. [79] studied the decomposition of pristine CTAB and reported the temperature window as 220 °C to 320 °C. The combustion of CTAB may have occurred during the second mass loss step; the consecutive steps can be attributed to continued content loss. As shown, in Figure 2.1, the changes in the curve for t-SiO<sub>2</sub> allows to identify all those mass loss steps, a first mass loss step in the temperature range of 100 °C to 200 °C; this mass loss of 1.0% is due to vaporization of adsorbed moisture. Following by subsequent steps at 200 °C to 400 °C (2.7%), 400 °C to 550 °C (3.7%) and then the slope of the curve begins to approach zero as the temperature approaches 800 °C (3.3%). The SiO<sub>2</sub> product inevitably contains active silanol groups due to incomplete hydrolysis and condensation reactions during synthesis. In a related study done by Javdani and collaborators, CTAB was one of the surfactants used as template to form mesoporous SiO<sub>2</sub> nanoparticles sized ~100 nm. The team employed five methanol washes to remove the CTAB from the porous surface and quantified the CTAB content (5.64%) using TGA [80]. The thermogram in Figure 2.1. shows a larger mass loss of CTAB on the t-SiO<sub>2</sub> in comparison to the literature (Table 3.1.), which raises the concern of whether the residual CTAB on the t-SiO<sub>2</sub> may impact the texture of the as prepared materials, and the preparation of pastes and films. This can be answered by obtaining the surface area of the t-SiO<sub>2</sub> before and after calcination near the temperature of combustion for CTAB.

### *Surface analysis*

To analyze the impact of the surface properties of the SiO<sub>2</sub> samples on the properties of the SiO<sub>2</sub> particles substrates and the SERS performance of the Au@SiO<sub>2</sub> substrates, nitrogen adsorption/desorption experiments were performed to determine the

Brunauer-Emmett-Teller (BET) surface area of the synthetic products. Typical nitrogen adsorption isotherms for s-SiO<sub>2</sub> and t-SiO<sub>2</sub> powder samples are shown in Figures 3.1A and B.

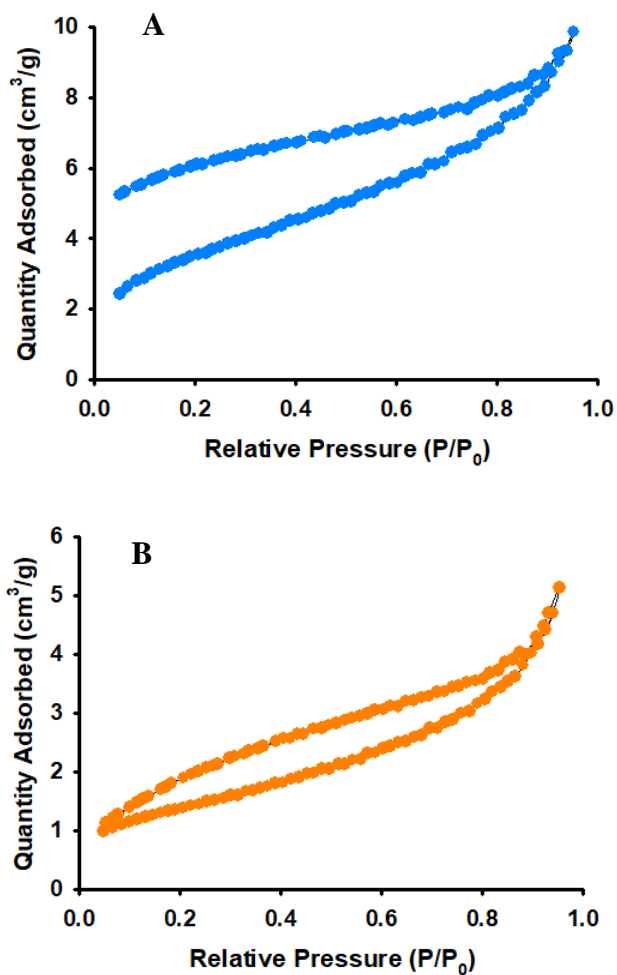


**Figure 3.1.** Nitrogen adsorption isotherm for samples of (A) s-SiO<sub>2</sub> and (B) t-SiO<sub>2</sub> at 77K

The nitrogen adsorption isotherms (77 K) collected for t-SiO<sub>2</sub> and s-SiO<sub>2</sub> particles can be analyzed using the IUPAC classification (microporous (type I), nonporous or macroporous (types II, III, and VI), or mesoporous (types IV and V)) [81].

The nitrogen adsorption plot for the s-SiO<sub>2</sub> particles indicates a non-porous structure (Type II isotherm). Despite being unexpected, the textured counterpart similarly displays a Type II isotherm typical of a solid material.

The surface area determination was carried out using the BET equation:

$$\frac{1}{W\left(\frac{P^0}{P}-1\right)} = \frac{1}{W_m \cdot C} + \frac{C-1}{W_m \cdot C} \left(\frac{P}{P^0}\right) \quad (3-1)$$

where W is the weight of gas adsorbed at the relative pressure of  $P/P_0$ ,  $W_m$  is the weight of the adsorbate at a monolayer capacity used to estimate the surface area, and the BET constant, C, accounts for the interactions between the sample and the adsorbate gas.

Therefore, if the mass of sample and the cross-sectional area of the adsorbate gas (N<sub>2</sub>, 16.200 Å<sup>2</sup>/molecule) are known, then the BET plot allows for the derivation of the monolayer capacity and the material surface area (m<sup>2</sup>/g). Figure 3.2 shows the  $\frac{1}{W\left(\frac{P_0}{P}-1\right)}$

vs.  $P/P_0$  in the range  $P/P_0$  of 0.05 to 0.35. The characterization results are summarized in Table 3.2.

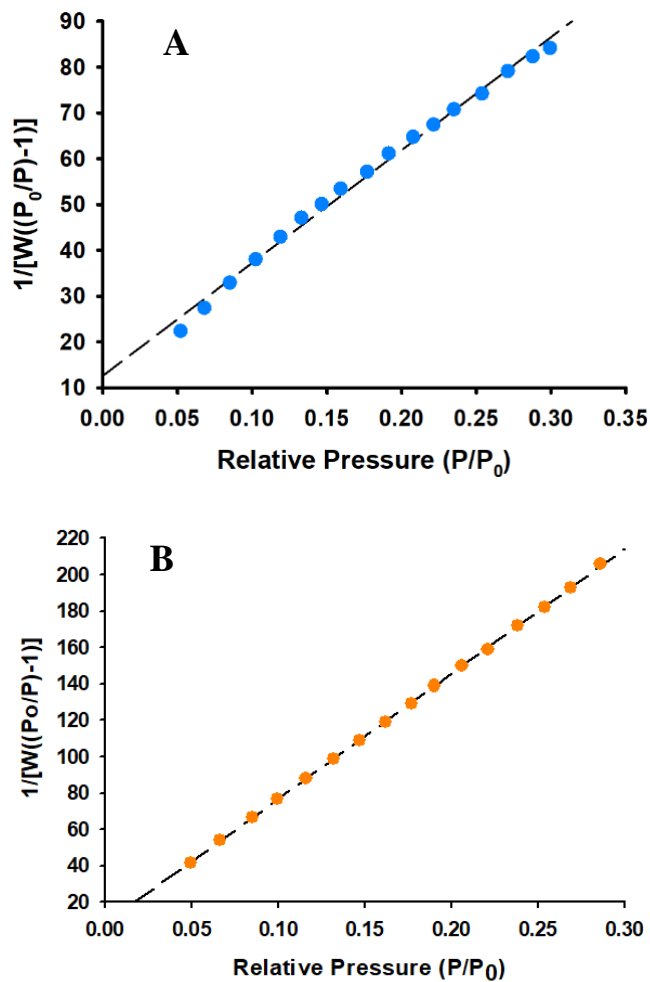


**Figure 3.2.** BET plot of the nitrogen adsorption on (A) s-SiO<sub>2</sub> on (B) t-SiO<sub>2</sub> at 77 K

**Table 3.2.** BET surface area for SiO<sub>2</sub> particles used throughout this study

SiO <sub>2</sub> Type	Surface Area (m <sup>2</sup> /g)
s-SiO <sub>2</sub>	12.7 (28.0 [73])
t-SiO <sub>2</sub>	5.0
t-SiO <sub>2</sub> (after heating one hour at 230 °C in air)	7.3
Commercial m-SiO <sub>2</sub>	278

As expected the s-SiO<sub>2</sub> particles have a surface area in the order of other SiO<sub>2</sub> samples prepared using the Stöber method as indicated in Table 3.2 [73]. Also, for solid SiO<sub>2</sub>, the BET surface area values are in very good agreement with calculated values obtained by assuming non-porous spheres with an average size of ~ 300 nm (see Figure 3.3) and a density of 2 g/cm<sup>3</sup> after considering that for SiO<sub>2</sub> particles obtained using the Stöber method, densities between 1.8 to 2.2 g/cm<sup>3</sup> have been reported) [73].

As summarized in Table 3.2, the surface area for t-SiO<sub>2</sub> is two orders of magnitude smaller than that for a commercial m-SiO<sub>2</sub> sample with similar particle diameter comparable to s-SiO<sub>2</sub>. The pre-treatment adopted for the BET surface area determination, 6 hours under vacuum at 200 °C, was not the reason for the observed results, because there was no difference on the surface area of a representative t-SiO<sub>2</sub> sample, before and after calcination under air in a tubular oven at 230 °C. This is surely associated to the CTAB to TEOS ratio used in this study as it was below the optimal range for obtaining a mesoporous structure [82, 83]. The amount of CTAB used is less than the critical micellar concentration (CMC) required for spontaneous formation of CTAB micelles in ethanol. In addition, it has been reported that the adsorption of CTAB can lead to aggregation of the SiO<sub>2</sub> particles with a significant reduction on surface area [84], as confirmed in this thesis.

### ***Particle size and textural properties***

TEM images of the as-prepared s-SiO<sub>2</sub> and t-SiO<sub>2</sub> particles are shown in Figure 3.3 and 3.4. As depicted in Figure 3.3(A), s-SiO<sub>2</sub> particles were quasi-monodispersed with a smooth surface texture. The particle size distribution (PSD) plot for s-SiO<sub>2</sub> is

shown in Figure 3.5 and is in good agreement with other studies related to silica particles obtained under similar experimental conditions [73]. An average particle size of  $324.51 \pm 46.18$  nm with a distribution of smaller and larger size nanoparticles was attained.

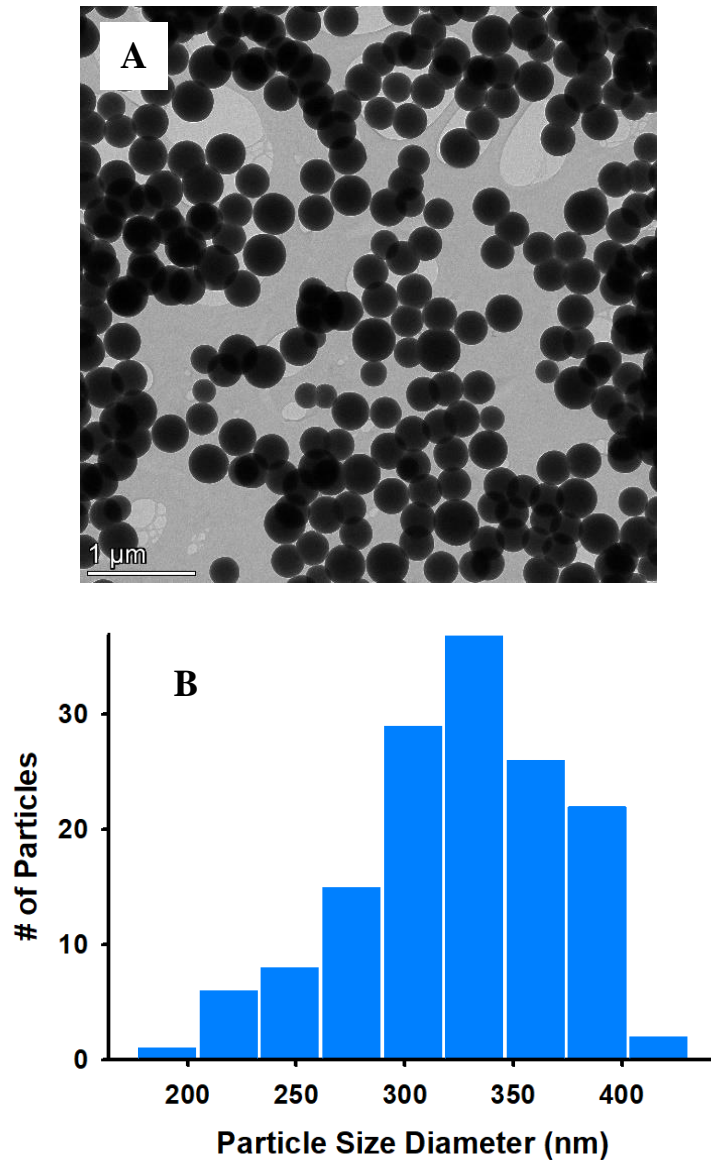


**Figure 3.3.** (A) TEM images of s-SiO<sub>2</sub>; Scale bar: 1 μm, and (B) particle size distribution analysis of synthesized s-SiO<sub>2</sub> particles using ImageJ software [85]

In the case of t-SiO<sub>2</sub> (Figure. 3.4), the presence of CTAB results in significant particle aggregation that forbid us to estimate an average particle size. However, the image in Figure 3.4B is clear evidence of textural differences between the two material.

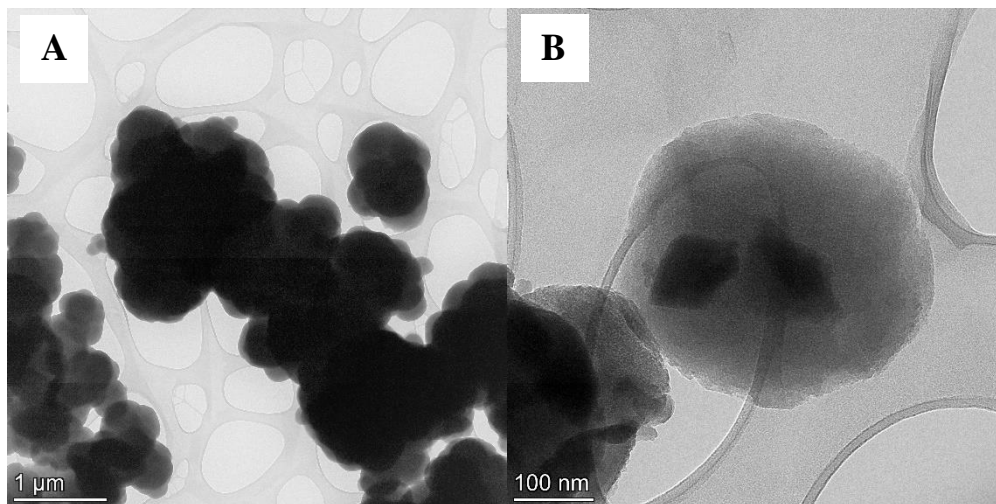


**Figure 3.4.** TEM images of t-SiO<sub>2</sub>; Scale bars: (A) 1 μm, (B) 100 nm

Additional TEM images of s- and t-SiO<sub>2</sub> particles are shown in Figure 3.5. The differences in surface texture in these samples is notorious and in good agreement with images reported in previous studies [48, 73].



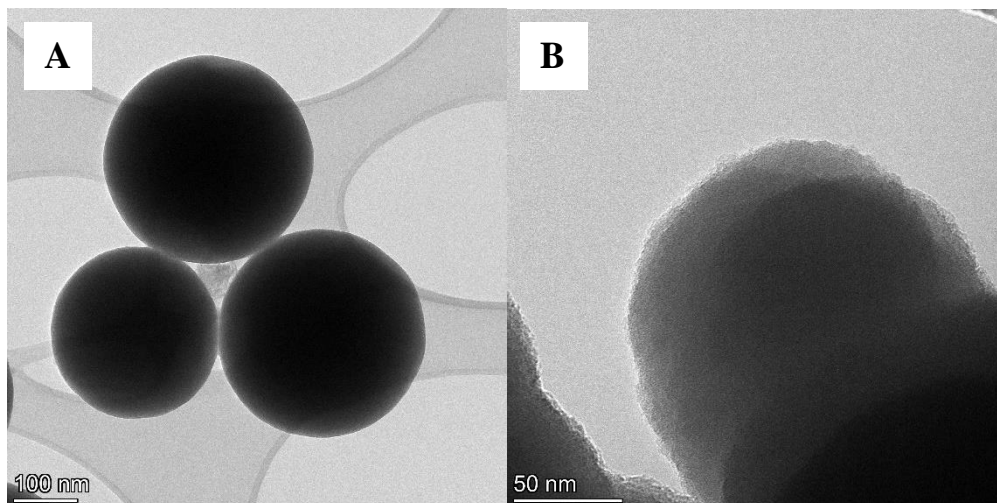


**Figure 3.5.** TEM images of (A) s-SiO<sub>2</sub>, (B) t-SiO<sub>2</sub>, Scale bars: (A) 100 nm, (B) 50 nm

### 3.1.2. Au Nps: Particle Size Analysis

TEM imaging is probably the best alternative to monitor the size of Au Nps; however, it has been shown in other studies, that UV-Visible spectroscopy can also provide an estimation of the Au Np size [10, 86, 87]. Herein, TEM was used to confirm the capability of UV-Visible spectroscopy for establishing the size of the Au Nps after each synthesis. TEM images of citrate-capped Au Nps are displayed in Figure 3.6A. The Au Nps were dispersed well, allowing for the PSD to be analyzed (Figure 3.6B).

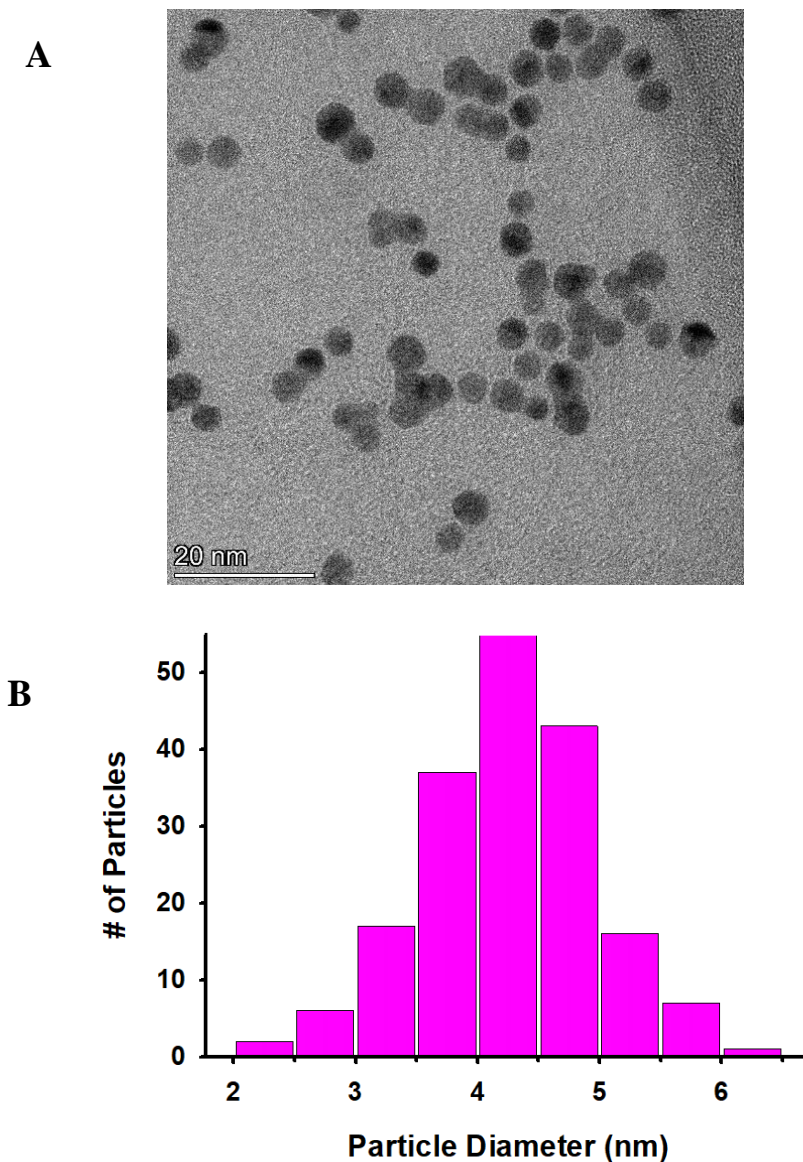


**Figure 3.6.** (A) TEM image of colloidal Au Nps sized (3-5 nm); Scale bar: 20 nm. (B) PSD analysis of Au Nps in TEM image completed with 53 spherical particles on the ImageJ software [85].

The Au Nps are spherical in shape. The analysis of the PSD reveals that the average diameter size in the Au Np in the colloidal solution is  $4.25 \pm 0.68$  nm, agreeing with other studies where a similar synthetic approach has been used [88, 89]. The position of the surface plasmon absorption maximum for Au Nps is directly influenced by its particle size, interparticle distance and interactions, and the dielectric properties of the

local environment [90]. In Figure 3.7, the Au Nps solution shows a well-defined absorbance band centered at 511 nm which is typical of spherical non-aggregated Au Nps of 5 nm diameter size [87, 90].

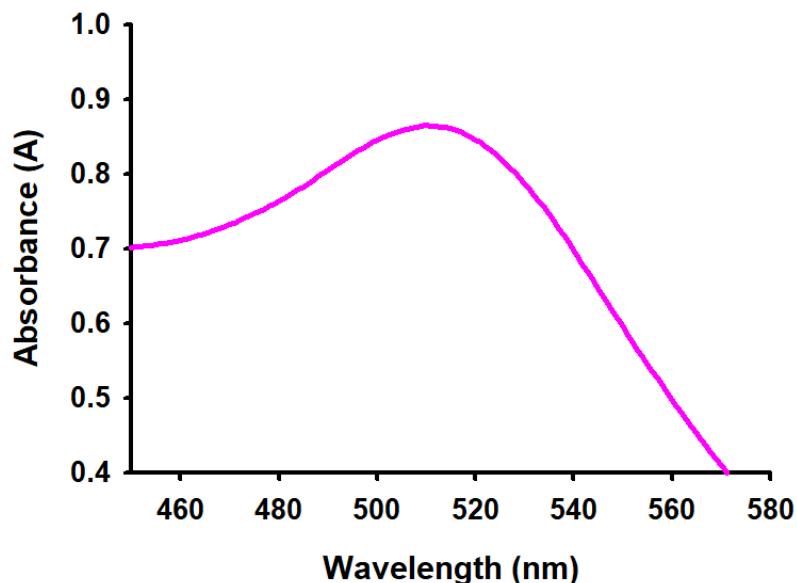


**Figure 3.7.** UV-Vis absorption spectrum of aqueous colloidal Au Nps sized 3-5 nm

The extinction efficiency is dependent on the surface plasmon resonance wavelength of the Au Np for sizes between 2.5 and 100 nm; and the position of the surface plasmon resonance peak increases with increasing diameter size [91].

The good agreement with the wavelength position of the maximum plasmon absorbance for the Au nanoparticles in solution was taken as an indication that UV-visible measurements could be used as a good estimation of the reproducibility of the synthetic approach, and Au loadings on the silica films, mainly in the case of well-dispersed nanoparticles as a consequence of the electrostatic repulsive forces introduced by the citrate capping ligand [92].

Haiss et. al [91] established an equation to determine the particle size of Au Nps from 5-50 nm based on the SPR absorbance of the material,  $A_{spr}$ , the initial concentration of Au,  $c_{Au}$  used in its synthesis, and TEM independent studies for the determination of accurate particle size. The proposed equation to estimate the average particle size,  $d$ , is defined below:

$$d = \left( \frac{A_{spr}(5.89 \times 10^{-6})}{c_{Au} \exp(C_1)} \right)^{1/C_2} \quad (3-2)$$

where  $C_1$  and  $C_2$  are empirical fitting parameters. It has been proposed that using the molar volume and the density of Au Nps in combination with the regression equation; the experimental values ( $C_1 = -4.75$ ,  $C_2 = 0.314$ ) can be optimized and the error in the calculated particle diameters reduced to ~6%. In this thesis, the average value obtained for three independently syntheses of Au Nps came to  $4.73 \pm 1.06$  nm (experimental parameter values), and  $4.32 \pm 1.01$  nm (optimized equation). An illustration of the similarities amongst the calculated diameter values determined with experimental parameters, theoretical parameters, and TEM analysis is shown in Figure 3.8. The calculated values fall within the range of the particle diameter sizes found through TEM analysis. For this reason, the UV-Visible spectra of the synthesized Au Nps was used as a fast size characterization method of the Au Nps obtained after each synthesis.

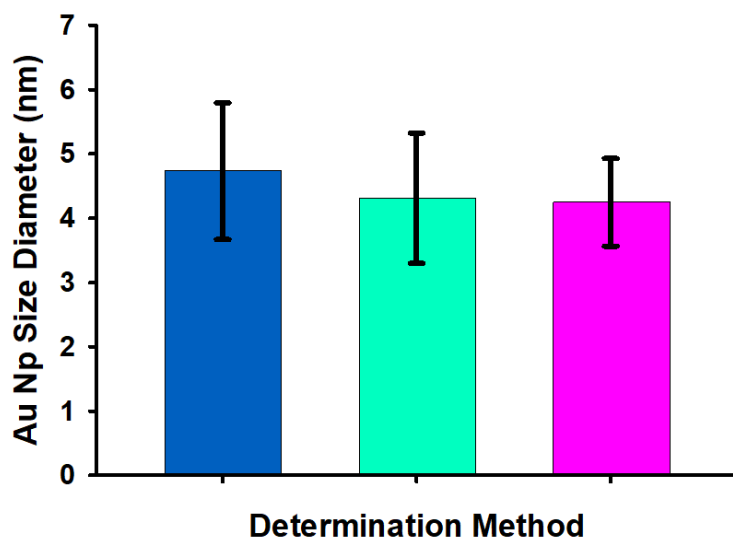


**Figure 3.8.** Average particle size for Au Nps in solution obtained using TEM images (pink), and Eq. 3-2 with experimental  $C_1$  and  $C_2$  parameters (blue) and optimized  $C_1$  and  $C_2$  constants (green). Particles obtained from three independent synthesis.

### 3.2. Rheological Properties of SiO<sub>2</sub> Pastes

The previously prepared SiO<sub>2</sub> particles were used to prepare the SiO<sub>2</sub> pastes to be used for the preparation of films on silica substrates using a screen-printing approach. The quality of the films obtained with this approach is strongly dependent on the rheological properties of the paste and consequently the paste formulation. A viscosity versus shear rate plot for SiO<sub>2</sub> pastes reported in the literature is shown in Figure 3.9 [77]. The formulation identified as the best combination is relatively simple (~ 50 wt% SiO<sub>2</sub> (filler), ~ 6 wt% ethyl cellulose (binder), and 44 wt%  $\alpha$ -terpineol (solvent)).

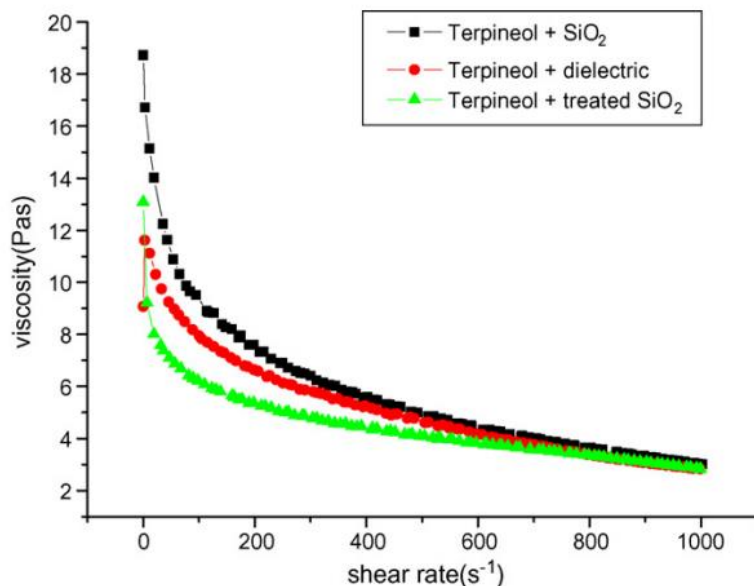


**Figure 3.9.** Viscosity vs. shear rate curve for literature paste systems containing 50 wt% of filler (3  $\mu\text{m}$   $\text{SiO}_2$ , 3  $\mu\text{m}$  silane-functionalized  $\text{SiO}_2$ , or a dielectric powder) and the same binding agent (ethyl cellulose), and organic solvent ( $\alpha$ -terpineol) used in this work at 6 wt% and 44% respectively. Reprinted from J. Mater. Process. Technol., **197**, Lin, H.C., C.; Hwu, W.; Ger, M., *The Rheological Behaviors Of Screen-Printing Pastes*, p. 7., Copyright (2007), with permission from Elsevier.

However, preliminary experiments carried out with commercial fumed silica in this study showed that 50 wt%  $\text{SiO}_2$  result in very thick films with just one layer, then the silica content was reduced to  $\sim 20$  wt% to be able to produce thinner films, and be able to apply more than one layer that it is expected to will reduce the number of defects. Ethanol was also added to be able to get uniform pastes because of the differences in mill systems (Literature: three-roller mill, this work: ball mill). It was now vital to monitor the amount of ethanol in the paste that would enable non-Newtonian behaviour while limiting uncontrollable spreading during the screen-printing process. These preliminary results are shown in Figure 3.10.

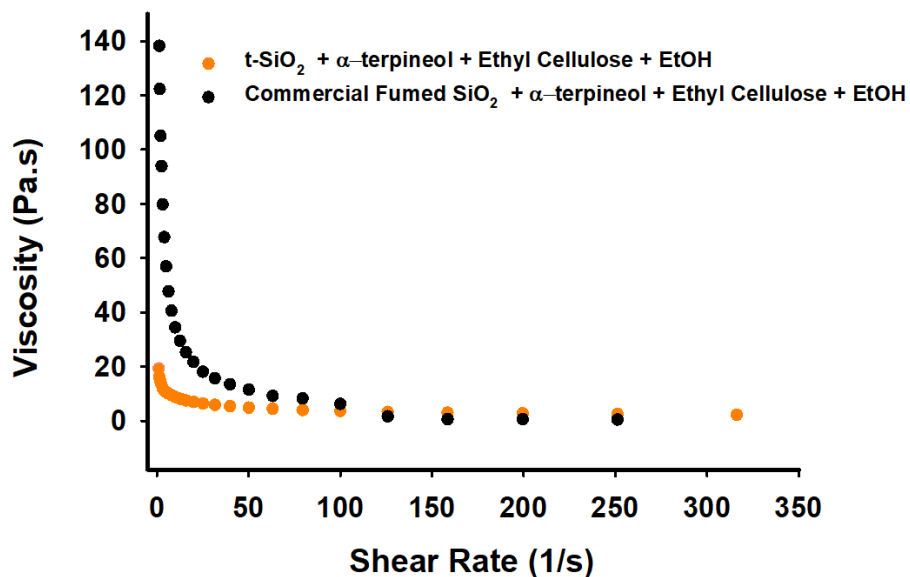


**Figure 3.10** Viscosity vs. shear rate curve for paste systems prepared with 20% t-SiO<sub>2</sub> particle filler (Orange) and 20% Commercial fumed SiO<sub>2</sub> (0.2-0.3 μm) (Black)

The viscosity vs shear rate curves obtained by Lin et al. [77] experiences a significant drop at a low shear rate, and continue to slowly decrease as the shear rate increases; it was reported as indicative of shear-thinning behaviour caused by weakly attracted interactions. The surface properties of the filler play an important role on the paste viscosity; thus, it was not expected for the solid-like particles synthesized to ~325 nm in this work or the porous particles purchased at ~ 240 nm to follow the exact curve of the literature which used a particle of a much larger diameter as a filler, nonetheless a similar trend was observed (Figure 3.10). The wt% SiO<sub>2</sub>: wt% EC was kept identical as reported in the literature work shown in Figure 3.9, and even with a lower wt% of filler, the decreasing viscosity pattern of the commercial fumed SiO<sub>2</sub>-based paste was similar to the paste system studied by Lin et al. The same was observed for the t-SiO<sub>2</sub> pastes, indicating that the paste was similar rheological behaviour to the fumed SiO<sub>2</sub> although, the curve is not expected to be identical as the filler in each paste is different and the

amount of ethanol may vary slightly between each system. Based on these preliminary studies, pastes with the formulation summarized in Table 3.3 were used for the preparation of all the films in this thesis.

**Table 3.3.** Composition of the initial SiO<sub>2</sub> paste and with the addition of ethanol

Reagent	Wt% (w/o EtOH)	Wt% (w/ EtOH)	Role
$\alpha$ -terpineol	70	64	Solvent
Ethyl Cellulose	10	9	Binding Agent
SiO <sub>2</sub> Np	20	18	Filler
Ethanol	---	9	Co-solvent

### 3.3. SiO<sub>2</sub> and Au@SiO<sub>2</sub> Films Physical Characterization Studies

The morphological properties of each SiO<sub>2</sub> film prior to deposition is important to analyze the impact of the inert silica support on the SERS performance of Au Nps. Profilometry was used to measure the film thickness and, obtaining the arithmetic average deviation (Ra) using 3-D surface topographic data to investigate differences in surface roughness:

$$Ra = \frac{1}{n} \sum_{i=1}^n |y_i| \quad (3-3)$$

where n, is the number of measurements, and y is the absolute value of profile departure (film height) [93]. 3D profilometric images were obtained for screen-printed s-SiO<sub>2</sub> and t-SiO<sub>2</sub> films after calcination at 600 °C before and after Au Nps adsorption. Tables 3.4



and 3.5 summarizes these surface morphological features; the profilometer images can be found in Appendix A2.

**Table 3.4.** Summary of film topographic morphology for screen-printed two-layer SiO<sub>2</sub> films on glass slides.

Type of SiO <sub>2</sub>	Roughness/Ra (μm) <sup>#</sup>	Thickness (μm) <sup>#</sup>
Solid Surface Structure	0.378 ± 0.001	2.35
Textured Surface Structure	0.627 ± 0.022	4.28

<sup>#</sup> Average of two determinations

**Table 3.5.** Summary of film topographic morphology for Au@s-SiO<sub>2</sub> and Au@t-SiO<sub>2</sub> films

Au@SiO <sub>2</sub> film	Roughness/Ra (μm) <sup>#</sup>	Thickness (μm) <sup>#</sup>	Estimated Au Nps layer thickness (μm)
Solid Surface Structure	0.244 ± 0.001	4.35	2.00
Textured Surface Structure	0.567 ± 0.007	6.06	1.78

<sup>#</sup> Average of two determinations

As presented in Table 3.4, the Ra value for the t-SiO<sub>2</sub> films at 0.627 ± 0.022 μm is noticeably higher by ~60% in comparison to the s-SiO<sub>2</sub> films that have a Ra value of 0.378 ± 0.001 μm. It is anticipated that there is a random distribution of SiO<sub>2</sub> particles within each film which will generate interparticle gaps and the SEM images of the s-SiO<sub>2</sub> film in Figure 3.11 and t-SiO<sub>2</sub> film in Figure 3.12 clearly show the differences.

The t-SiO<sub>2</sub> films exhibit enhanced roughness due to the occurrence of naturally larger aggregates in the starting SiO<sub>2</sub> materials and consequently in the final films; this is surely the reason for the differences in roughness and film thickness between t- and s-SiO<sub>2</sub>.

Once the Au Nps are deposited onto the SiO<sub>2</sub> films, there is a 37% and an 8% reduction in the surface roughness for Au@s-SiO<sub>2</sub> ( $R_a = 0.244 \pm 0.001 \mu\text{m}$ ) and Au@t-SiO<sub>2</sub>, ( $0.567 \pm 0.007 \mu\text{m}$ ), respectively.

The thickness of the s-SiO<sub>2</sub> film was nearly 7 times the average size of the individual s-SiO<sub>2</sub> particles (Figure 3.3), confirming that the coating of the SiO<sub>2</sub> is a multilayer system. Comparing the two particle films, the t-SiO<sub>2</sub> films are approximately 2  $\mu\text{m}$  thicker than the s-SiO<sub>2</sub> films; the SEM images in Figure 3.12 shows a larger number of aggregates of varying sizes which is not observed for the s-SiO<sub>2</sub> (Figure 3.11) demonstrating that the particle size will change the film morphology. Based on other studies, it is expected that the SiO<sub>2</sub> films structure will have a unique effect on the surface plasmon excitation effect of Au Nps [12].

Although both the Au@s-SiO<sub>2</sub> and Au@t-SiO<sub>2</sub> were prepared with the exact same procedure, the loading of Au Nps may have led to the formation of larger Au nanostructures on the s-SiO<sub>2</sub> film than on the t-SiO<sub>2</sub> film as indicated by the difference in film thickness between the two systems after Au deposition. The differences will impact the SERS activity of these two substrates based on other studies [12, 51, 53, 94, 95]. Quantifying the Au Nps on the film will also better conclude that. Semi-quantification of the film Au content can be done using EDX analysis.

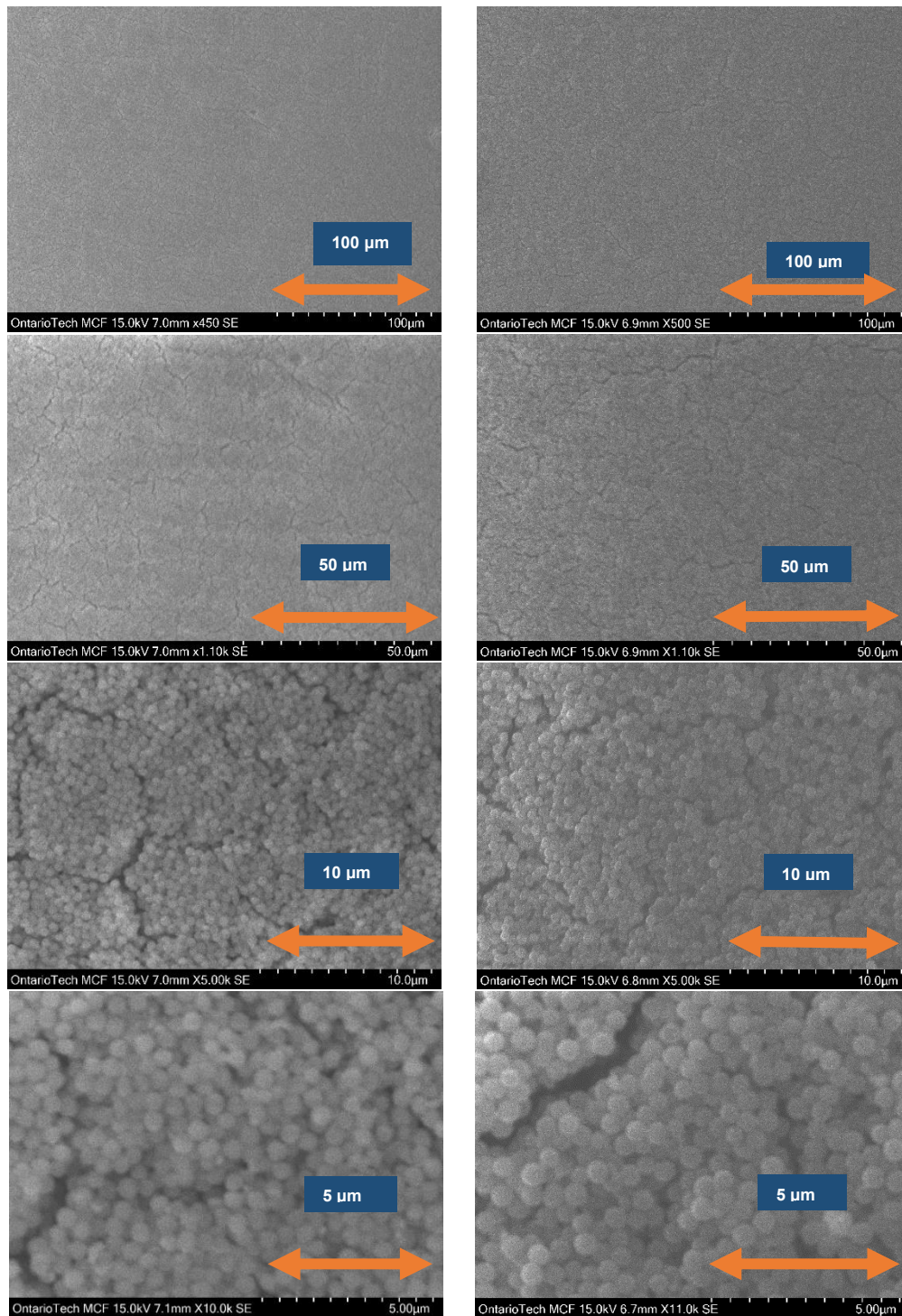


**Figure 3.11.** SEM images of a s-SiO<sub>2</sub> film surface before (left) and after Au adsorption (right).

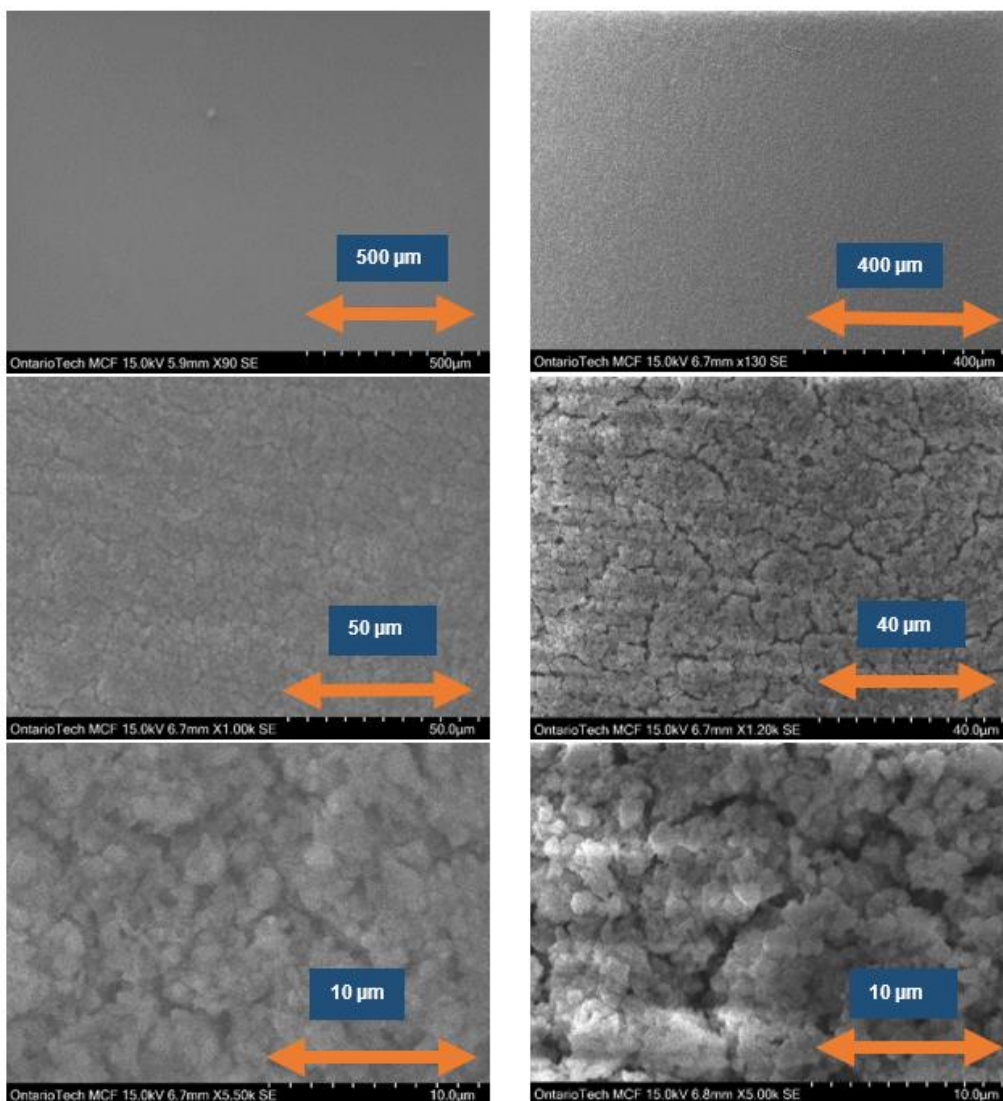


**Figure 3.12.** SEM images of a t-SiO<sub>2</sub> film surface before (left) and after Au adsorption (right).

***EDX analysis for surface content qualitative analysis***

The elemental composition was determined by energy-dispersive X-ray (EDX) spectroscopy analysis to gain insight towards the Au Np content on the Au@SiO<sub>2</sub> films. The EDX spectra shows the points of where a specific element exists, which provides a distribution of material on the selected area. This is shown for Au@SiO<sub>2</sub> films composed

of s-SiO<sub>2</sub> in Figure 3.13 and t-SiO<sub>2</sub> particles in Figure 3.14. Only the major constituents are highlighted in both figures.

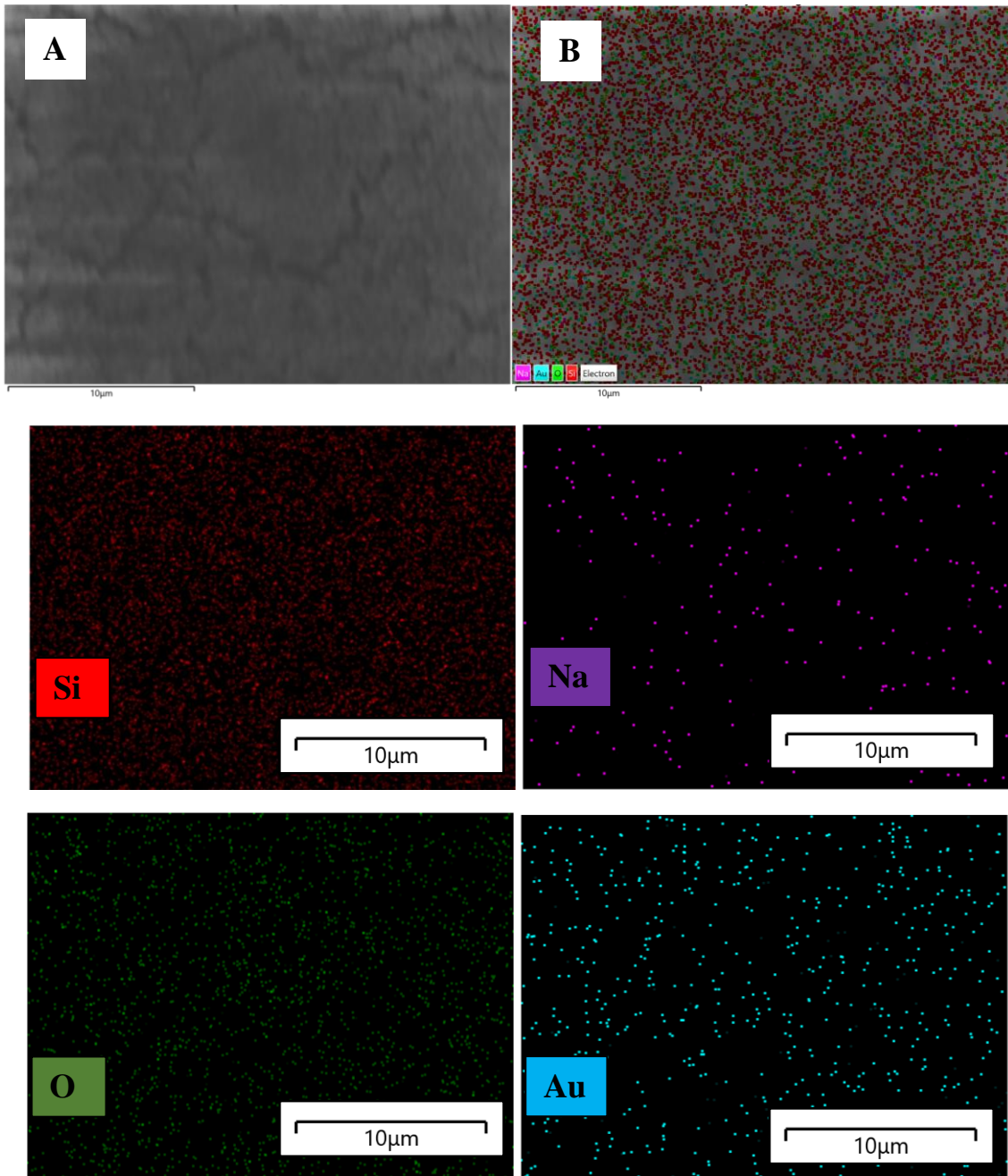


**Figure 3.13.** Surface morphology and elemental mapping of the Au@s-SiO<sub>2</sub> nanostructured film. Top: (A) Electron SEM image (B) EDX layered image and Bottom: corresponding elemental mapping via energy-dispersive X-ray spectroscopy semi-quantitative analysis.

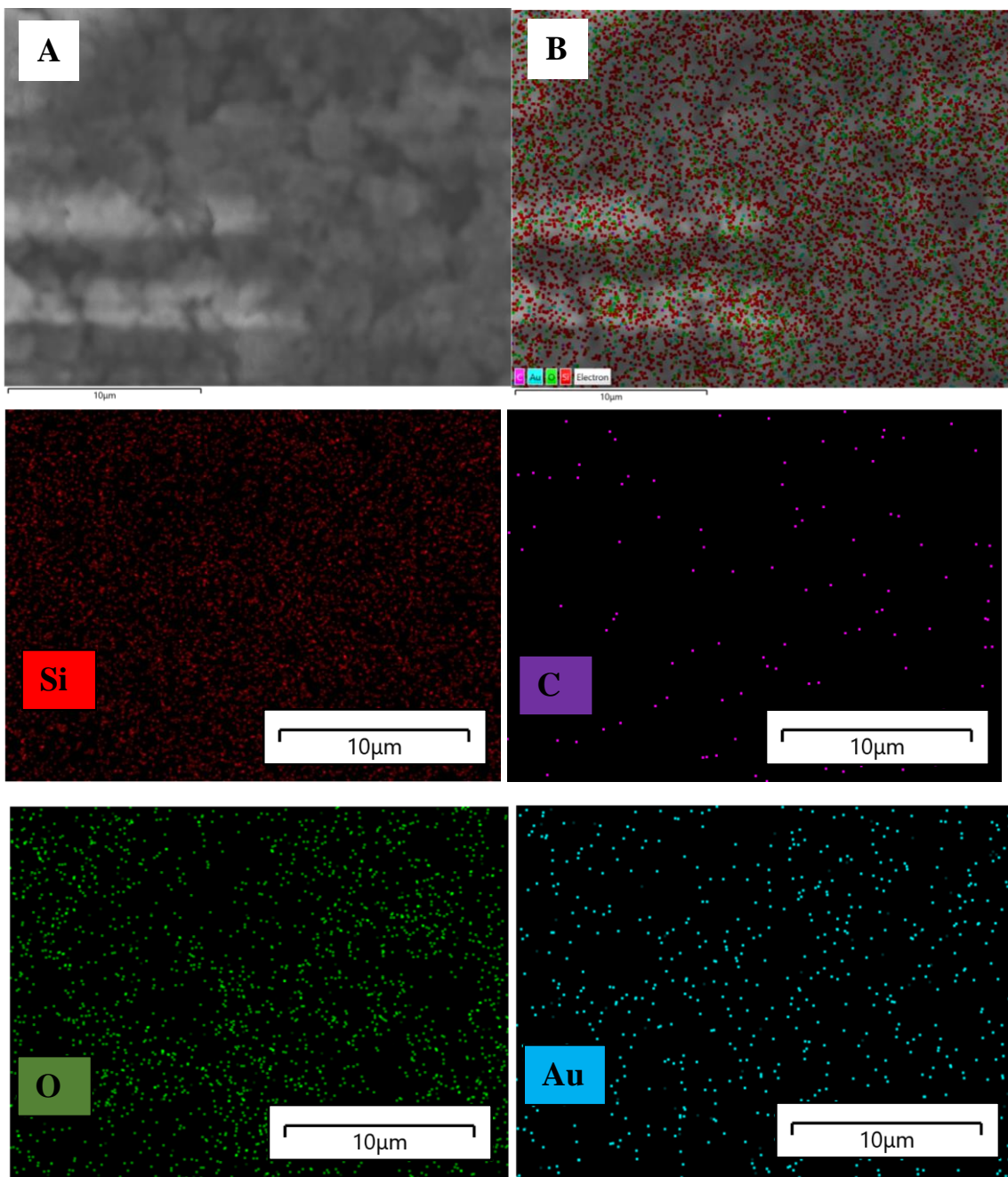


**Figure 3.14.** Surface morphology and elemental mapping of the Au@t-SiO<sub>2</sub> nanostructured film. Top: (A) Electron SEM image (B) EDX layered image and Bottom: corresponding elemental mapping via energy-dispersive X-ray spectroscopy semi-quantitative analysis

EDX analysis was used to estimate the elemental composition of the films (surface). Both Au@t-SiO<sub>2</sub> and Au@s-SiO<sub>2</sub> films were examined at three different samples. A summary of the average weight percent (wt%) composition for the films analyzed are shown in Table 3.6 for Au@s-SiO<sub>2</sub> and Table 3.7 for Au@t-SiO<sub>2</sub>. For both the Au@t-SiO<sub>2</sub> and Au@s-SiO<sub>2</sub> films, Au is shown to be evenly distributed where there is large accumulation of particles and limited detection of Au was observed in the crevices. The composition analysis confirms that Au, Si and O are present on the film which is surely associated to the SiO<sub>2</sub> particles in the film, even when it is worth noting that films are deposited on glass slides. The Si: O ratio is nearly 1:1, while the relative amount of Au to Si by wt% is nearly 1:4. Carbon and sodium are surely the result of contamination associated to the use of sodium citrate as capping ligand in the preparation of Au Nps for stabilization.

**Table 3.6.** EDX composition analysis of 3 sample Au@s-SiO<sub>2</sub> films

<b>Element</b>	<b>Weight (%)</b>
Oxygen	44.43
Silicon	43.43
<b>Gold</b>	<b>11.83</b>
Sodium	0.33

**Table 3.7.** EDX composition analysis of 3 sample Au@t-SiO<sub>2</sub> films

<b>Element</b>	<b>Weight (%)</b>
Oxygen	44.53
Silicon	43.10
<b>Gold</b>	<b>10.17</b>
Sodium	0.13
Carbon	2.03

On average the wt% of Au on Au@s-SiO<sub>2</sub> in comparison to Au@t-SiO<sub>2</sub> is slightly higher, 12 wt% vs 10 wt%, respectively. This would suggest that any difference in SERS performance between the two substrates may be linked more likely to the distribution of Au on the porous structure of the SiO<sub>2</sub> films than to the Au content itself.

### *Au loadings on SiO<sub>2</sub> films*

The slight broadening and red shift of the maximum of absorbance in the 550-700 nm range in the spectrum of a representative Au@SiO<sub>2</sub> film (Figure 3.15) indicates the formation of Au Nps aggregates at the surface of the SiO<sub>2</sub> films. With aggregation, the inter-particle distance of Au Nps is decreased, introducing the dipole-dipole interactions between particles that result in a red shift in the SPR wavelength and eventually stronger SERS intensity. The differing curves displayed by each sample suggests that the distribution of the Nps are not exactly alike. The film shows an absorbance peak ~480 nm and a peak at ~560 nm. Every analyzed sample of the Au@SiO<sub>2</sub> films contain these distinct peaks with ranging intensity strength.

Studies have shown that the refractive index of the surrounding medium of Au Np samples will influence the surface plasmon resonance wavelength and the absorbance [91]. Furthermore, transitioning from Au Nps in water to Au Nps adsorbed on functionalized SiO<sub>2</sub> in air, will affect the absorbance exhibited by the material.



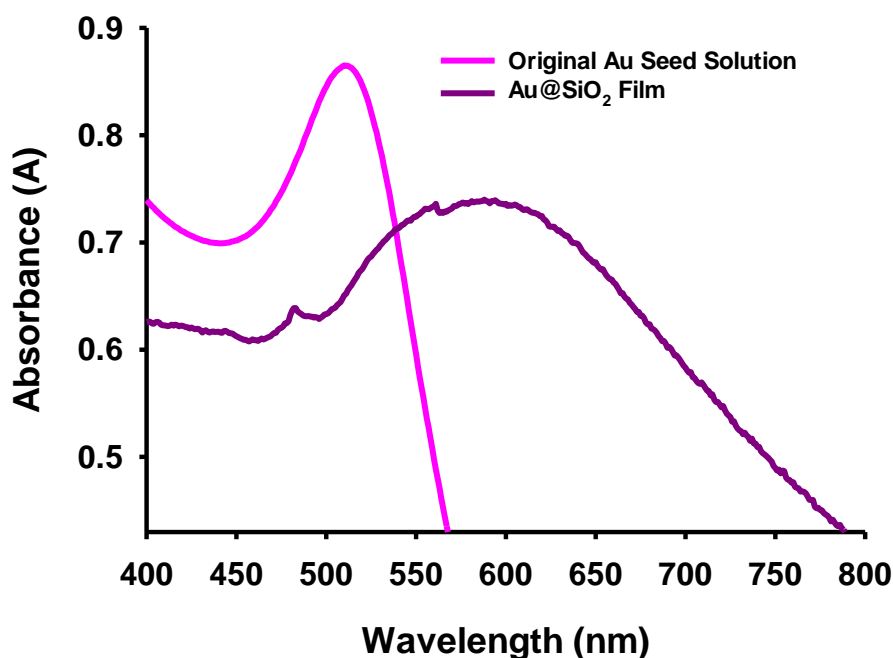


**Figure 3.15.** UV-visible absorption spectrum of aqueous colloidal Au Nps (sized 3-5 nm) and a representative Au@SiO<sub>2</sub> film

### *Conclusions for this chapter*

In conclusion, two 3D rigid screen-printed thin film substrates were fabricated and characterized. Two types of SiO<sub>2</sub> microspheres were used to prepare pastes: solid and textured surface SiO<sub>2</sub> spheres, the latter prepared in the presence of CTAB. The particle diameter sizes of the SiO<sub>2</sub> particles and Au Nps were examined with TEM imaging, where the t-SiO<sub>2</sub> images alluded to the formation of a textured surface and significant aggregation. The composition of the final screen-printing pastes prepared with these SiO<sub>2</sub> particles was ideal for the preparation of almost defect-free films as shown by the low magnification SEM images included in this chapter.

After annealing, s-SiO<sub>2</sub> and t-SiO<sub>2</sub> films were fully characterized. The thickness and roughness were determined by optical profilometry, SiO<sub>2</sub> particle film structures and

Au distribution/Au content determined by SEM/EDX analysis. These are preliminary assessments; the film porosity and Au content must be studied further with more sensitive techniques in the future, for instance ellipsometric porosimetry, and inductively coupled plasma - mass spectrometry (ICP-MS).

## **Chapter 4: Au@s-SiO<sub>2</sub> and Au@t-SiO<sub>2</sub> SERS Evaluation**

This chapter summarizes the studies carried out to evaluate the performance of SERS substrates prepared and characterized using the materials and methods described in Chapters 2 and 3. Au@s-SiO<sub>2</sub> and Au@t-SiO<sub>2</sub> films deposited on glass slides using screen-printing. These substrates were characterized using an inVia Renishaw system with a 532 nm excitation laser, and rhodamine 6G (R6G) as a target analyte (Section 1.7).

### **4.1. SERS Evaluation of Au@s-SiO<sub>2</sub>/silica and Au@t-SiO<sub>2</sub>/silica Substrates**

There have been previous studies regarding successfully functionalizing SiO<sub>2</sub> Nps with PEI to create an Au Nps shell around amino-functionalized SiO<sub>2</sub> particles. With that being said, to the best of our knowledge, there are little to no studies investigating the SERS performance of this type of system on screen-printed SiO<sub>2</sub> particle film on silica slides. For this reason, a performance assessment for both Au@s-SiO<sub>2</sub>/silica and Au@t-SiO<sub>2</sub>/silica SERS substrates have been carried out using R6G to evaluate the impact of the SiO<sub>2</sub> particle surface and film properties on the SERS response and reproducibility in the same film and between different substrates.

### **4.2. SERS Analysis Using R6G - Adsorption Time Experiments to Define the Evaluation Conditions**

Preliminary time adsorption experiments were performed by immersing different Au@SiO<sub>2</sub> slides in 1  $\mu$ M R6G solution for 10 s, 30 s, 60 s, 120 s, and 300 s to set the best conditions for the SERS characterization studies (Figure 4.1).

The results show 5 minutes immersion time provides a strong signal in a reasonable time, and extending the immersion time will not represent a significant improvement. The slides were then immersed in the solution for 5 minutes, and then let to dry under the microscope in complete absence of light, after removing any excess of solution on the glass slide surrounding the Au@SiO<sub>2</sub> film, but without touching the Au film. The SERS experiments were completed with a Renishaw inVia Raman Spectrometer equipped with a 532 nm solid state laser source. Standard aqueous solutions of R6G were prepared in a concentration range of 10<sup>-3</sup> M to 10<sup>-8</sup> M. For the Raman acquisition spectra, the following conditions were used: 0.5% laser power of 50 mW nominal power (0.25 mW), 10 s exposure time, 10 accumulations, and 50x magnification.

#### **4.3. SERS Substrates Evaluation: Point-to-Point Signal Reproducibility**

One of the major problems faced when preparing Au film on functionalized glass substrates (Appendix A1) was the lack of signal reproducibility between samples, and the relatively high LoD (0.1 mM). For this reason, the first step in these studies was to analyze the SERS signal reproducibility of the Au@s-SiO<sub>2</sub>/silica and Au@t-SiO<sub>2</sub>/silica substrates and evaluate the LoD and LoQ.

Signal reproducibility was evaluated by collecting 8 spectra for a R6G (1 μM) solution at 8 different points, in a single slide, for a total of 6 individual samples of each type of substrate (Au@s-SiO<sub>2</sub> and Au@t-SiO<sub>2</sub>). The spectra are shown in Figures 4.2 and 4.3. Significant characteristic peaks are observed in both films at 613, 774, 1127, 1310, 1362, 1507, 1649, and 1573 cm<sup>-1</sup>, associated to C-C-C in plane bending, CH out plane

bending, CH in plane bending, C<sub>2</sub> stretching, C<sub>2</sub> stretching and 1573 cm<sup>-1</sup> is the result of CO stretching (Table 1.1).

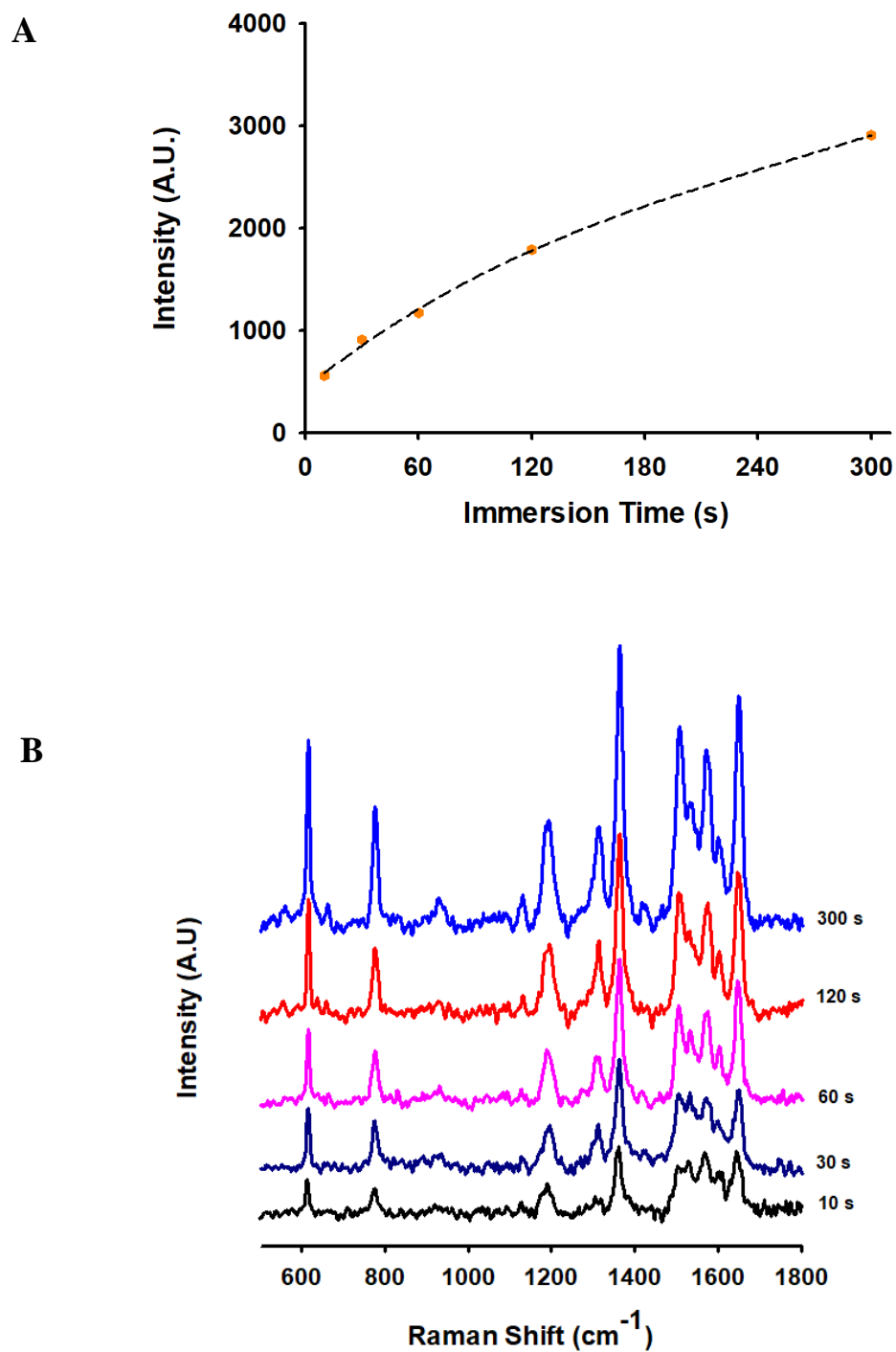


**Figure 4.1.** (A) SERS signal at 613 cm<sup>-1</sup> vs immersion time for R6G (1 μM R6G) and (B) SERS spectra for R6G (1 μM) at increasing immersion times (10, 30, 60, 120, and 300 s).

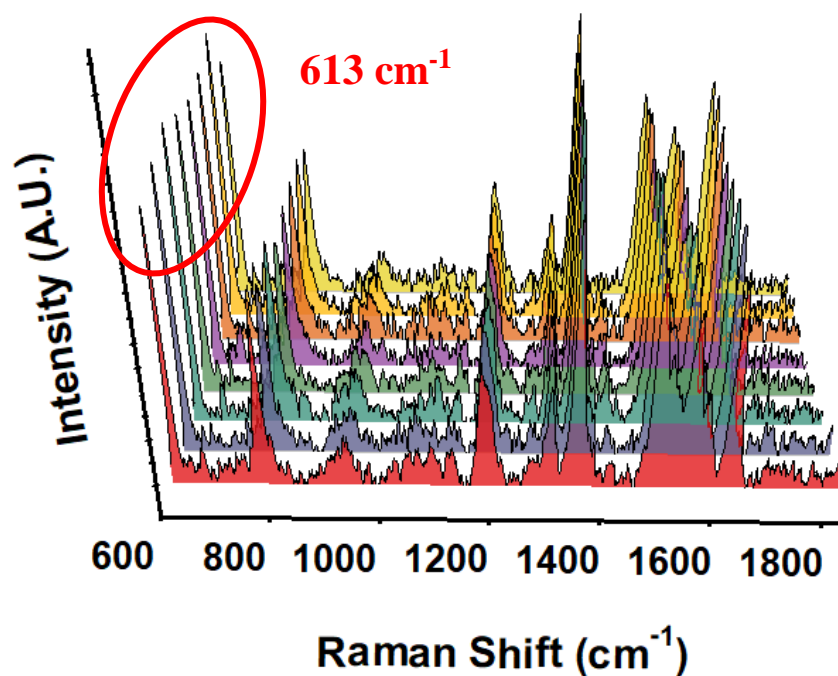


**Figure 4.2.** SERS spectra collected for 1  $\mu\text{M}$  of R6G at 8 randomly selected sites close to the centre of a representative Au@s-SiO<sub>2</sub> film. Acquisition parameters: 50 mW of 532 nm excitation at 0.5% power, 10 second integration for 10 accumulations 50x magnification

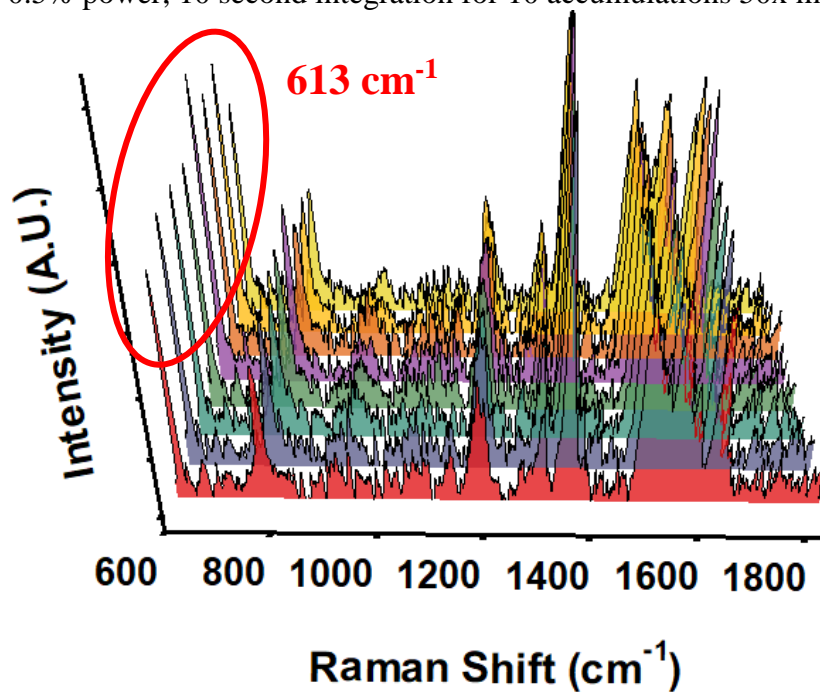


**Figure 4.3.** SERS spectra collected for 1  $\mu\text{M}$  of R6G at 8 randomly selected sites close to the centre of a representative Au@t-SiO<sub>2</sub> film. Acquisition parameters: 50 mW of 532 nm excitation at 0.5% power, 10 second integration for 10 accumulations 50x magnification

The band at 613  $\text{cm}^{-1}$  was used for the comparison, and the results are summarized in Tables 4.1 and 4.2 for Au@s-SiO<sub>2</sub>/silica and Au@t-SiO<sub>2</sub>/silica, respectively. The spectra were collected from 200  $\text{cm}^{-1}$  to 1900  $\text{cm}^{-1}$  at 0.5% laser power, 10 s exposure time, and 10 accumulations.

**Table 4.1.** Average absolute intensities of the 613  $\text{cm}^{-1}$  band measured for a 1  $\mu\text{M}$  R6G solution on multiple Au@s-SiO<sub>2</sub> films

<b>Average Abs. Intensity @ 613 <math>\text{cm}^{-1}</math></b>	<b>Standard Deviation</b>	<b>Relative Standard Deviation</b>	<b>Maximum</b>	<b>Minimum</b>
2071	204	10%	2281	1651
2797	456	16%	3692	2306
5365	201	4%	5661	5048
3200	218	7%	3430	2881
4511	360	8%	4970	3954
4738	259	5%	5084	4265

**Table 4.2.** Average absolute intensities of the 613  $\text{cm}^{-1}$  band measured for a 1  $\mu\text{M}$  R6G solution on multiple Au@t-SiO<sub>2</sub> films

<b>Average Abs. Intensity @ 613 <math>\text{cm}^{-1}</math></b>	<b>Standard Deviation</b>	<b>Relative Standard Deviation</b>	<b>Maximum</b>	<b>Minimum</b>
2732	535	20%	3586	2087
2069	250	12%	2490	1746
3098	1575	50%	4741	1193
2165	159	7%	2388	1901
3487	312	9%	3895	2983
4046	441	11%	4545	3255

As shown, the relative standard deviation (% RSD) values for the experiments with Au@s-SiO<sub>2</sub> are within 5 and 16% (Table 4.1), with an average intensity value of  $3776 \pm 270 \text{ cm}^{-1}$  and average % RSD of 8%. These results are in the range of literature

coefficient variation values reported for uniform substrates; this suggests that the repeatability for the Au@s-SiO<sub>2</sub> slides is good [56].

In contrast, the Au@t-SiO<sub>2</sub> substrates (Table 4.2) had much larger values for the coefficient of variation for individual slides; with reasonable low values, 7-12 % RSD, and extremely high % RSD, 20-50. The average % RSD for the Au@t-SiO<sub>2</sub> is 18% that includes one point with an extremely large % RSD value that is likely not representative of this group of samples. Based on other studies, this might imply that the distribution of hot-spots on the t-SiO<sub>2</sub> substrates may not be as uniform as the s-SiO<sub>2</sub> film.

### ***SERS Mapping***

Alternatively, the reproducibility on the SERS spectra was analyzed using SERS mapping to avoid arbitrarily selecting the points to be analyzed and any bias in the results. The automatic mapping method was used here to estimate the differences in the distribution of hot spots on the substrate surface. Unless stated otherwise, all Raman spectral images were collected with the same instrument with the following static scan conditions: 0.5% laser power of 50 mW nominal power, 10 s exposure time, 1 accumulation, and 50x magnification. These Raman measurement settings were chosen as a compromise to compensate for the long-time duration that comes with mapping, but it is likely that the signal-to-noise ratio in each measurement would not be as good as in the other determination where 10 accumulations and 10s exposure time were used for the spectra acquisition. Spectra were analyzed using Origin Pro 2022 software. SERS Mapping of the Au@s-SiO<sub>2</sub> films at 10 μM R6G concentrations are shown alongside Au@t-SiO<sub>2</sub> at the same concentration in Figure 4.4.



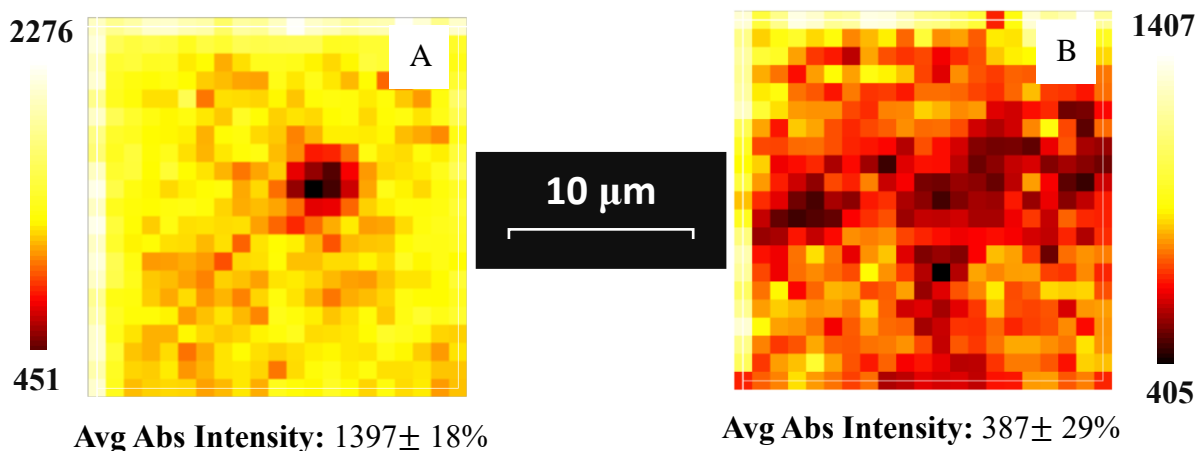


**Figure 4.4.** SERS mapping of R6G (10  $\mu\text{M}$ ) on (A) Au@s-SiO<sub>2</sub> and (B) Au@t-SiO<sub>2</sub> substrates. Analysis was completed on an area of 21 x 21  $\mu\text{m}^2$ .

The small square areas indicate the location where the analyte was probed using the intensity of the 613  $\text{cm}^{-1}$  band for the comparison, and the different colour scales represent differences in intensity between the given ranges (right and left scales). For constructing these mapping images, 441 spectra were collected with 1  $\mu\text{m}$  steps in an area of 21 x 21  $\mu\text{m}^2$ , 1 accumulation per spectra, and 10 second exposure time. The confidence interval is reported as % RSD, coefficient of variation.

In the case of the Au@s-SiO<sub>2</sub>, most of the area show high SERS intensity signals, when compared with the Au@t-SiO<sub>2</sub> for which many regions show very low SERS activity. The images are consistent with the differences in the coefficient of variations for the Au@s-SiO<sub>2</sub> and Au@t-SiO<sub>2</sub>, 18 and 29 % RSD, respectively. The larger % RSD values when compared with those in Tables 4.1 and 4.2 were assigned to the spectra collection conditions (0.5% laser power, 10 s exposure time, 1 accumulation). The differences exhibited between each film type can be associated to the less homogenous films in the case of t-SiO<sub>2</sub> (Figures 3.12). Additional SERS Mapping of the Au@s-SiO<sub>2</sub> films at different R6G concentrations are shown in Figure 4.5.

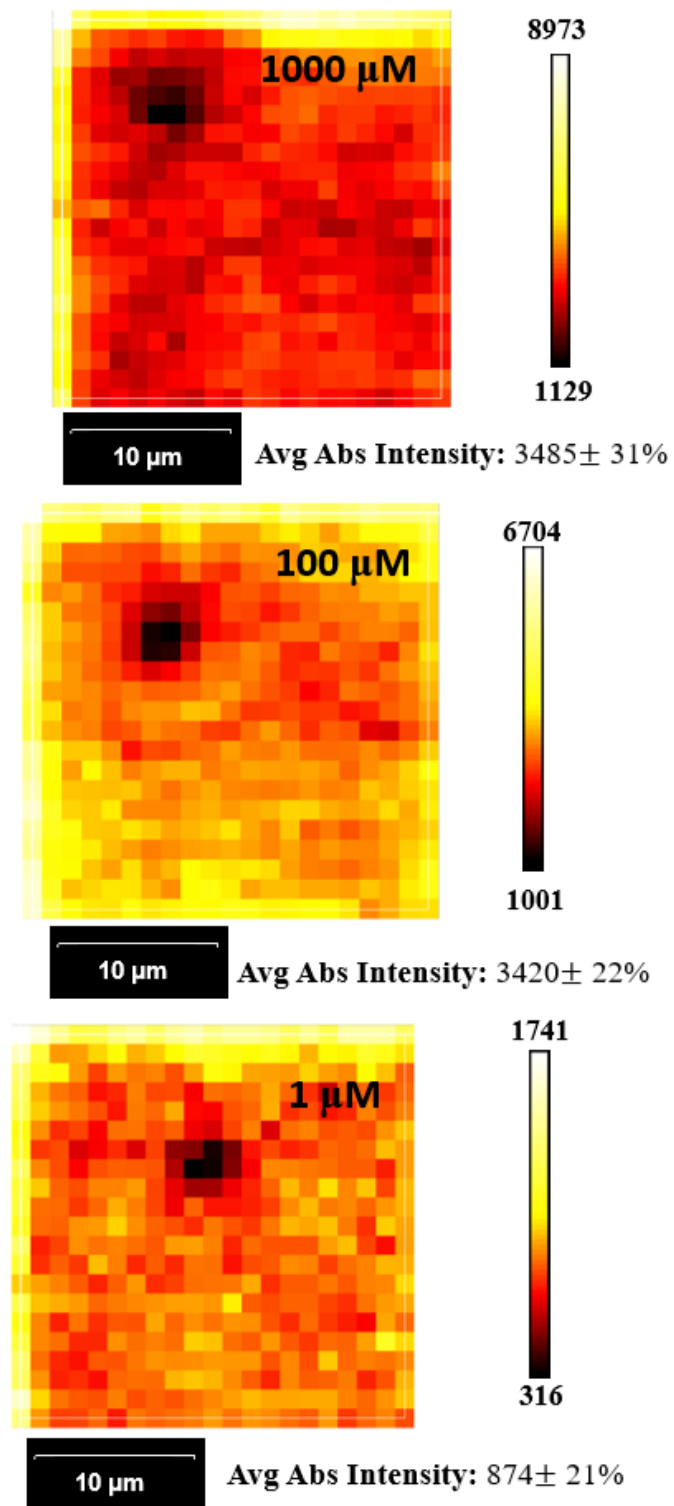


**Figure 4.5.** 21 x 21 μm square area SERS mapping of R6G coated on Au@s-SiO<sub>2</sub> film SERS substrates, at the associated concentration. Analysis was completed to the absolute intensity of the 613 cm<sup>-1</sup> R6G band. 441 spectra were obtained with 1 μm steps, 1 accumulation, and 10 second exposure time

Each image shown in Figure 4.5 displays small regions of weak SERS activity (black squares). Majority of the analyzed area show high SERS intensity signals as a result of efficiently formed SERS hot-spots. The figure also shows that as the concentration of analyte increases (1-1000  $\mu\text{M}$ ), the spatial variability was greatly reduced.

Mapping with a larger step was also performed in an attempt to cover larger areas. In Figure 4.6, SERS mapped images of Au@t-SiO<sub>2</sub> are displayed with 5  $\mu\text{m}$  steps rather than 1  $\mu\text{m}$  steps to increase the distance between each spectrum and avoid overlapping in laser interaction limiting the exposure of adsorbed R6G to the laser beam during analysis at each spot. At 1  $\mu\text{M}$  R6G, the % RSD for Au@t-SiO<sub>2</sub> is less than that of the Au@s-SiO<sub>2</sub> film. This type of mapping better emphasizes the variation in hot spot formation on the Au@t-SiO<sub>2</sub> film, further proving Au@s-SiO<sub>2</sub> to be the better substrate.

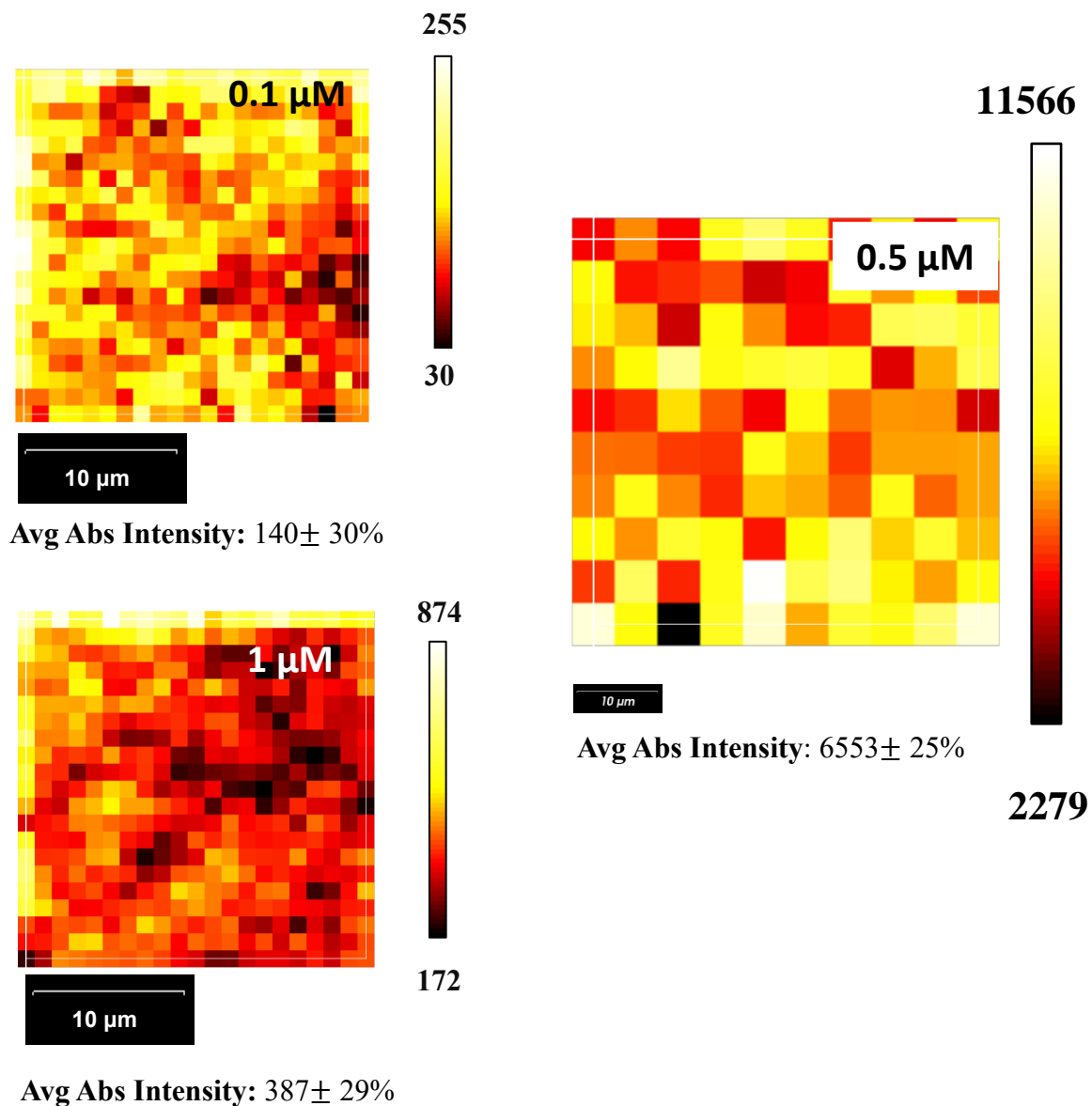


**Figure 4.6.** SERS mapping of R6G coated on Au@t-SiO<sub>2</sub> film SERS substrates: (left) 0.1 and 1  $\mu\text{M}$  on a 21 x 21  $\mu\text{m}^2$  area (1  $\mu\text{m}$  steps, 1 accumulation) and (right) 0.5  $\mu\text{M}$  on a 50 x 50  $\mu\text{m}^2$  area (5  $\mu\text{m}$  steps, 4 accumulations) 1 second exposure time. Analysis was completed to the absolute intensity of the 613  $\text{cm}^{-1}$  R6G band.

#### 4.4. SERS Substrates Evaluation: Signal Repeatability Between Substrates

Analytical repeatability is an important figure of merit in analytical chemistry. Along with the good point-to-point reproducibility, slides must show a good reproducibility between slides, since differences in SERS-EF between substrates can result in errors when quantifying species in solution. The sample-to-sample variability of the Au@s-SiO<sub>2</sub> and the Au@t-SiO<sub>2</sub> slides in this study is well illustrated with the waterfall SERS spectra from 8 sample films (Figure 4.7).

Unfortunately, the substrate-to-substrate reproducibility expressed in terms of the % RSD of determination on six independent slides (data points in Tables 4.1 and 4.2) are 34 and 26% for Au@s-SiO<sub>2</sub> and Au@t-SiO<sub>2</sub>, significantly higher than the values obtained for the point-to-point reproducibility, 8 and 18%, respectively. Because of time constraints, the following studies were aimed to establish the substrates performance by establishing other figures of merit such as sensibility, limit of detection, and limit of quantification, instead of trying to optimize the substrate-to-substrate reproducibility. The statistical data shown so far was performed with 6 random spatial SERS responses measured manually. As it was mentioned, SERS mapping was accomplished to obtain numerous spectra (441) for each acquisition on a single slide. These data were used to perform one-way ANOVA tests [96] to evaluate the statistical difference between both type of substrates (Au@s-SiO<sub>2</sub> and Au@t-SiO<sub>2</sub>). However, the SERS data failed the Shapiro-Wilk normality test ( $P < 0.050$ ) in both film types; showing that the data sets were not normally distributed. For this reason, the nonparametric Kruskal-Wallis One-Way ANOVA test was adopted for the analysis. Detailed descriptions of these statistical tests are found in the bibliography [96, 97].

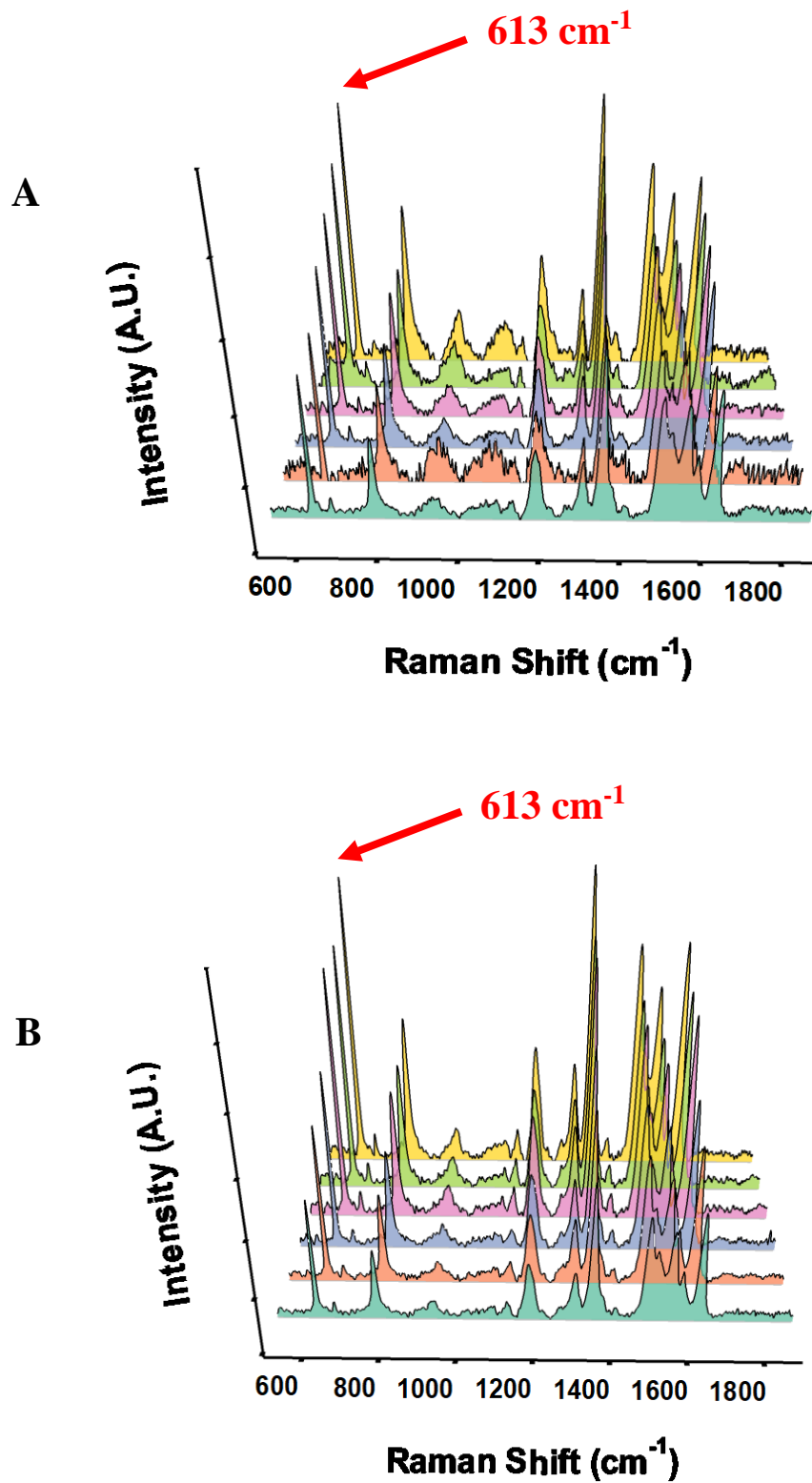


**Figure 4.7.** Waterfall SERS spectra of 1  $\mu\text{M}$  R6G from 6 sample films of Au@t-SiO<sub>2</sub> (A), and Au@s-SiO<sub>2</sub> (B). Each spectrum is an average of 8 measurements taken on each film. Spectra obtained with following Raman parameters: 50 mW of 532 nm excitation at 0.5% nominal power and 10 second integration time for 10 accumulations 50x magnification.

The test found that the differences in the median values of the absolute SERS intensity among four different samples of Au@s-SiO<sub>2</sub> are greater than would be expected by chance, thus there is a statistically significant difference amongst the samples (H = 804.163, P = <0.001). For the Au@t-SiO<sub>2</sub> substrate, the test also revealed that there is a statistically significant difference among the Au@t-SiO<sub>2</sub> samples (H = 761.782, P = <0.001). The results allow to conclude that there is a strong difference between the signals obtained on different samples of the same film type and establish the lack of signal reproducibility between samples.

#### **4.5. Sensitivity, Limit of Detection and Limit of Quantification Determination for Au@s-SiO<sub>2</sub> and Au@t-SiO<sub>2</sub>**

The SERS spectra for both the Au@t-SiO<sub>2</sub> and Au@s-SiO<sub>2</sub> system are shown in comparison to the background signal of the Au@SiO<sub>2</sub> substrate measured in substrates immersed in water instead of R6G solutions (blank) in Figure 4.8. The blank has a consistent signal peak that occurs around 1500-1700 cm<sup>-1</sup>. This peak overlaps with several vibrational bands of R6G (Table 1.1), but the SERS signals are so strong even for a low concentrations R6G solution (0.1 μM) that the vibrational bands for R6G are clearly visible in both substrates Au@s-SiO<sub>2</sub> and Au@t-SiO<sub>2</sub>.

For the sensitivity, limit of detection and limit of quantification determination for Au@s-SiO<sub>2</sub> and Au@t-SiO<sub>2</sub>, SERS spectra for R6G solutions between 0.05 μM and 1000 μM were collected for both type of substrates on 5 positions in each substrate. These spectra were collected under the following conditions: 0.5% power of a 532 nm 50 mW excitation laser, 10 second integration time, 10 accumulations, and 50x magnification. Spectra at 5

points were collected and averaged for each solution. Figures 4.9A and 4.10A show the spectra collected at five different points for Au@s-SiO<sub>2</sub> and Au@t-SiO<sub>2</sub> at each concentration.

It is worth noting that although the Au SERS-active nanoparticles deposited on silica glass (Appendix A1) and on the synthesized SiO<sub>2</sub> particle film are the same, the sensitivity of the latter is significantly higher. This is attributed to the difference in morphology between the two systems, where the roughened structure that is introduced to the Au@SiO<sub>2</sub> films is beneficial.

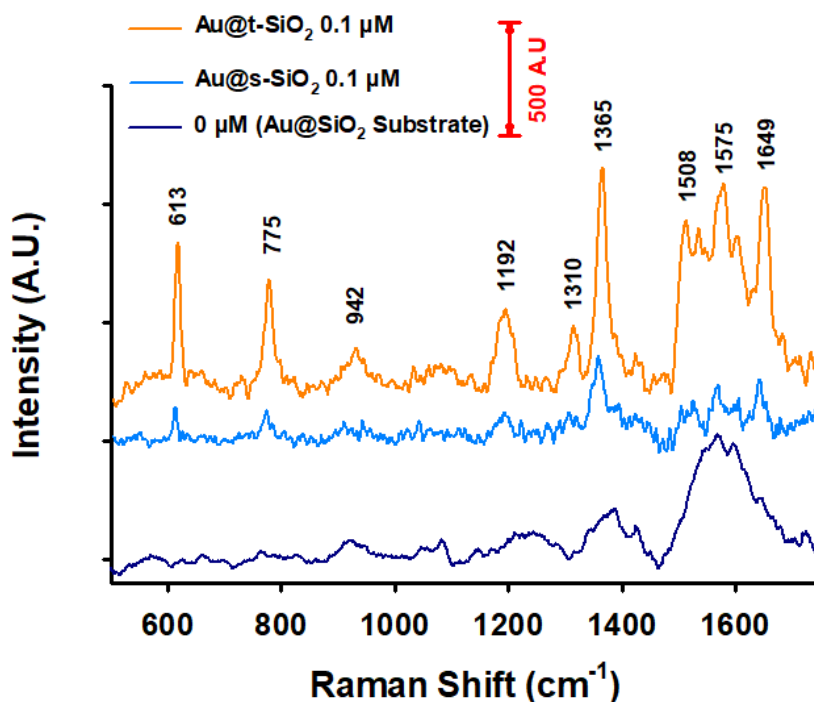


**Figure 4.8.** Comparison of SERS spectra collected with the Au@t-SiO<sub>2</sub> (orange) and Au@s-SiO<sub>2</sub> (blue) systems at 0.1 μM. Black line corresponds to the Au@SiO<sub>2</sub> film. The SERS intensity scale bar is 500 A.U. Laser λ: 532 nm; laser power: 25 mW



The calibration curves  $\log$  [SERS signal] vs  $\log$  [concentration] are shown in Figure 4.9 and 4.10, along with the best linear regression fit to the experimental data (Eq. 4-1).

$$\log(\text{SERS signal}) = \log(b) + m * \log([R6G]) \quad (4-1)$$

In this case, both the peak height and the signal integrated area after baseline correction were used for the calibration curves. The intensities used to create the linear regression curves correspond to average values of spectra collected at five positions. As shown, the calibration curves in the figures follow the expected linear trend as the intensity increases with the concentration. Regression parameters and correlation coefficient ( $R^2$ ) are summarized in Table 4.3. The point for 0.1  $\mu\text{M}$  was excluded from the calibration curve since it seems to be outside the linear range for this substrate. SERS observations frequently result in nonlinear intensity variations with concentration at very low or very high monolayer coverage [98].

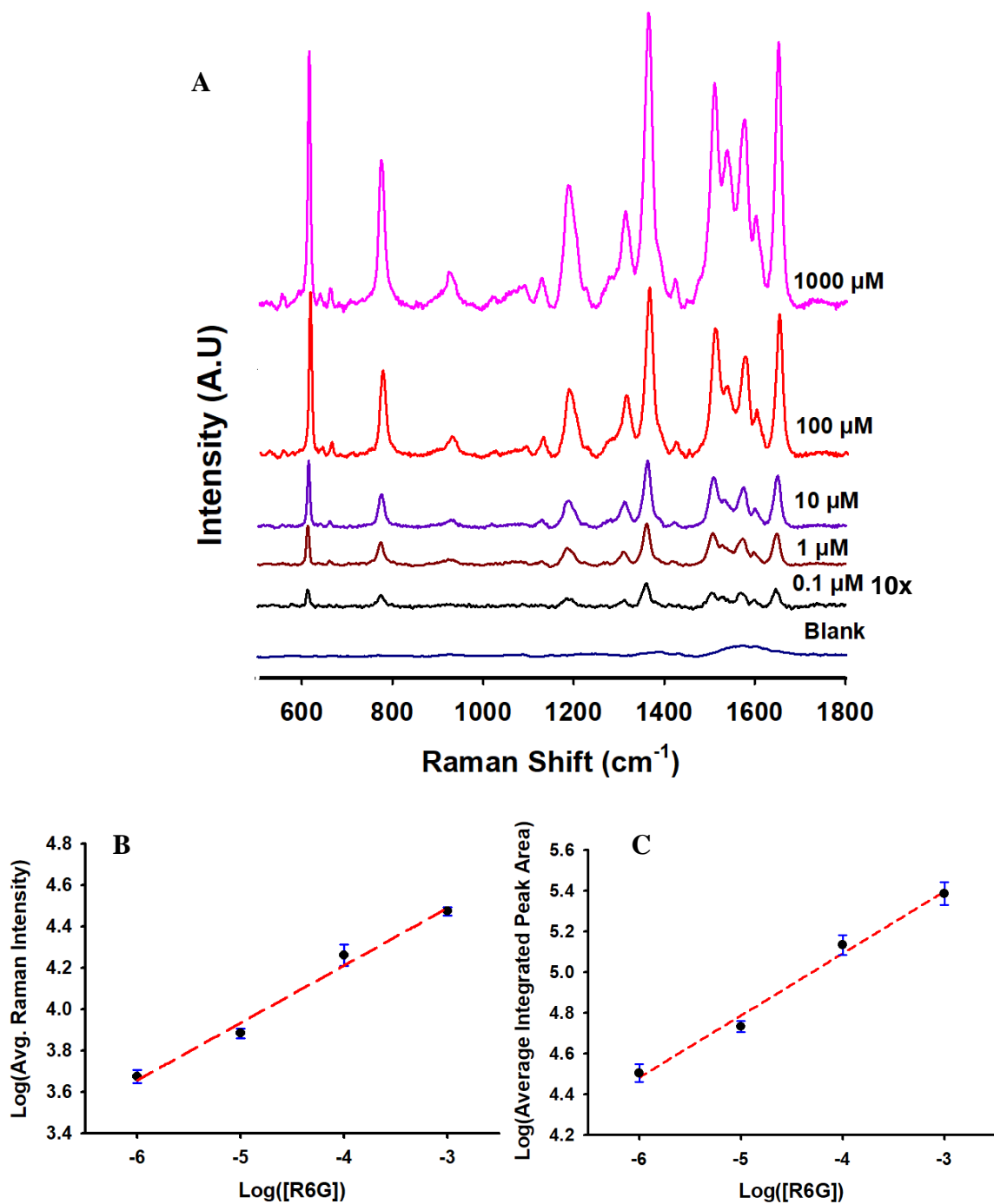


**Figure 4.9.** (A) SERS spectra of R6G measured at increasing concentrations (0.1  $\mu\text{M}$  to 1000  $\mu\text{M}$ ) on Au@s-SiO<sub>2</sub> films. Calibration curve for R6G analyzed on Au@s-SiO<sub>2</sub> films at a concentration range of 1000  $\mu\text{M}$  to 1  $\mu\text{M}$  obtained using (B) Peak height at 613  $\text{cm}^{-1}$  and the respective (C) peak integration area

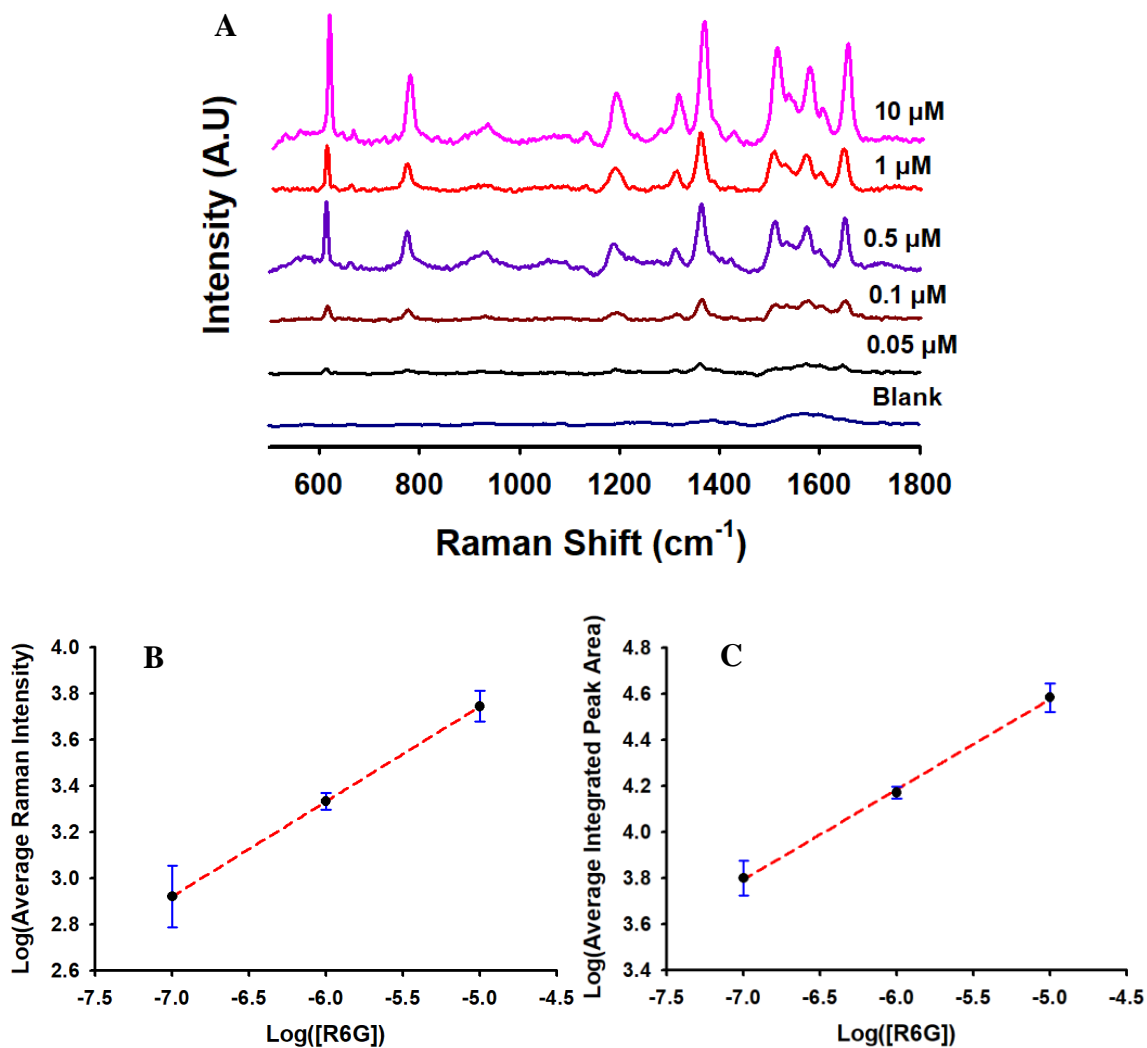


**Figure 4.10.** (A) SERS spectra of R6G measured at increasing concentrations (0.05  $\mu\text{M}$  to 10  $\mu\text{M}$ ) on Au@t-SiO<sub>2</sub> films. Calibration curve for R6G analyzed on Au@t-SiO<sub>2</sub> films at a concentration range of 0.1  $\mu\text{M}$  to 10  $\mu\text{M}$  obtained using (B) Peak height at 613  $\text{cm}^{-1}$  and the respective (C) peak integration area

**Table 4.3.** Regression analysis summary for calibration curves collected on both t-SiO<sub>2</sub> and s-SiO<sub>2</sub> systems.

	Au@t-SiO <sub>2</sub>			Au@s-SiO <sub>2</sub>		
	Slope	R <sup>2</sup>	y-intercept log(b)	Slope	R <sup>2</sup>	y-intercept log(b)
Integrated Peak area	0.3924	0.9991	6.540	0.3050	0.989	6.312
Peak Height	0.4116	1	5.803	0.2778	0.986	5.323

The SERS-EF is used extensively in the literature to report the performance of new substrates [60, 99-102]; however, there is some controversy regarding its validity as an ideal metric for comparison between substrates prepared using different methods [22, 62, 103]. For this reason, in this thesis, the sensitivity, limit of detection (LoD) and limit of quantification (LoQ) will be used as figures of merit. Figures 4.9 and 4.10 display the calibration curves used to calculate these three parameters for both substrates.

In accordance to IUPAC guidelines, the minimal acceptable signal intensity to assess whether R6G is in solution (LoD) must be three times greater than the standard deviation of the blank signal:

$$S_m = \bar{S}_{bl} + 3 * s_{bl} \quad (4-2)$$

$$\text{LoD} = 10^{\left(\frac{\log(S_m) - \log(b)}{m}\right)} \quad (4-3)$$

where,  $\bar{S}_{bl}$ , is the average signal in the blank, and  $s_{bl}$  is the standard deviation in the signal of several blank measurements. On the other hand, the LoQ is the minimum concentration at which quantitative measurements can be made. This is described as ten times the standard deviation in the blank signal:

$$\text{LoQ} = 10^{\left(\frac{\log(\bar{S}_{bl} + 10 * s_{bl}) - \log(b)}{m}\right)} \quad (4-4)$$

The LoD and LoQ values for the respective substrate (Au@s-SiO<sub>2</sub> and Au@t-SiO<sub>2</sub>) can be found in Table 4.4. The timeframe of the thesis did not allow for the preparation of additional slides to carry out measurements in more dilute regions and use the most conventional linear signal vs. concentration plots for the determination of the LoD and LoQ. Instead, these figures of merit were obtained from log-log regression plots using the peak height of the analyte and blank signals at ~613 cm<sup>-1</sup> for the analysis. It is highly likely that the Au@s-SiO<sub>2</sub> film can detect R6G at concentrations lower than 0.1 μM as implied by the LoD in Table 4.4; however, this was not confirmed experimentally due to time restriction.

**Table 4.4.** Summarized figure of merits acquired by quantitative analysis of the peak height of the 613 cm<sup>-1</sup> band

Substrate	LoD (M)	LoQ (M)	Sensitivity
Au@s-SiO <sub>2</sub>	3.00x10 <sup>-10</sup>	1.62x10 <sup>-8</sup>	0.278
Au@t-SiO <sub>2</sub>	2.58x10 <sup>-8</sup>	3.81x10 <sup>-7</sup>	0.412

Any attempts to estimate the SERS-EF using different type of approximations to calculate the number of Au Nps in the films, and adsorbed R6G molecules on the Au surface resulted in unrealistic and highly unexpected values, probably due to the assumptions required when calculating the SERS-EF. For this reason, only the LoD and LoQ are reported in Table 4.4.

The calibration curve for the Au@s-SiO<sub>2</sub> films led to an LoD calculation two orders of magnitude lower than the one obtained for the Au@t-SiO<sub>2</sub> film and an LoQ one order of magnitude lower. Although the Au@t-SiO<sub>2</sub> calibration curve exhibits a steeper slope, it is not clear why the individual signals are less intense in these samples.

However, these results must be taken with care because of the low number of samples analyzed, and the relative standard deviations of the point-to-point and sample-to-sample determination in the case of the textured sample.

In Table 4.4, the LoD and LoQ were determined with average and standard deviation values that were calculated using the 5 points measured at the 5 sites on the blank substrate, as is (including any negative values). The signal-to-noise ratio found in the spectra for each point of measurement was very random, and the baseline for each measurement was different which makes it difficult to acquire an accurate standard deviation for signal in the  $613\text{ cm}^{-1}$  range. In this second method, the standard deviation used in calculation is considered as the standard deviation as the analyte concentration approaches 0 M,  $SD_0$ . Thus, the signal for the LoD is defined as  $3*SD_0$  and that for LoQ as  $10*SD_0$ . Four concentrations in the most dilute region are plotted on the x-axis, with the corresponding standard deviation on the y-axis. The extrapolation of this plot gives,  $SD_0$ , the standard deviation as the concentration approaches 0 M. Using the regression line equation, 0 M was substituted as the concentration and the y-intercept will remain; this is the  $SD_0$ . For *s*-SiO<sub>2</sub>, the y-intercept came to be 188.108 using the following 4 most dilute concentrations: 0.1  $\mu\text{M}$ , 1  $\mu\text{M}$ , 10  $\mu\text{M}$ , and 100  $\mu\text{M}$ . The y-intercept for the *t*-SiO<sub>2</sub> was found to be 183.417 and this was obtained with the following three concentrations: 0.1  $\mu\text{M}$ , 1  $\mu\text{M}$ , and 10  $\mu\text{M}$ . The final LoD and LoQ values are summarized in Table 4.5.

**Table 4.5.** Determination of LoD, LoQ with extrapolated standard deviation values

Substrate	LoD	LoQ
Au@s-SiO <sub>2</sub>	5.469x10 <sup>-10</sup> M	4.170x10 <sup>-8</sup> M
Au@t-SiO <sub>2</sub>	3.638x10 <sup>-8</sup> M	6.780x10 <sup>-7</sup> M

Table 4.6 summarizes the reported LoD concentrations visually evaluated for R6G detected on a variation of Au substrates from the literature. This was done to determine how R6G compares to published substrates, and it can be concluded that the LoD of both Au@SiO<sub>2</sub> systems are comparable with literature values. The parameters, such as laser wavelength is different for some of these substrates, thus it is not expected to be a good comparison. However, we can evaluate the benefit of using the 532 nm laser in some cases.

**Table 4.6.** Visual limit of detection concentrations determined in literature on Au-based substrate films.

Year	Substrate	Laser $\lambda$	LoD (M)	Ref.
2012	Au Nps array	785 nm	1.00x10 <sup>-10</sup>	[69]
2019	Amino functionalized SiO <sub>2</sub> core@a-Si shell particle array Au Nps	633 nm	1.00x10 <sup>-10</sup>	[104]
2013	Au Nano worms of individual Au Nanospheres	1064 nm	1.00x10 <sup>-7</sup>	[100]
2019	Silica coated Au nanostars	632.8 nm	0.58x10 <sup>-7</sup>	[105]
/	Au@s-SiO <sub>2</sub> film	532 nm	3.00x10 <sup>-10</sup> (10 <sup>-7</sup> )	This Work
/	Au@t-SiO <sub>2</sub> film	532 nm	2.58x10 <sup>-8</sup> (5 x 10 <sup>-8</sup> )	This Work

The sensitivity determination was done by using the curves shown in Figures 4.9 and 4.10; whether the peak height or the peak integrated area were used for the determination, the calculated values for the Au@t-SiO<sub>2</sub> films is higher than that of the Au@s-SiO<sub>2</sub> films. Considering that these calculations can be influenced by the number of points involved, two additional R6G solutions (0.5, and 0.05 μM) were prepared and measured on Au@t-SiO<sub>2</sub> films the following day. The agreement with previous data was not good (Figure 4.10B and C) and therefore could not be included in the final calculations. Despite the lower sensitivity, the Au@s-SiO<sub>2</sub> films have consistently shown higher signals than the Au@t-SiO<sub>2</sub> films. This is something that could not be analyzed at this point, but it is likely associated to the properties of the SiO<sub>2</sub> films where the Au Nps are adsorbed and will be addressed in the future.

### *Surface Property Studies*

As described in Chapter 2, the SiO<sub>2</sub> screen-printed templates of interest were prepared with particles either inhabiting a solid or texturized surface. Each type of material results in very different pastes and films as confirmed by using optical profilometry. Au Nps adsorbed on these films have shown to result in difference in SERS intensity towards R6G. The best performance in terms of the intensity of the signals for the 613 and 1649 cm<sup>-1</sup> bands has been found for the Au@s-SiO<sub>2</sub> substrates (see Figure 4.11). The weaker SERS response for the t-SiO<sub>2</sub> substrate might be associated to the extreme aggregation observed in the case of the SiO<sub>2</sub> starting materials (Figure 3.4). However, this substrate has shown to have a greater sensitivity, indicating that other factors might play a role in the overall substrate performance.



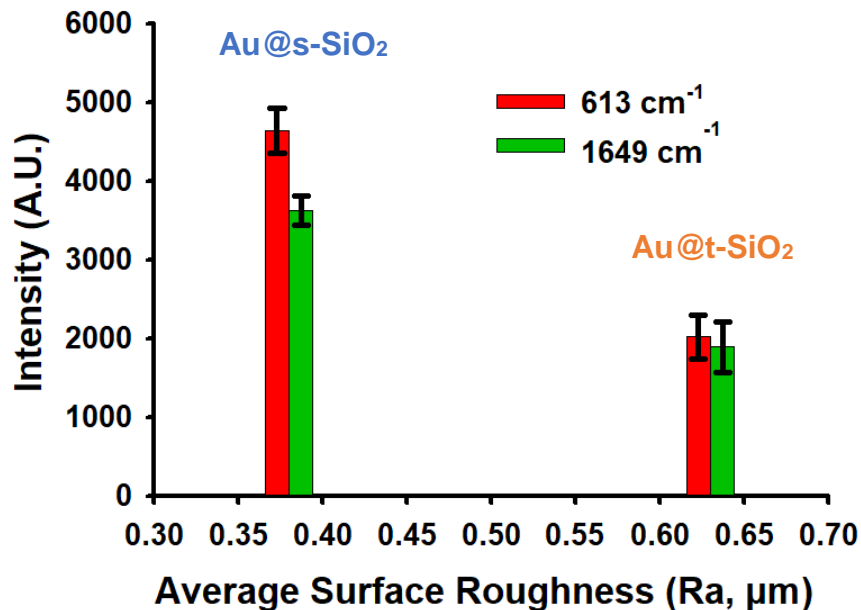


**Figure 4.11.** Average roughness as a function of SERS intensity of band at 1649 and 613  $\text{cm}^{-1}$  on Au@t-SiO<sub>2</sub> and Au@s-SiO<sub>2</sub>

SERS research has demonstrated that the pore size of a porous substrate can influence the electromagnetic LSPR enhancement of metal Nps [9, 23, 34]. Efficient LSPR occurrences take place within an ideal distance between plasmonic Nps; when the pore size is too large or too small, the enhancement can be diminished because the pore size of the template will dictate the distance between the Au Nps, and the proximity of the analyte to Au Nps [9, 15, 27]. Interparticle distances below 1 nm experience considerable broadening due to nonlocal effects [5]. The structure of the t-SiO<sub>2</sub> aggregate particles may be restricting the amount of Au Nps that can embed on the t-SiO<sub>2</sub> aggregate; as well as affect the distance between each Au Np, making the expected hot-spot region susceptible to weaker electric field enhancements.

In order to demonstrate that the observed response intensities from the two substrates behave differently, the Mann-Whitney rank sum test [96] was carried out using

the 441 spectra for 1  $\mu\text{M}$  R6G obtained using SERS mapping on Au@s-SiO<sub>2</sub> and Au@t-SiO<sub>2</sub> films. The median of the 441 absolute SERS intensity values collected at 1  $\mu\text{M}$  R6G on a singular Au@s-SiO<sub>2</sub> compared to the median of the 441 absolute SERS intensity values collected on a singular Au@t-SiO<sub>2</sub> differed significantly (Mann Whitney U = 4696.500,  $n_1 = n_2 = 441$ ,  $P = <0.001$ ). Therefore, Au@s-SiO<sub>2</sub> demonstrated significantly higher SERS intensity values at the 613  $\text{cm}^{-1}$  band than Au@t-SiO<sub>2</sub>.

### *Conclusions for this chapter*

The fabricated 3D substrates, Au@s-SiO<sub>2</sub> and Au@t-SiO<sub>2</sub> were evaluated for their SERS signal spatial variability and sample-to-sample variability. The coefficient variation values calculated for the Au@s-SiO<sub>2</sub> substrate film were relatively low, indicating uniformity within the individual films. Au@t-SiO<sub>2</sub> films exhibit less uniformity as the coefficient variation values were generally higher than Au@s-SiO<sub>2</sub>. However, in examining sample-to-sample variability, Au@t-SiO<sub>2</sub> showed slightly better signal reproducibility. Comparing the LOD of both Au@SiO<sub>2</sub> substrates (Table 4.7), the more uniform porous template structure that is introduced by the Au@s-SiO<sub>2</sub> substrates enhances the surface plasmon excitation experienced during SERS analysis resulting in improved detection sensitivity. With that being said, the reason for this is not clearly understood, since the signals for the Au@t-SiO<sub>2</sub> substrates were always lower than those for the Au@s-SiO<sub>2</sub> substrate at the same R6G solution concentrations. Theoretical simulations are required to explain this apparent discrepancy.

**Table 4.7.** Reproducibility, Sensitivity, LoD, and LoQ for Au@s-SiO<sub>2</sub> and Au@t-SiO<sub>2</sub>

<b>Substrate</b>	<b>Sample to Sample % RSD</b>	<b>Spatial % RSD</b>	<b>Sensitivity</b>	<b>LoD (Visual) (M)</b>	<b>LoQ (M)</b>
<b>Au@s-SiO<sub>2</sub></b>	34	8	0.2778	6 x 10 <sup>-10</sup> (10 <sup>-7</sup> )	4 x 10 <sup>-8</sup>
<b>Au@t-SiO<sub>2</sub></b>	26	18	0.4116	4 x 10 <sup>-8</sup> (5 x 10 <sup>-8</sup> )	7 x 10 <sup>-7</sup>

## Chapter 5: Conclusions and Future Work

In this study, the aim was to develop and optimize a cost-effective, facile, screen-printing method for the preparation of sensitive and reproducible SERS substrates. In this approach, Au colloidal particles were adsorbed (embedded) on SiO<sub>2</sub> 3D nanostructured films prepared using pastes containing SiO<sub>2</sub> particles synthesized by the Stöber method in the absence and presence of a surfactant (CTAB). For the preparation of the pastes, several formulations were analyzed, but one involving ~18 wt% silica, 9 wt% ethyl cellulose, 64 wt%  $\alpha$ -terpineol, and 9 wt% ethanol was finally used because of the good adherence to the silica substrate after calcination at 600 °C, resulting in macroscopic uniform silica films. Preliminary attempts to upload Au Nps on the pristine SiO<sub>2</sub> particles films were unsuccessful, and for this reason, PEI was used to functionalize the surface of silica, and make the interaction with the Au-citrate capped Nps more favourable.

Both, materials and films were extensively characterized with the goal of getting a better understanding of the impact of the materials properties on the film morphology and SERS signals. In the case of the SERS signal spatial reproducibility, the values obtained for both substrates fall within the literature acceptable % RSD range of <20%. The LoD ( $3.00 \times 10^{-10}$  M for Au@s-SiO<sub>2</sub> and  $2.58 \times 10^{-8}$  M for Au@t-SiO<sub>2</sub>) and LoQ ( $1.62 \times 10^{-8}$  M for Au@s-SiO<sub>2</sub> and  $3.81 \times 10^{-7}$  M for Au@t-SiO<sub>2</sub>) values are close to those reported in the bibliography for R6G; however, lower limits have been reported for other target analytes, highlighting the need to study the performance of these new substrates with other molecules.

### ***Comparison with layer-by-layer deposition prepared substrates (Appendix A1)***

A comparison with the first intended substrate from the initial stage of the thesis project (Appendix A1) takes us to conclude that our developed screen-printed method has a number of advantages in terms of sensitivity and slide-to-slide reproducibility, as discussed below.

R6G concentrations at or above 0.1 mM readily saturate the detector when deposited on the Au@t-SiO<sub>2</sub> film, so it can not be compared to the Au monolayer and multilayer films prepared by the layer-by-layer approach (Appendix A1) which could not detect concentrations below 0.1 mM.

A multilayer Au film on silica glass slides was implemented as a way to increase the amount of Au Nps on the surface of glass. Unfortunately, this method requires multiple layer-by-layer depositions to reach an ideal structural morphology that will generate an enhanced SERS signal. The substrate examined is a product of three depositions which is insufficient for the purpose. The Au@SiO<sub>2</sub> films exhibited stronger peak intensity than both the Au monolayer and multilayer on silica glass, also lower LoD levels for Au@SiO<sub>2</sub> were detected. This confirms that the Au@SiO<sub>2</sub> substrate developed in this work demonstrated that the enhanced signal can be obtained in an alternative way that is less tedious and more time-effective.

### ***Au@s-SiO<sub>2</sub>***

The adsorption of Au Nps on the s-SiO<sub>2</sub> films resulted in more uniform SERS substrates and moderate roughness, resulting in better point-to-point reproducibility with an average % RSD of ~ 8%, and a sample-to-sample reproducibility of 34% for Au@s-

SiO<sub>2</sub>; however, the conditions explored in the thesis were very limited, and there is significant room for improvement. Top and lateral SEM images of the s-SiO<sub>2</sub> films confirmed the formation of highly dense and uniform distribution of discrete spherical SiO<sub>2</sub> particles. The uniform distribution of Au nanoparticles on the surface of the SiO<sub>2</sub> particle film (EDX) is consistent with the profilometer and the SERS mapping results. To illustrate this, a SEM image, the surface topography and a typical SERS map results for a representative substrate are reproduced here in Figure 5.1.

### ***Au@t-SiO<sub>2</sub>***

The large particle aggregates present in the synthesized t-SiO<sub>2</sub> nanomaterials led to films with a random distribution of large crevices on the SiO<sub>2</sub> film surface that can explain the lower point-to-point reproducibility when compared to the Au@s-SiO<sub>2</sub> substrates (average % RSD of ~ 18%), curiously the sample to sample reproducibility was slightly better 26% and as well as the sensitivity (slope) towards R6G. Profilometer and SEM images for these films are illustrated in Figure 5.2.

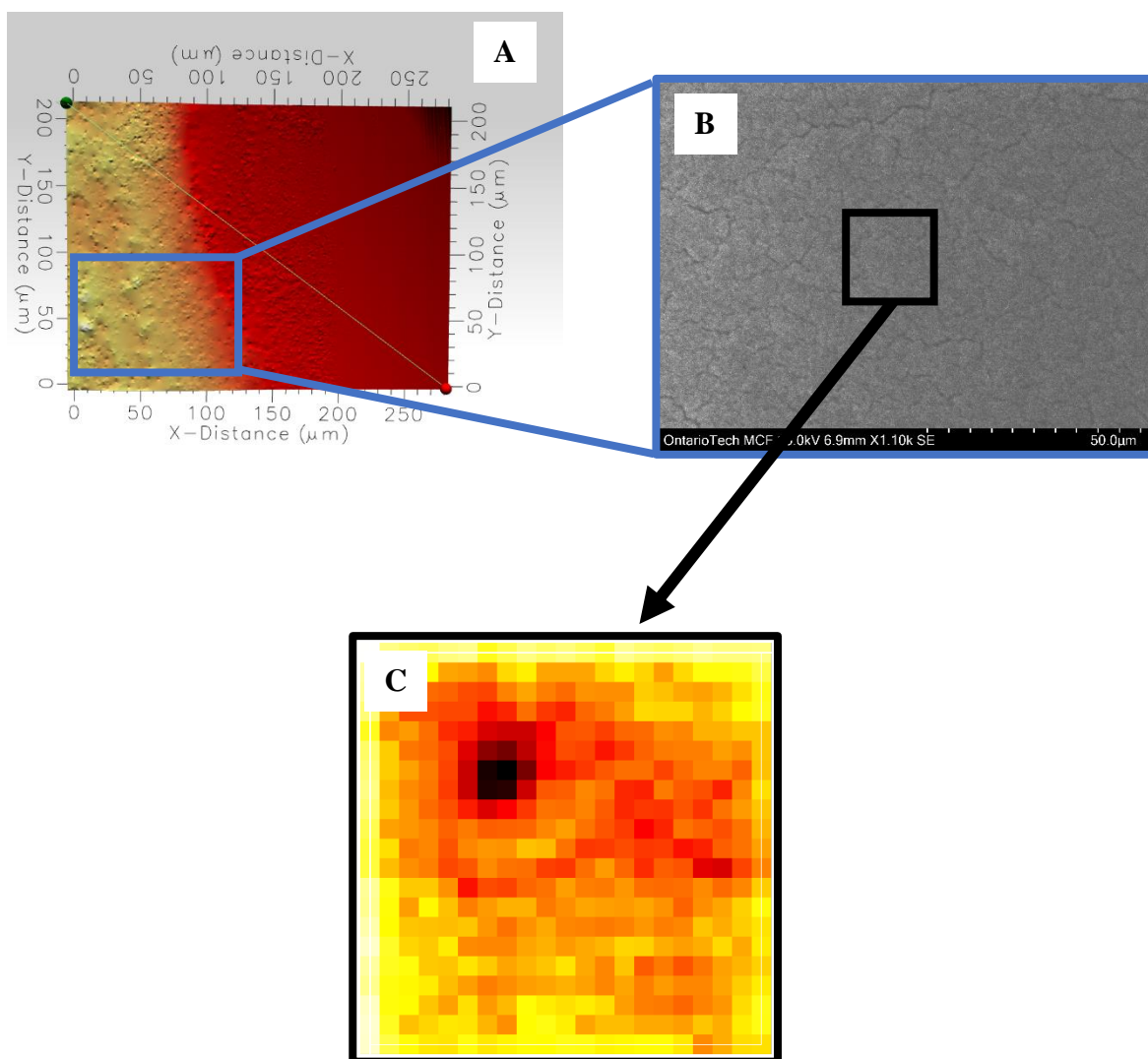


**Figure 5.1.** (A) Typical 3D scanned surface topography of a Au@s-SiO<sub>2</sub> film (250 x 200 μm square area compared to (B) a characteristic SEM image of a Au@s-SiO<sub>2</sub> film (25 x 17 μm square area), and resulting (C) SERS map of a smaller area (21 x 21 μm square area) indicated by the black square.

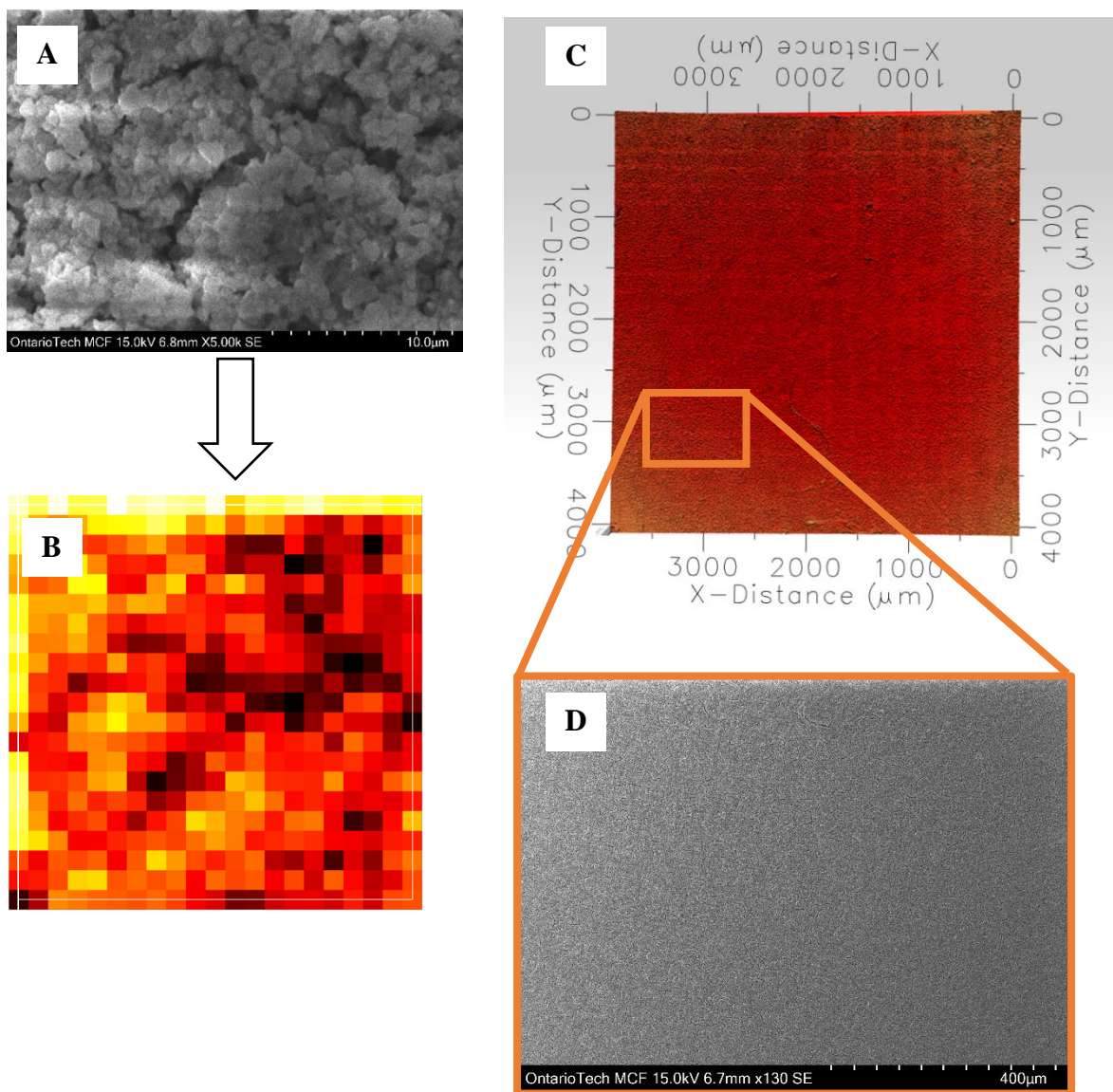


**Figure 5.2.** Au@t-SiO<sub>2</sub> film displayed as (A) a SEM image (25 x 17 μm square area), and (B) a typical SERS map of a similar area (21 x 21 μm square area) from this substrate. (C) A 3D scanned surface topography image of Au@t-SiO<sub>2</sub> (4000 x 4000 μm), and size comparison (orange box within) to the a (D) SEM image obtained at a larger scale (965 x 680 μm).



## Future Work

### 1. Optimize procedure to reduce differences between sample films

In this study, the fabricated films showed to inhabit a high number of “cracks” on the surface as displayed in the SEM images of the film following calcination (Figure 3.11 and 3.12). The large fractures are still present after Au adsorption as shown in Figure 5.3.

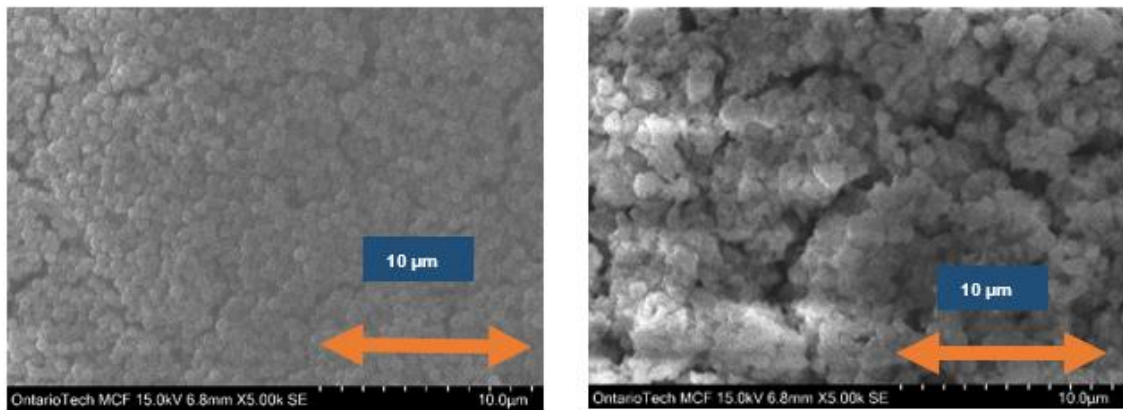


**Figure 5.3.** SEM images of (Left) Au@s-SiO<sub>2</sub> and (Right) Au@t-SiO<sub>2</sub>; Scale bar: 10 µm.

The presence of cracks is far from ideal as it will change the Au Nps environment and consequently the SERS signal. Microscale structural differences in the substrate will alter the potential electromagnetic enhancement along the surface eventually generating spatial and sample-to-sample variability.

Future work will involve studying smaller silica nanoparticle, paste formulations and heat treatments to avoid the formation of cracks.

***Changes in paste formulation:*** For instance, it has been proposed that the surface modification of the silica particles using a silane-coupling agent can contribute to produce more uniform films, despite this was considered an option in the original plan, the preparation of the SERS substrate resulted highly time consuming and it could not be intended. The silane molecules can adsorb onto the hydrophilic surface of the SiO<sub>2</sub> particles yielding a hydrophobic tail into the paste medium; this is expected to enhance the compatibility of the SiO<sub>2</sub> particles with the organic vehicle. The silane also acts as a dispersant, leading to better dispersion of the SiO<sub>2</sub> particles in the colloidal suspension. Consequently, the paste will experience less friction and lowered viscosity at low shear rates thus, the rheological behaviour must be studied again to ensure that the paste is suitable for screen-printing applications.

***Effect of SiO<sub>2</sub> particle size:*** Studying the impact of the SiO<sub>2</sub> particle size is an excellent approach towards optimizing the proposed sensor for better reproducibility and SERS enhancing ability potentially contributing to reducing the LoD value by the formation of more hot spots when loading with Au Nps. This work was a development project thus this could not be done within the limited time due to certain restrictions. The SiO<sub>2</sub> particle size was obtained using 0.57 M of basic catalyst in order to produce a high yield of SiO<sub>2</sub> product to isolate within 24 hours and following centrifugation. Smaller particles are synthesized with a lower concentration of NH<sub>4</sub>OH, however based on previous experiments, it was difficult to recover product after an ageing time of 24 hours. As a consequence, it could not have been studied within the duration of this thesis.

***Investigate the effect of Au Nps size, shape, and Raman excitation laser:*** Generally, the shape of the Au Np will exhibit different optical properties that will impact on the absorbance of the generated localized surface plasmon resonance. Thus, the sensitivity of the substrate can be tailored to enhance the Au Np resonance with any Raman excitation laser, taking advantage of the SERS enhancement made possible by SERRS. The size of the Au Nps in this study was 3-5 nm to obtain a matched LSPR of the Au nanomaterial to the excitation laser of 532 nm, however this was a compromise because a small Au Np size exhibits limited oscillation conduction band electrons. For this reason, larger Au Nps (~20-50 nm) which exhibit stronger local field effects will be intended in the future.

## **2. Use these SERS sensors to investigate other analytes**

The analyte, R6G, was used throughout this thesis work, however fluorescent dyes have recently been discouraged for use as model molecules, due to its fluctuation cross-section upon adsorption to metal, and the high fluorescence background which deters the accurate calculation of SERS-EF. Analytes, such as melamine, can be considered due to its typically distinctive signals, and the thiol, 4-mercaptobenzoic acid, due to its strong binding affinity to Au Nps.

## Chapter 6: References

1. Smith, E. and G. Dent, *The Theory of Raman Spectroscopy*, in *Modern Raman Spectroscopy – A Practical Approach*. 2004. p. 71-92.
2. Agarwal, N.R., et al., *Ag and Au nanoparticles for SERS substrates produced by pulsed laser ablation*. Cryst. Res. Technol., 2011. **46**(8): p. 836-840.
3. Moskovits, M., *Surface-enhanced Raman spectroscopy: a brief retrospective*. J. Raman Spectrosc., 2005. **36**(6-7): p. 485-496.
4. Moskovits, M., *Surface-enhanced spectroscopy*. Rev. Mod. Phys., 1985. **57**(3): p. 783-826.
5. García de Abajo, F.J., *Nonlocal Effects in the Plasmons of Strongly Interacting Nanoparticles, Dimers, and Waveguides*. J. Phys. Chem. C, 2008. **112**(46): p. 17983-17987.
6. Langer, J., et al., *Present and Future of Surface-Enhanced Raman Scattering*. ACS Nano, 2020. **14**(1): p. 28-117.
7. Smith, E. and G. Dent, *Introduction, Basic Theory and Principles*, in *Modern Raman Spectroscopy – A Practical Approach*. 2004. p. 1-21.
8. Singh, D.K., M. Pradhan, and A. Materny, *Modern techniques of spectroscopy : basics, instrumentation, and applications*. Progress in optical science and photonics. 2021, Singapore: Springer.
9. Lim, H., et al., *Synthesis of Uniformly Sized Mesoporous Silver Films and Their SERS Application*. J. Phys. Chem. C, 2020. **124**: p. 23730-23737.
10. Suchomel, P., et al., *Simple size-controlled synthesis of Au nanoparticles and their size-dependent catalytic activity*. Sci. Rep., 2018. **8**(1): p. 4589-11.
11. Li, J.F., et al., *Shell-isolated nanoparticle-enhanced Raman spectroscopy*. Nature, 2010. **464**(7287): p. 392-5.
12. Fan, M. and A.G. Brolo, *Self-Assembled Au Nanoparticles as Substrates for Surface-Enhanced Vibrational Spectroscopy: Optimization and Electrochemical Stability*. ChemPhysChem, 2008. **9**: p. 1899-1907.
13. Mosier-Boss, P.A., *Review of SERS Substrates for Chemical Sensing*. Nanomaterials, 2017. **7**(6): p. 142.
14. Halvorson, R.A. and P.J. Vikesland, *Surface-Enhanced Raman Spectroscopy (SERS) for Environmental Analyses*. Environ. Sci. Technol., 2010. **44**(20): p. 7749-7755.
15. Baia, M., S. Astilean, and T. Iliescu, *Raman and SERS Investigations of Pharmaceuticals*. 1. Aufl. ed. 2008, Berlin, Heidelberg: Springer-Verlag.

16. Xu, W., et al., *DNAzyme signal amplification based on Au@Ag core-shell nanorods for highly sensitive SERS sensing miRNA-21*. *Anal. Bioanal. Chem.*, 2022. **414**(14): p. 4079-4088.
17. Hering, K., et al., *SERS: a versatile tool in chemical and biochemical diagnostics*. *Anal. Bioanal. Chem.*, 2008. **390**(1): p. 113-124.
18. Yu, B., et al., *Sensitive and simple determination of zwitterionic morphine in human urine based on liquid-liquid micro-extraction coupled with surface-enhanced Raman spectroscopy*. *Talanta (Oxford)*, 2018. **186**: p. 427-432.
19. Wu, H., et al., *Rapid and fingerprinted monitoring of pesticide methyl parathion on the surface of fruits/leaves as well as in surface water enabled by gold nanorods based casting-and-sensing SERS platform*. *Talanta (Oxford)*, 2019. **200**: p. 84-90.
20. Bell, S.E.J., et al., *Towards Reliable and Quantitative Surface-Enhanced Raman Scattering (SERS): From Key Parameters to Good Analytical Practice*. *Angew. Chem. Int. Ed. Engl.*, 2020. **59**(14): p. 5454-5462.
21. Fang, J., et al., *A SERS substrate with remarkable reproducibility: Adsorbing and detecting both hydrophobic and hydrophilic molecules using rGO/PEI/PAA/CD-AgNP nanocomposites*. *Appl. Surf. Sci.*, 2021. **542**: p. 148708.
22. Fan, M., G.F.S. Andrade, and A.G. Brolo, *A review on recent advances in the applications of surface-enhanced Raman scattering in analytical chemistry*. *Anal. Chim. Acta.*, 2020. **1097**: p. 1-29.
23. Kim, J., et al., *Single-Particle Analysis on Plasmonic Nanogap Systems for Quantitative SERS*. *J. Raman Spectrosc.*, 2021. **52**(2): p. 375-385.
24. Balasubramanian, J., et al., *Chapter 10 - Plasmonic nanosensors and their spectroscopic applications—current trends and future perspectives*, in *Molecular and Laser Spectroscopy*, V.P. Gupta, Editor. 2022, Elsevier. p. 337-372.
25. Schrader, B., *Infrared and Raman Spectroscopy - Methods and Applications*. *VCH, Weinheim, 1995, DM 298,-, ISBN 3-527-26446-9*. Vol. 100. 1996. 1268-1268.
26. Schlücker, S., *Surface-Enhanced Raman Spectroscopy: Concepts and Chemical Applications*. *Angew. Chem. Int. Ed. Engl.*, 2014. **53**(19): p. 4756-4795.
27. *Surface-Enhanced Raman Scattering and Surface-Enhanced Resonance Raman Scattering*, in *Modern Raman Spectroscopy – A Practical Approach*. 2004. p. 113-133.
28. Fleischmann, M., P.J. Hendra, and A.J. McQuillan, *Raman spectra of pyridine adsorbed at a silver electrode*. *Chem. Phys. Lett.*, 1974. **26**(2): p. 163-166.
29. Jeanmaire, D.L. and R.P. Van Duyne, *Surface raman spectroelectrochemistry: Part I. Heterocyclic, aromatic, and aliphatic amines adsorbed on the anodized silver electrode*. *J. Electroanal. Chem.*, 1977. **84**(1): p. 1-20.

30. Han, X.X., et al., *Semiconductor-enhanced Raman scattering: active nanomaterials and applications*. *Nanoscale*, 2017. **9**(15): p. 4847-4861.
31. Karthick Kannan, P., et al., *Recent Advances in 2D Inorganic Nanomaterials for SERS Sensing*. *Adv. Mater. Lett.*, 2019. **31**(34): p. 1803432.
32. Lombardi, J.R. and R.L. Birke, *A Unified Approach to Surface-Enhanced Raman Spectroscopy*. *J. Phys. Chem. C*, 2008. **112**(14): p. 5605-5617.
33. Gersten, J.I., *The effect of surface roughness on surface enhanced Raman scattering*. *Chem. Phys.*, 1980. **72**(10): p. 5779-5780.
34. Vo-Dinh, T., et al., *Surface-enhanced Raman spectrometry for trace organic analysis*. *Anal. Chem.*, 1984. **56**(9): p. 1667-1670.
35. Le Ru, E.C. and P.G. Etchegoin, *Principles of Surface-Enhanced Raman Spectroscopy and related plasmonic effects*. 2009, Oxford, UK: Elsevier.
36. Pilot, R., R. Signorini, and L. Fabris, *Surface-Enhanced Raman Spectroscopy: Principles, Substrates, and Applications*. 2018, Switzerland: Springer.
37. Wang, H., et al., *Coupling enhancement mechanisms, materials, and strategies for surface-enhanced Raman scattering devices*. *Analyst*, 2021. **146**: p. 5008.
38. Balčytis, A., et al., *From Fundamental toward Applied SERS: Shared Principles and Divergent Approaches*. *Adv. Opt. Mater.*, 2018. **6**(16): p. 1800292.
39. Lombardi, J.R., et al., *Charge-transfer theory of surface enhanced Raman spectroscopy: Herzberg–Teller contributions*. *Chem. Phys.*, 1986. **84**(8): p. 4174-4180.
40. Leona, M., *Microanalysis of organic pigments and glazes in polychrome works of art by surface-enhanced resonance Raman scattering*. *Proc. Natl. Acad. Sci.*, 2009. **106**(35): p. 14757-14762.
41. Moskovits, M. and J.S. Suh, *Surface Selection Rules for Surface-enhanced Raman Spectroscopy: Calculations and Application to the Surface-enhanced Raman Spectrum of Phthalazine on Silver*. *J. Phys. Chem.*, 1984. **88**(23): p. 5526-5530.
42. Creighton, J.A. *The Selection Rules for Surface-enhanced Raman Spectroscopy*. in *Spectroscopy of Surface*. 1988. New York, NY, USA: Wiley & Sons.
43. Li, J.F., et al., *Core-Shell Nanoparticle-Enhanced Raman Spectroscopy*. *Chem Rev*, 2017. **117**(7): p. 5002-5069.
44. Moskovits, M., *Surface selection rules*. *Chem. Phys.*, 1982. **77**(9): p. 4408-4416.
45. Moskovits, M., *Surface roughness and the enhanced intensity of Raman scattering by molecules adsorbed on metals*. *Chem. Phys.*, 1978. **69**(9): p. 4159-4161.
46. Creighton, J.A., C.G. Blatchford, and M.G. Albrecht, *Plasma resonance enhancement of Raman scattering by pyridine adsorbed on silver or gold sol*

- particles of size comparable to the excitation wavelength.* J. Chem. Soc., Faraday Trans. 2, 1979. **75**(0): p. 790-798.
47. Halouzka, V., et al., *Copper nanowire coated carbon fibers as efficient substrates for detecting designer drugs using SERS.* Talanta (Oxford), 2017. **165**: p. 384-390.
  48. Jiang, T., et al., *Synthesis and improved SERS performance of silver nanoparticles-decorated surface mesoporous silica microspheres.* Appl. Surf. Sci., 2016. **378**: p. 181-190.
  49. Freeman, R.G., et al., *Self-Assembled Metal Colloid Monolayers: An Approach to SERS Substrates.* Science, 1995. **267**(5204): p. 1629-1632.
  50. Solís, D.M., et al., *Optimization of Nanoparticle-Based SERS Substrates through Large-Scale Realistic Simulations.* ACS Photonics, 2017. **4**(2): p. 329-337.
  51. Wang, K., et al., *Facile synthesis of high-performance SiO<sub>2</sub>@Au core-shell nanoparticles with high SERS activity.* RSC Adv, 2018. **8**(54): p. 30825-30831.
  52. Jang, Y.H., et al., *Configuration-controlled Au nanocluster arrays on inverse micelle nano-patterns: versatile platforms for SERS and SPR sensors.* Nanoscale, 2013. **5**(24): p. 12261-12271.
  53. Fan, M. and A.G. Brolo, *Silver Nanoparticles Self Assembly as SERS Substrates with Near Single Molecule Detection Limit.* Phys. Chem. Chem. Phys., 2009. **11**: p. 7381-7389.
  54. Han, Y., et al., *Layer-by-layer Self-assembly of Oppositely Charged Ag Nanoparticles on Silica Microspheres for Trace Analysis of Aqueous Solutions using Surface-enhanced Raman Scattering.* J. Nanosci. Nanotechnol., 2008. **8**(11): p. 5791-800.
  55. Tao, A.R., J. Huang, and P. Yang, *Langmuir-Blodgett of Nanocrystals and Nanowires.* Acc. Chem. Res., 2008. **41**(12): p. 1662-73.
  56. Farling, C.G., et al., *Fabrication of high quality electrochemical SERS (EC-SERS) substrates using physical vapour deposition.* Phys. Chem. Chem. Phys., 2021. **23**: p. 20065.
  57. Chang, Y., Y. Lu, and Y. Hung, *Controlling the Nanoscale Gaps on Silver Island Film for Efficient Surface-Enhanced Raman Spectroscopy.* Nanomaterials, 2019. **9**: p. 470.
  58. Zhu, Z., et al., *Fabrication of Surface-Enhanced Raman Spectroscopy (SERS) – Active Electrodes by Silver Sputtering Deposition for Electrochemical SERS Analysis.* Electroanalysis, 2018. **30**(7): p. 1432-1437.
  59. Wu, W., et al., *Low-Cost, Disposable, Flexible and Highly Reproducible Screen Printed SERS Substrates for the Detection of Various Chemicals.* Sci. Rep., 2015. **5**.

60. Qu, L., et al., *Batch Fabrication of Disposable Screen-Printed SERS Arrays*. Lab Chip, 2012. **12**(5): p. 876-881.
61. Alberti, G., et al., *MIP-Based Screen-Printed Potentiometric Cell for Atrazine Sensing*. Chemosensors, 2022. **10**(8): p. 339.
62. Le Ru, E.C., et al., *Surface Enhanced Raman Scattering Enhancement Factors: A Comprehensive Study*. J. Phys. Chem. C, 2007. **111**(37): p. 13794-13803.
63. Gupta, R. and W.A. Weimer, *High enhancement factor gold films for surface enhanced Raman spectroscopy*. Chem. Phys. Lett., 2003. **374**(3-4): p. 302-306.
64. Liu, Y., et al., *Localized and propagating surface plasmon co-enhanced Raman spectroscopy based on evanescent field excitation*. Chem. Commun., 2011. **47**: p. 3784–3786.
65. Park, J.E., Y. Lee, and J.M. Nam, *Precisely Shaped, Uniformly Formed Gold Nanocubes with Ultrahigh Reproducibility in Single Particle Scattering and Surface-Enhanced Raman Scattering and Surface-Enhanced Raman Scattering*. Nano Lett., 2018. **18**: p. 6475-6482.
66. Roriguez-Torres, M.P., L.A. Diaz-Torres, and S. Romero-Servin, *Heparin Assisted Photochemical Synthesis of Gold Nanoparticles and Their Performance as SERS Substrates*. Int. J. Mol. Sci., 2014. **15**: p. 19239-19252.
67. Michota, A. and J. Bukowska, *Surface-enhanced Raman Scattering (SERS) of 4-mercaptobenzoic Acid on Silver and Gold Substrates*. J. Raman Spectrosc., 2002. **34**(1): p. 21-25.
68. Dieringer, J.A., et al., *Surface-Enhanced Raman Excitation Spectroscopy of a Single Rhodamine 6G Molecule*. J. Am. Chem. Soc., 2008. **131**: p. 849-854.
69. Agarwal, N.R., et al., *Au Nanoparticle Arrays Produced by Pulsed Laser Deposition for Surface Enhanced Raman Spectroscopy*. Appl. Surf. Sci., 2012. **258**: p. 9148-9152.
70. He, X.N., et al., *Surface-enhanced Raman Spectroscopy using Gold-coated Horizontally Aligned Carbon Nanotubes*. Nanotechnology, 2012. **23**: p. 205702.
71. Zhong, F., et al., *Porous Silicon Photonic Crystals Coated with Ag Nanoparticles as Efficient Substrates for Detecting Trace Explosives Using SERS*. Nanomaterials, 2018. **8**: p. 872.
72. Watanabe, H., et al., *DFT Vibrational Calculations of Rhodamine 6G Adsorbed on Silver: Analysis of Tip-Enhanced Raman Spectroscopy*. J. Phys. Chem. B, 2005. **109**: p. 5012-5020.
73. Greasley, S.L., et al., *Controlling Particle Size in the Stober Process and Incorporation of Calcium*. J. Colloid Interface Sci., 2016. **469**: p. 213-223.



74. Cipriotti, S.V., et al., *Thermal Behavior and Structural Study of SiO<sub>2</sub>/Poly( $\epsilon$ -caprolactone) Hybrids Synthesized via Sol-Gel Method*. *Materials*, 2018. **11**: p. 275.
75. Mueller, R., et al., *OH Surface Density of SiO<sub>2</sub> and TiO<sub>2</sub> by Thermogravimetric Analysis*. *Langmuir*, 2003. **19**: p. 160-165.
76. Brito-Silva, A.M., et al., *Improved Synthesis of Gold and Silver Nanoshells*. *Langmuir*, 2013. **29**(13): p. 4366-72.
77. Lin, H., et al., *The Rheological Behaviors of Screen-printing Pastes*. *J. Mater. Process Technol.*, 2008. **197**: p. 7.
78. McGillivray, D., *Synthesis and Characterization of Nanostructured Catalysts for Photovoltaic Applications*, in *Faculty of Science*. 2013, University of Ontario Institute of Technology: ProQuest Dissertations Publishing.
79. Gundanna, S.K., et al., *Effect of Thermal Treatment on the Surface/interfacial Behaviour of Au@SiO<sub>2</sub> Nanoparticles in the Presence of CTAB Surfactant Molecules*. *Powder Technol.*, 2021. **381**: p. 503-508.
80. Javdani, H., et al., *Tannic Acid-templated Mesoporous Silica Nanoparticles as an Effective Treatment in Acute Ferrous Sulfate Poisoning*. *Microporous Mesoporous Mater.*, 2020. **307**: p. 110486.
81. Thommes, M., et al., *Physisorption of gases, with special reference to the evaluation of surface area and pore size distribution (IUPAC Technical Report)*. *Pure Appl. Chem.*, 2015. **87**(9-10): p. 1051-1069.
82. Vazquez, N.I., et al., *Synthesis of Mesoporous Silica Nanoparticles by sol-gel as Nanocontainer for Future Drug Delivery Applications*. *Bol. Soc. Esp. Ceram. Vidr*, 2017. **56**: p. 139-145.
83. Walcarius, A., et al., *Electrochemically Assisted Self-assembly of Mesoporous Silica Thin Films*. *Nat. Mater.*, 2007. **6**(8): p. 602-608.
84. Liu, Y., et al., *Silica nanoparticles separation from water: aggregation by cetyltrimethylammonium bromide (CTAB)*. *Chemosphere*, 2013. **92**: p. 681-687.
85. Schneider, C.A., W.S. Rasband, and K.W. Eliceiri, *NIH Image to ImageJ: 25 years of image analysis*. *Nat. Methods*, 2012. **9**(7): p. 671-675.
86. Zuber, A., et al., *Detection of gold nanoparticles with different sizes using absorption and fluorescence based method*. *Sens. Actuators B Chem.*, 2015. **227**: p. 117-127.
87. Amendola, V. and M. Meneghetti, *Size Evaluation of Gold Nanoparticles by UV-vis Spectroscopy*. *J. Phys. Chem. C*, 2009. **113**: p. 4277-4285.
88. Wang, C., et al., *Polyethylenimine-interlayered Silver-shell Magnetic-core Microspheres as Multifunctional SERS Substrates*. *J. Mater. Chem. A*, 2015. **3**: p. 8684.

89. Fang, Y., et al., *Self-Assembly of Cationic Polyelectrolyte-Functionalized Graphene Nanosheets and Gold Nanoparticles: A Two-Dimensional Heterostructure for Hydrogen Peroxide Sensing*. Langmuir, 2010. **26**: p. 11277-11282.
90. Depciuch, J., et al., *From Spherical to Bone-shaped Gold Nanoparticles—Time factor in the Formation of Au NPs, their Optical and Photothermal Properties*. Photodiagnosis and Photodyn. Ther., 2020. **30**: p. 101670.
91. Haiss, W., et al., *Determination of Size and Concentration of Gold Nanoparticles from UV-Vis Spectra*. Anal. Chem., 2007. **79**: p. 4215-4221.
92. Olteanu, N.L., et al., *“One-pot” synthesis of fluorescent Au@SiO<sub>2</sub> and SiO<sub>2</sub>@Au nanoparticles*. Arab. J. Chem., 2016. **9**: p. 854-864.
93. Lesovoy, L., F. Matiko, and B. Chaban, *Equation of Arithmetic Mean Deviation of Roughness Profile*. Syst. Sci. Control. Eng., 2019. **5**: p. 81-88.
94. Lee, C., et al., *Thickness of a Metallic Film, in Addition to its Roughness, Plays a Significant Role in SERS Activity*. Sci. Rep., 2015. **5**(1): p. 11644.
95. Schneidewind, H., et al., *The Effect of Silver Thickness on the Enhancement of Polymer Based SERS Substrates*. Nanotechnology, 2014. **25**: p. 445203.
96. Kaltenbach, H., *A Concise Guide to Statistics*. 2012: Scholars Portal.
97. Ostertagova, E., O. Ostertag, and J. Kovac, *Methodology and Application of the Kruskal-Wallis Test*. Appl. Mech. Mater., 2014. **611**: p. 115-120.
98. Smith, E. and G. Dent, *Surface-Enhanced Raman Scattering and Surface-Enhanced Resonance Raman Scattering*, in *Modern Raman Spectroscopy – A Practical Approach*. 2004. p. 113-133.
99. Agarwal, N.R., P.M. Ossi, and S. Trusso, *Driving electromagnetic field enhancements in tailored gold surface nanostructures: Optical properties and macroscale simulations*. Appl. Surf. Sci., 2019. **466**: p. 19-27.
100. Nagashree, K.L., et al., *Spontaneous formation of branched nanochains from room temperature molten amides: visible and near-IR active, SERS substrates for non-fluorescent and fluorescent analytes*. RSC Adv., 2013. **3**: p. 8356.
101. Abdelsalam, M.E., et al., *Electrochemical SERS at a Structured Gold Surface*. Electrochem. Commun., 2005. **7**: p. 740-744.
102. Yukhymchuk, V.O., et al., *Efficient core-SiO<sub>2</sub>/shell-Au Nanostructures for Surface Enhanced Raman Scattering*. Semicond. Phys. Quantum Electron. Optoelectron., 2014. **17**: p. 217-221.
103. Rodrigues, D.C., et al., *Critical Assessment of Enhancement Factor Measurements in Surface-enhanced Raman scattering on Different Substrates*. Phys. Chem. Chem. Phys., 2015. **17**: p. 21294.

104. Yang, H., et al., *Hybrid nanostructure of SiO<sub>2</sub>@Si with Au-nanoparticles for surface enhanced Raman spectroscopy*. *Nanoscale*, 2019. **11**: p. 13484.
105. Bassi, B., et al., *Robust, reproducible, recyclable SERS substrates: monolayers of gold nanostars grafted on glass and coated with a thin silica layer*. *Nanotechnology*, 2019. **30**(2): p. 025302.

## Appendices

### Appendix A

#### A1. Monolayer and Multilayer Au/silica films (Method 1)

This section discusses the reference system prepared by method 2, introduced in Chapter 2. Using this method, the resulting substrates were SERS active, making it a good starting point for the substrate development process. SERS Spectra of R6G at 100  $\mu\text{M}$  were obtained with the following Raman Parameters: 50 mW of 532 nm excitation at 1% nominal power and 10 second integration time for 3 accumulations 50x magnification. The lowest detectable concentration was 100  $\mu\text{M}$  R6G.

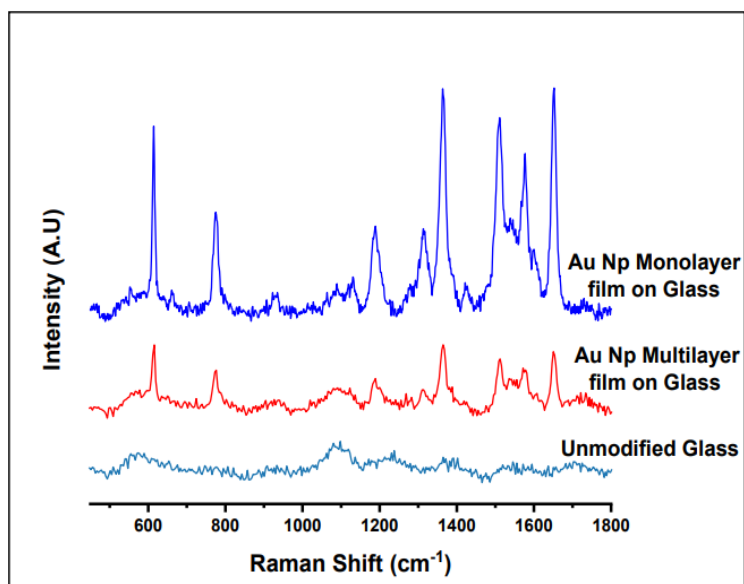
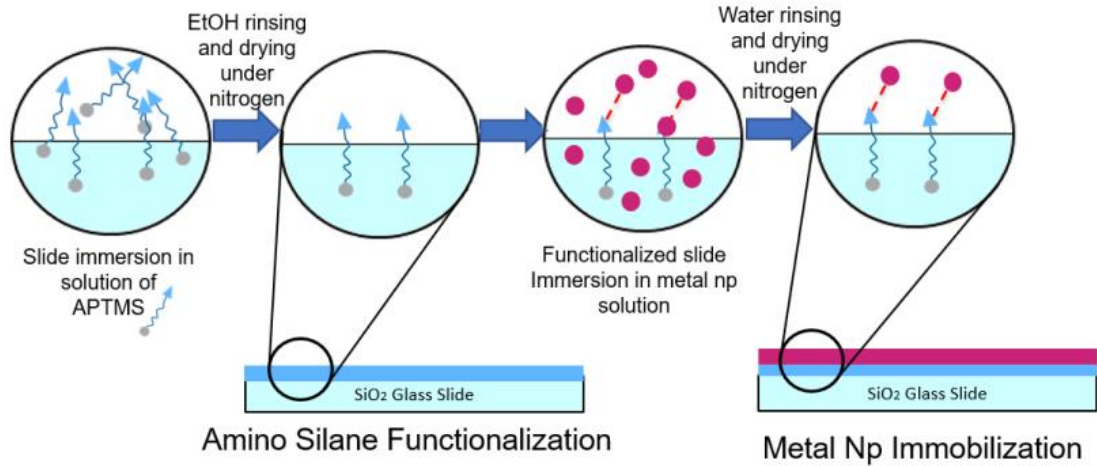
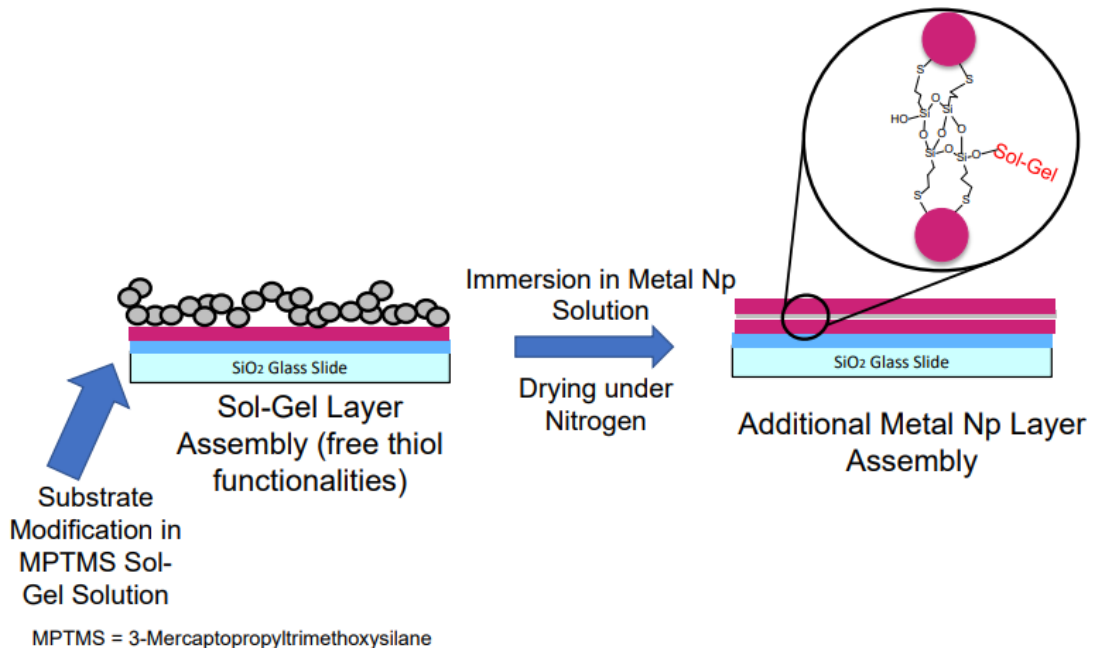


**Figure A1.1.** SERS Spectra of R6G at 100  $\mu\text{M}$  obtained on Au Nps monolayer and multilayer films on glass. Raman Parameters: 50 mW of 532 nm excitation at 1% nominal power and 10 second integration time for 3 accumulations 50x magnification



APTMS = 3-aminopropyltrimethoxysilane

**Figure A1.2.** Schematic of Self-assembled Monolayer with Aminosilane (APTMS) Functionalization

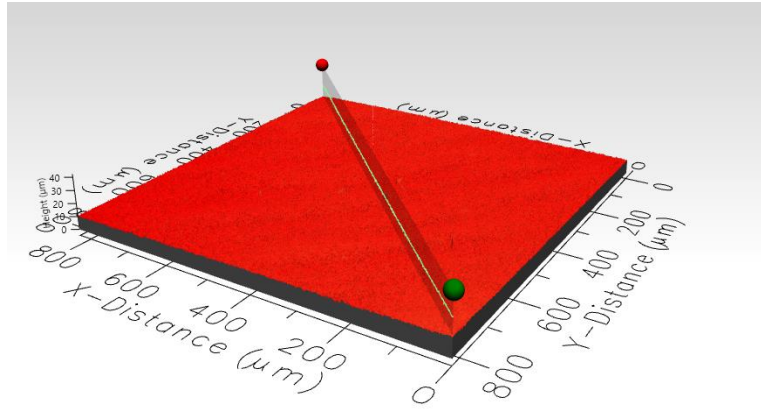


MPTMS = 3-Mercaptopropyltrimethoxysilane

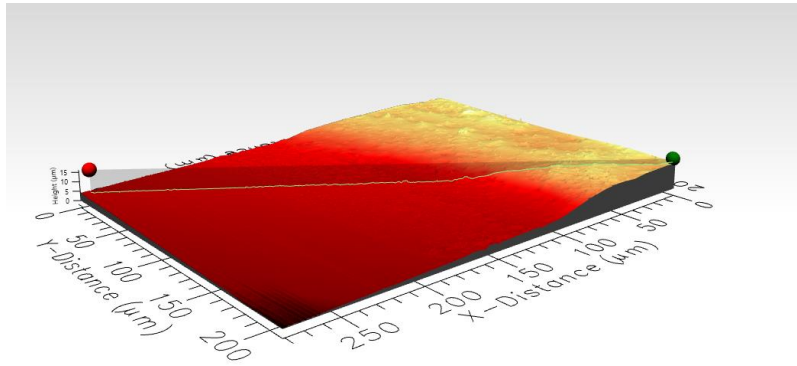
**Figure A1.3.** Multilayer Deposition with Sol-Gel MPTMS Solution

## A2. Surface Topographic images (Profilometry Results)

**s-SiO<sub>2</sub>**



**Au@s-SiO<sub>2</sub>**



**Au@s-SiO<sub>2</sub>**

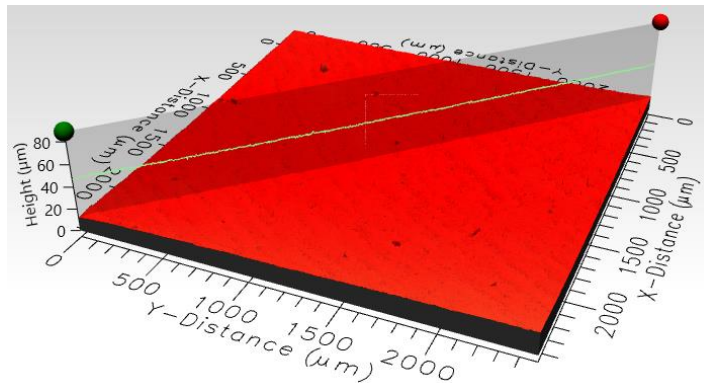


**Figure A2.1** Surface Topographic images of calcinated s-SiO<sub>2</sub> film and Au@s-SiO<sub>2</sub> film on glass obtained with a 3D profilometer equipped with white light interferometry detection. The Au@s-SiO<sub>2</sub> film was measured on the edge

**t-SiO<sub>2</sub>**

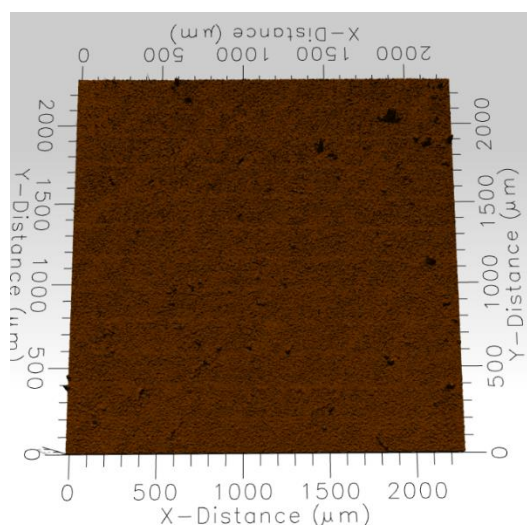
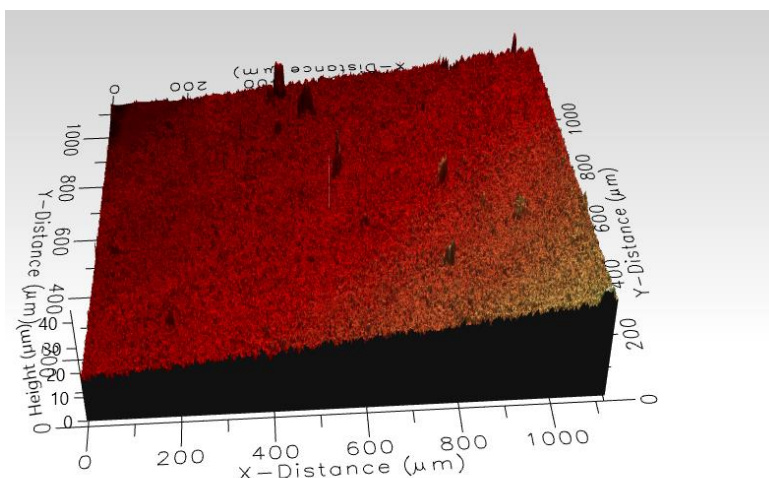


**Figure A2.2** Surface Topographic images of calcinated t-SiO<sub>2</sub> films on glass obtained with a 3D profilometer equipped with white light interferometry detection

Figure A2.2 illustrates the uniformity in film thickness once the Au is deposited on the t-SiO<sub>2</sub> film. The t-SiO<sub>2</sub> film inhabits many regions of different heights and the frequency of different heights occurring on the film is higher than that for the Au@t-SiO<sub>2</sub> film (Figure A2.1), nonetheless roughness is still observed. The smooth area of the Au@s-SiO<sub>2</sub> film stems from the glass slide which the film is deposited on, as this image was obtained on the edge of the film (Figure A2.1, middle) This is a practice that

provides a distinction between the film and the leveled solid support, and highlights the thickness and surface features.

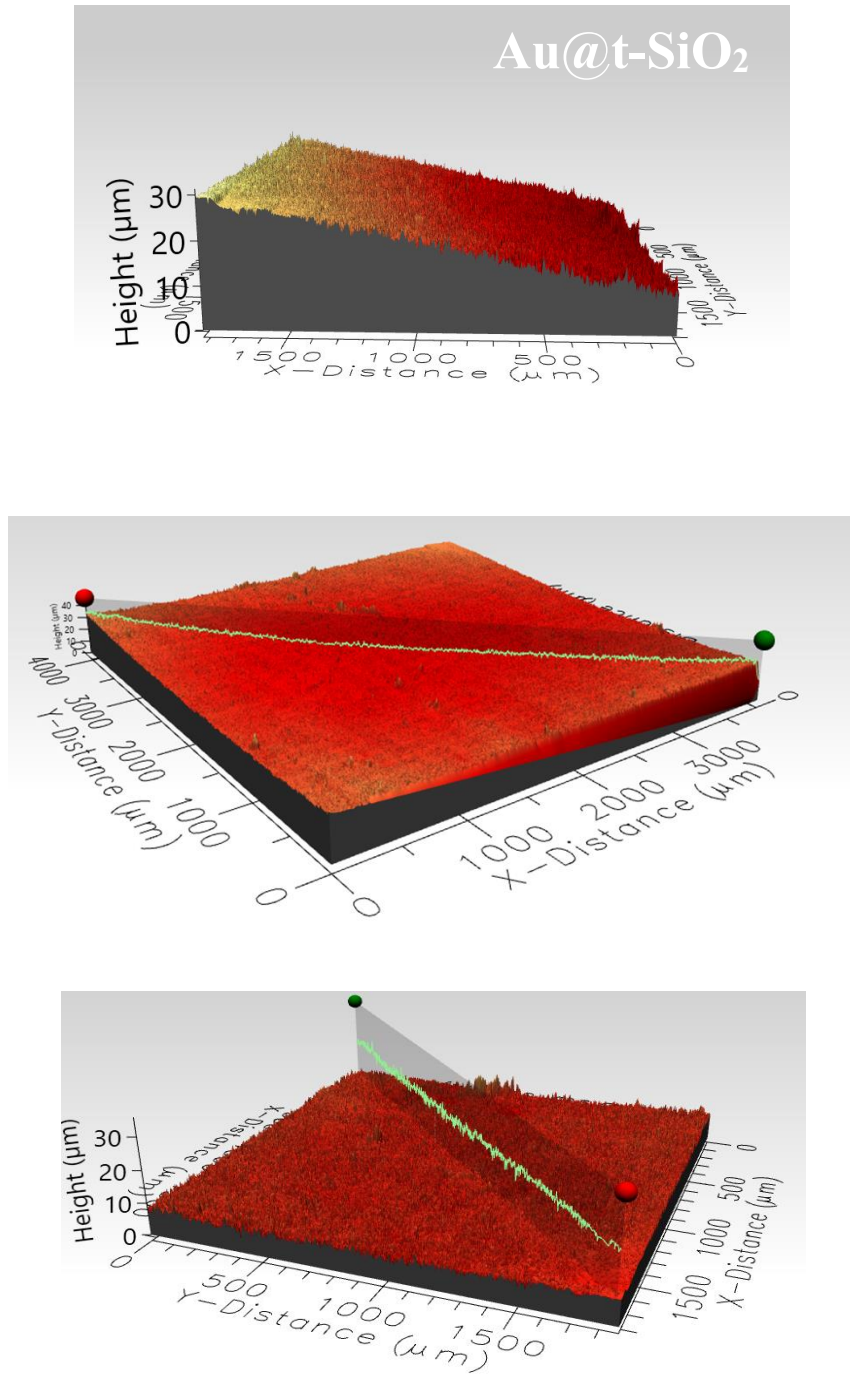
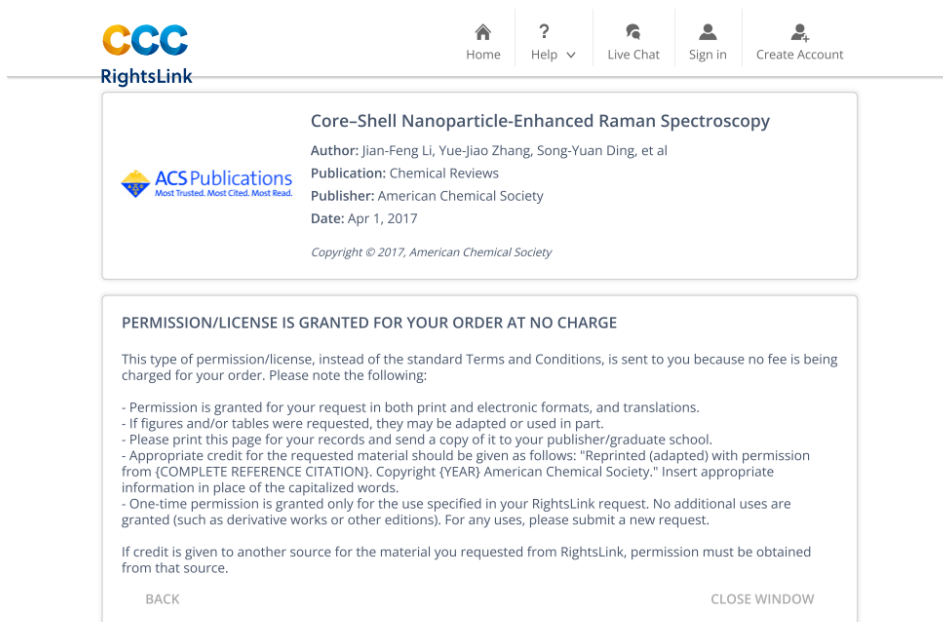


**Figure A2.3.** Surface Topographic images of Au@t-SiO<sub>2</sub> films on glass obtained with a 3D profilometer equipped with white light interferometry detection



### A3. Permission to Reprint

**Figure 1.8.** Timeline of SERS substrate development since discovery (a) The first SERS effect discovered on roughened Ag electrode, (b) SERS of Ag or Au colloids, of (c) silver nanoislands on n-GaAs electrode demonstrating “borrowing” strategy also highlighted by (d) deposited transition metal on roughened Au electrode, (e) single molecule SERS, (f) silica core-Au shell nanoparticle, (g) UPD and redox replacement transition metal on Au nanoparticles, (h) SERS tag, (i) Au core-transition metal shell nanoparticles, (j) Ag film on nanosphere (AgFON) substrates with an alumina layer, (k) silica shell isolated nanoparticles (SHINERS), and (l) graphene shell isolated nanoparticles. Reprinted (adapted) with permission from {Li, J.F., et al., *Core-Shell Nanoparticle-Enhanced Raman Spectroscopy*. Chem. Rev., 2017. **117**(7): p. 5002-5069}. Copyright {2017} American Chemical Society



The screenshot shows the ACS RightsLink interface. At the top, there is a navigation bar with icons for Home, Help, Live Chat, Sign in, and Create Account. Below the navigation bar, the main content area displays the following information:

**CCC RightsLink**

**Core-Shell Nanoparticle-Enhanced Raman Spectroscopy**  
Author: Jian-Feng Li, Yue-Jiao Zhang, Song-Yuan Ding, et al  
Publication: Chemical Reviews  
Publisher: American Chemical Society  
Date: Apr 1, 2017  
Copyright © 2017, American Chemical Society

**PERMISSION/LICENSE IS GRANTED FOR YOUR ORDER AT NO CHARGE**

This type of permission/license, instead of the standard Terms and Conditions, is sent to you because no fee is being charged for your order. Please note the following:

- Permission is granted for your request in both print and electronic formats, and translations.
- If figures and/or tables were requested, they may be adapted or used in part.
- Please print this page for your records and send a copy of it to your publisher/graduate school.
- Appropriate credit for the requested material should be given as follows: "Reprinted (adapted) with permission from (COMPLETE REFERENCE CITATION). Copyright (YEAR) American Chemical Society." Insert appropriate information in place of the capitalized words.
- One-time permission is granted only for the use specified in your RightsLink request. No additional uses are granted (such as derivative works or other editions). For any uses, please submit a new request.

If credit is given to another source for the material you requested from RightsLink, permission must be obtained from that source.

BACK CLOSE WINDOW

**Figure 1.9.** Simulation of maximum SERS enhancement for planar monolayers of particles with different morphology: Au Nanostars (GNS), Au Nanorods (GNR), Au Nanospheres (GNP). Reprinted (adapted) with permission from {Solís, D.M., et al., *Optimization of Nanoparticle-Based SERS Substrates through Large-Scale Realistic Simulations*. ACS Photonics, 2017. 4(2): p. 329-337}. Copyright {2017} American Chemical Society. The image was obtained from <https://pubs.acs.org/doi/10.1021/acsp Photonics.6b00786>. Further permissions related to the material excerpted should be directed to the ACS.



ACS Publications <acs@service-now.com>  
Fri 12-09, 12:54 AM  
Raquel Simpson

Reply all

Flag for follow up. Start by December-09-22. Due by December-09-22.

[EXTERNAL EMAIL - USE CAUTION]

Dear Dr. Simpson,

Thank you for contacting ACS Publications Support.

Your permission requested is granted and there is no fee for this reuse. In your planned reuse, you must cite the ACS article as the source, add this direct link <https://pubs.acs.org/doi/10.1021/acsp Photonics.6b00786>, and include a notice to readers that further permissions related to the material excerpted should be directed to the ACS.

If you need further assistance, please let me know.

Best regards,  
Keith Pearl

~~~~~  
Keith Pearl  
ACS Publications Support  
Customer Services & Information  
Website: <https://acs.service-now.com/acs>  
Email: [support@services.acs.org](mailto:support@services.acs.org)  
Phone: 800-227-9919 | 202-872-(HELP) 4357

**Figure 3.9.** Viscosity vs. shear rate curve for literature paste systems containing 50 wt% of filler (3  $\mu\text{m}$   $\text{SiO}_2$ , 3  $\mu\text{m}$  silane-functionalized  $\text{SiO}_2$ , or a dielectric powder) and the same binding agent (ethyl cellulose), and organic solvent ( $\alpha$ -terpineol) used in this work at 6 wt% and 44% respectively. Reprinted from J. Mater. Process. Technol., **197**, Lin, H.C., C.; Hwu, W.; Ger, M., *The Rheological Behaviors Of Screen-Printing Pastes*, p. 7., Copyright (2007), with permission from Elsevier.

**ELSEVIER LICENSE  
TERMS AND CONDITIONS**

Dec 11, 2022

---

This Agreement between Ontario Tech University -- Raquel Simpson ("You") and Elsevier ("Elsevier") consists of your license details and the terms and conditions provided by Elsevier and Copyright Clearance Center.

|                              |                                                          |
|------------------------------|----------------------------------------------------------|
| License Number               | 5445980565391                                            |
| License date                 | Dec 11, 2022                                             |
| Licensed Content Publisher   | Elsevier                                                 |
| Licensed Content Publication | Journal of Materials Processing Technology               |
| Licensed Content Title       | The rheological behaviors of screen-printing pastes      |
| Licensed Content Author      | Hung-Wen Lin, Chang-Pin Chang, Wen-Hwa Hwu, Ming-Der Ger |
| Licensed Content Date        | Feb 1, 2008                                              |
| Licensed Content Volume      | 197                                                      |
| Licensed Content Issue       | 1-3                                                      |
| Licensed Content Pages       | 8                                                        |
| Start Page                   | 284                                                      |
| End Page                     | 291                                                      |

|                                              |                                                                                                                                           |
|----------------------------------------------|-------------------------------------------------------------------------------------------------------------------------------------------|
| Type of Use                                  | reuse in a thesis/dissertation                                                                                                            |
| Portion                                      | figures/tables/illustrations                                                                                                              |
| Number of figures/tables/illustrations       | 1                                                                                                                                         |
| Format                                       | both print and electronic                                                                                                                 |
| Are you the author of this Elsevier article? | No                                                                                                                                        |
| Will you be translating?                     | No                                                                                                                                        |
| Title                                        | Performance Assessment of Au SERS Substrates Prepared by Deposition of Au Nanoparticles on Screen-Printed SiO <sub>2</sub> Particle Films |
| Institution name                             | Ontario Tech University                                                                                                                   |
| Expected presentation date                   | Jan 2023                                                                                                                                  |
| Portions                                     | Figure 2                                                                                                                                  |
| Requestor Location                           | Ontario Tech University<br>2000 Simcoe St North<br><br>Oshawa, ON L1G 0C5<br>Canada<br>Attn: Ontario Tech University                      |
| Publisher Tax ID                             | GB 494 6272 12                                                                                                                            |
| Total                                        | 0.00 CAD                                                                                                                                  |
| Terms and Conditions                         |                                                                                                                                           |

**INTRODUCTION**

1. The publisher for this copyrighted material is Elsevier. By clicking "accept" in connection with completing this licensing transaction, you agree that the following terms and conditions apply to this transaction (along with the Billing and Payment terms and conditions established by Copyright Clearance Center, Inc. ("CCC"), at the time that you opened your Rightslink account and that are available at any time at <http://myaccount.copyright.com>).

#### GENERAL TERMS

2. Elsevier hereby grants you permission to reproduce the aforementioned material subject to the terms and conditions indicated.

3. Acknowledgement: If any part of the material to be used (for example, figures) has appeared in our publication with credit or acknowledgement to another source, permission must also be sought from that source. If such permission is not obtained then that material may not be included in your publication/copies. Suitable acknowledgement to the source must be made, either as a footnote or in a reference list at the end of your publication, as follows:

"Reprinted from Publication title, Vol /edition number, Author(s), Title of article / title of chapter, Pages No., Copyright (Year), with permission from Elsevier [OR APPLICABLE SOCIETY COPYRIGHT OWNER]." Also Lancet special credit - "Reprinted from The Lancet, Vol. number, Author(s), Title of article, Pages No., Copyright (Year), with permission from Elsevier."

4. Reproduction of this material is confined to the purpose and/or media for which permission is hereby given.

5. Altering/Modifying Material: Not Permitted. However figures and illustrations may be altered/adapted minimally to serve your work. Any other abbreviations, additions, deletions and/or any other alterations shall be made only with prior written authorization of Elsevier Ltd. (Please contact Elsevier's permissions helpdesk [here](#)). No modifications can be made to any Lancet figures/tables and they must be reproduced in full.

6. If the permission fee for the requested use of our material is waived in this instance, please be advised that your future requests for Elsevier materials may attract a fee.

7. Reservation of Rights: Publisher reserves all rights not specifically granted in the combination of (i) the license details provided by you and accepted in the course of this licensing transaction, (ii) these terms and conditions and (iii) CCC's Billing and Payment terms and conditions.

8. License Contingent Upon Payment: While you may exercise the rights licensed immediately upon issuance of the license at the end of the licensing process for the transaction, provided that you have disclosed complete and accurate details of your proposed use, no license is finally effective unless and until full payment is received from you (either by publisher or by CCC) as provided in CCC's Billing and Payment terms and conditions. If full payment is not received on a timely basis, then any license preliminarily granted shall be deemed automatically revoked and shall be void as if never granted. Further, in the event that you breach any of these terms and conditions or any of CCC's Billing and Payment terms and conditions, the license is automatically revoked and shall be void as if never granted. Use of materials as described in a revoked license, as well as any use of the materials beyond the scope of an unrevoked license, may constitute copyright infringement and publisher reserves the right to take any and all action to protect its copyright in the materials.

9. **Warranties:** Publisher makes no representations or warranties with respect to the licensed material.

10. **Indemnity:** You hereby indemnify and agree to hold harmless publisher and CCC, and their respective officers, directors, employees and agents, from and against any and all claims arising out of your use of the licensed material other than as specifically authorized pursuant to this license.

11. **No Transfer of License:** This license is personal to you and may not be sublicensed, assigned, or transferred by you to any other person without publisher's written permission.

12. **No Amendment Except in Writing:** This license may not be amended except in a writing signed by both parties (or, in the case of publisher, by CCC on publisher's behalf).

13. **Objection to Contrary Terms:** Publisher hereby objects to any terms contained in any purchase order, acknowledgment, check endorsement or other writing prepared by you, which terms are inconsistent with these terms and conditions or CCC's Billing and Payment terms and conditions. These terms and conditions, together with CCC's Billing and Payment terms and conditions (which are incorporated herein), comprise the entire agreement between you and publisher (and CCC) concerning this licensing transaction. In the event of any conflict between your obligations established by these terms and conditions and those established by CCC's Billing and Payment terms and conditions, these terms and conditions shall control.

14. **Revocation:** Elsevier or Copyright Clearance Center may deny the permissions described in this License at their sole discretion, for any reason or no reason, with a full refund payable to you. Notice of such denial will be made using the contact information provided by you. Failure to receive such notice will not alter or invalidate the denial. In no event will Elsevier or Copyright Clearance Center be responsible or liable for any costs, expenses or damage incurred by you as a result of a denial of your permission request, other than a refund of the amount(s) paid by you to Elsevier and/or Copyright Clearance Center for denied permissions.

#### LIMITED LICENSE

The following terms and conditions apply only to specific license types:

15. **Translation:** This permission is granted for non-exclusive world **English** rights only unless your license was granted for translation rights. If you licensed translation rights you may only translate this content into the languages you requested. A professional translator must perform all translations and reproduce the content word for word preserving the integrity of the article.

16. **Posting licensed content on any Website:** The following terms and conditions apply as follows: Licensing material from an Elsevier journal: All content posted to the web site must maintain the copyright information line on the bottom of each image; A hyper-text must be included to the Homepage of the journal from which you are licensing at <http://www.sciencedirect.com/science/journal/xxxxx> or the Elsevier homepage for books at <http://www.elsevier.com>; Central Storage: This license does not include permission for a scanned version of the material to be stored in a central repository such as that provided by Heron/XanEdu.

Licensing material from an Elsevier book: A hyper-text link must be included to the Elsevier homepage at <http://www.elsevier.com>. All content posted to the web site must maintain the copyright information line on the bottom of each image.

**Posting licensed content on Electronic reserve:** In addition to the above the following clauses are applicable: The web site must be password-protected and made available only to bona fide students registered on a relevant course. This permission is granted for 1 year only. You may obtain a new license for future website posting.

17. For journal authors: the following clauses are applicable in addition to the above:

**Preprints:**

A preprint is an author's own write-up of research results and analysis, it has not been peer-reviewed, nor has it had any other value added to it by a publisher (such as formatting, copyright, technical enhancement etc.).

Authors can share their preprints anywhere at any time. Preprints should not be added to or enhanced in any way in order to appear more like, or to substitute for, the final versions of articles however authors can update their preprints on arXiv or RePEc with their Accepted Author Manuscript (see below).

If accepted for publication, we encourage authors to link from the preprint to their formal publication via its DOI. Millions of researchers have access to the formal publications on ScienceDirect, and so links will help users to find, access, cite and use the best available version. Please note that Cell Press, The Lancet and some society-owned have different preprint policies. Information on these policies is available on the journal homepage.

**Accepted Author Manuscripts:** An accepted author manuscript is the manuscript of an article that has been accepted for publication and which typically includes author-incorporated changes suggested during submission, peer review and editor-author communications.

Authors can share their accepted author manuscript:

- immediately
  - via their non-commercial person homepage or blog
  - by updating a preprint in arXiv or RePEc with the accepted manuscript
  - via their research institute or institutional repository for internal institutional uses or as part of an invitation-only research collaboration work-group
  - directly by providing copies to their students or to research collaborators for their personal use
  - for private scholarly sharing as part of an invitation-only work group on commercial sites with which Elsevier has an agreement
- After the embargo period
  - via non-commercial hosting platforms such as their institutional repository
  - via commercial sites with which Elsevier has an agreement

In all cases accepted manuscripts should:

- link to the formal publication via its DOI
- bear a CC-BY-NC-ND license - this is easy to do
- if aggregated with other manuscripts, for example in a repository or other site, be shared in alignment with our hosting policy not be added to or enhanced in any way to appear more like, or to substitute for, the published journal article.

**Published journal article (JPA):** A published journal article (PJA) is the definitive final record of published research that appears or will appear in the journal and embodies all



value-adding publishing activities including peer review co-ordination, copy-editing, formatting, (if relevant) pagination and online enrichment.

Policies for sharing publishing journal articles differ for subscription and gold open access articles:

**Subscription Articles:** If you are an author, please share a link to your article rather than the full-text. Millions of researchers have access to the formal publications on ScienceDirect, and so links will help your users to find, access, cite, and use the best available version.

Theses and dissertations which contain embedded PJAs as part of the formal submission can be posted publicly by the awarding institution with DOI links back to the formal publications on ScienceDirect.

If you are affiliated with a library that subscribes to ScienceDirect you have additional private sharing rights for others' research accessed under that agreement. This includes use for classroom teaching and internal training at the institution (including use in course packs and courseware programs), and inclusion of the article for grant funding purposes.

**Gold Open Access Articles:** May be shared according to the author-selected end-user license and should contain a [CrossMark logo](#), the end user license, and a DOI link to the formal publication on ScienceDirect.

Please refer to Elsevier's [posting policy](#) for further information.

18. **For book authors** the following clauses are applicable in addition to the above: Authors are permitted to place a brief summary of their work online only. You are not allowed to download and post the published electronic version of your chapter, nor may you scan the printed edition to create an electronic version. **Posting to a repository:** Authors are permitted to post a summary of their chapter only in their institution's repository.

19. **Thesis/Dissertation:** If your license is for use in a thesis/dissertation your thesis may be submitted to your institution in either print or electronic form. Should your thesis be published commercially, please reapply for permission. These requirements include permission for the Library and Archives of Canada to supply single copies, on demand, of the complete thesis and include permission for Proquest/UMI to supply single copies, on demand, of the complete thesis. Should your thesis be published commercially, please reapply for permission. Theses and dissertations which contain embedded PJAs as part of the formal submission can be posted publicly by the awarding institution with DOI links back to the formal publications on ScienceDirect.

#### **Elsevier Open Access Terms and Conditions**

You can publish open access with Elsevier in hundreds of open access journals or in nearly 2000 established subscription journals that support open access publishing. Permitted third party re-use of these open access articles is defined by the author's choice of Creative Commons user license. See our [open access license policy](#) for more information.

#### **Terms & Conditions applicable to all Open Access articles published with Elsevier:**

Any reuse of the article must not represent the author as endorsing the adaptation of the article nor should the article be modified in such a way as to damage the author's honour or reputation. If any changes have been made, such changes must be clearly indicated.

The author(s) must be appropriately credited and we ask that you include the end user license and a DOI link to the formal publication on ScienceDirect.

If any part of the material to be used (for example, figures) has appeared in our publication with credit or acknowledgement to another source it is the responsibility of the user to ensure their reuse complies with the terms and conditions determined by the rights holder.

**Additional Terms & Conditions applicable to each Creative Commons user license:**

**CC BY:** The CC-BY license allows users to copy, to create extracts, abstracts and new works from the Article, to alter and revise the Article and to make commercial use of the Article (including reuse and/or resale of the Article by commercial entities), provided the user gives appropriate credit (with a link to the formal publication through the relevant DOI), provides a link to the license, indicates if changes were made and the licensor is not represented as endorsing the use made of the work. The full details of the license are available at <http://creativecommons.org/licenses/by/4.0>.

**CC BY NC SA:** The CC BY-NC-SA license allows users to copy, to create extracts, abstracts and new works from the Article, to alter and revise the Article, provided this is not done for commercial purposes, and that the user gives appropriate credit (with a link to the formal publication through the relevant DOI), provides a link to the license, indicates if changes were made and the licensor is not represented as endorsing the use made of the work. Further, any new works must be made available on the same conditions. The full details of the license are available at <http://creativecommons.org/licenses/by-nc-sa/4.0>.

**CC BY NC ND:** The CC BY-NC-ND license allows users to copy and distribute the Article, provided this is not done for commercial purposes and further does not permit distribution of the Article if it is changed or edited in any way, and provided the user gives appropriate credit (with a link to the formal publication through the relevant DOI), provides a link to the license, and that the licensor is not represented as endorsing the use made of the work. The full details of the license are available at <http://creativecommons.org/licenses/by-nc-nd/4.0>. Any commercial reuse of Open Access articles published with a CC BY NC SA or CC BY NC ND license requires permission from Elsevier and will be subject to a fee.

Commercial reuse includes:

- Associating advertising with the full text of the Article
- Charging fees for document delivery or access
- Article aggregation
- Systematic distribution via e-mail lists or share buttons

Posting or linking by commercial companies for use by customers of those companies.

**20. Other Conditions:**

v1.10

Questions? [customercare@copyright.com](mailto:customercare@copyright.com) or +1-855-239-3415 (toll free in the US) or +1-978-646-2777.

**Figure 1.10.** SERS spectra collected on Au thin films soaked in aqueous R6G solutions from  $1 \times 10^{-4}$  to  $1 \times 10^{-10}$  M. Au film were prepared via pulsed laser ablation using a KrF excimer laser ( $\lambda = 248$  nm, pulse width 25 ns, repetition rate 10 Hz) in the presence of controlled Argon and pressure value of 100 Pa. Reprinted from Appl. Surf. Sci., **258**, N. R. Agarwal, F. Neri, S. Trussoc, A. Lucotti and P. M. Ossi, Au nanoparticle arrays produced by Pulsed Laser Deposition for Surface Enhanced Raman Spectroscopy, p. 9148-9152, Copyright (2012), with permission from Elsevier

ELSEVIER LICENSE  
TERMS AND CONDITIONS

Dec 08, 2022

---

This Agreement between Ontario Tech University -- Raquel Simpson ("You") and Elsevier ("Elsevier") consists of your license details and the terms and conditions provided by Elsevier and Copyright Clearance Center.

|                              |                                                                                                    |
|------------------------------|----------------------------------------------------------------------------------------------------|
| License Number               | 5444400650489                                                                                      |
| License date                 | Dec 08, 2022                                                                                       |
| Licensed Content Publisher   | Elsevier                                                                                           |
| Licensed Content Publication | Applied Surface Science                                                                            |
| Licensed Content Title       | Au nanoparticle arrays produced by Pulsed Laser Deposition for Surface Enhanced Raman Spectroscopy |
| Licensed Content Author      | N.R. Agarwal,F. Neri,S. Trusso,A. Lucotti,P.M. Ossi                                                |
| Licensed Content Date        | Sep 15, 2012                                                                                       |
| Licensed Content Volume      | 258                                                                                                |
| Licensed Content Issue       | 23                                                                                                 |
| Licensed Content Pages       | 5                                                                                                  |
| Start Page                   | 9148                                                                                               |
| End Page                     | 9152                                                                                               |

|                                              |                                                                                                                                           |
|----------------------------------------------|-------------------------------------------------------------------------------------------------------------------------------------------|
| Type of Use                                  | reuse in a thesis/dissertation                                                                                                            |
| Portion                                      | figures/tables/illustrations                                                                                                              |
| Number of figures/tables/illustrations       | 1                                                                                                                                         |
| Format                                       | both print and electronic                                                                                                                 |
| Are you the author of this Elsevier article? | No                                                                                                                                        |
| Will you be translating?                     | No                                                                                                                                        |
| Title                                        | Performance Assessment of Au SERS Substrates Prepared by Deposition of Au Nanoparticles on Screen-Printed SiO <sub>2</sub> Particle Films |
| Institution name                             | Ontario Tech University                                                                                                                   |
| Expected presentation date                   | Jan 2023                                                                                                                                  |
| Portions                                     | Fig. 4. SERS spectra of Rhodamine 6G obtained by Au substrates deposited at 100 Pa (top) and commercial substrates (bottom)               |
| Requestor Location                           | Ontario Tech University<br>2000 Simcoe St North<br><br>Oshawa, ON L1G 0C5<br>Canada<br>Attn: Ontario Tech University                      |
| Publisher Tax ID                             | GB 494 6272 12                                                                                                                            |
| Total                                        | 0.00 CAD                                                                                                                                  |
| Terms and Conditions                         |                                                                                                                                           |

**Figure 1.12.** SERS Spectra of R6G ( $10^{-6}$  M) on different substrates coated with and without Au. Red: Granular Au-sputtered horizontally aligned multiwalled carbon nanotube (Au-HA-CNT) (3000 nm x 50 nm). Reprinted from Nanotechnology, X. N. He, Y. Gao, M. Mahjouri-Samani, P. N. Black, J. Allen, M. Mitchell, et al., *Surface-enhanced Raman spectroscopy using gold-coated horizontally aligned carbon nanotubes*, **23**, p. 205702, 30 April 2012; <http://dx.doi.org/10.1088/0957-4484/23/20/205702> © IOP Publishing. Reproduced with permission. All rights reserved

**Marketplace**

This is a License Agreement between Raquel E. Simpson/Ontario Tech University ("User") and Copyright Clearance Center, Inc. ("CCC") on behalf of the Rightsholder identified in the order details below. The license consists of the order details, the Marketplace Order General Terms and Conditions below, and any Rightsholder Terms and Conditions which are included below.

All payments must be made in full to CCC in accordance with the Marketplace Order General Terms and Conditions below.

|                  |             |                   |                                    |
|------------------|-------------|-------------------|------------------------------------|
| Order Date       | 08-Dec-2022 | Type of Use       | Republish in a thesis/dissertation |
| Order License ID | 1298863-1   | Publisher Portion | IOP Publishing                     |
| ISSN             | 0957-4484   |                   | Chart/graph/table/figure           |

**LICENSED CONTENT**

|                   |                                      |                  |                                                      |
|-------------------|--------------------------------------|------------------|------------------------------------------------------|
| Publication Title | Nanotechnology                       | Country          | United Kingdom of Great Britain and Northern Ireland |
| Author/Editor     | Institute of Physics (Great Britain) | Rightsholder     | IOP Publishing, Ltd                                  |
| Date              | 01/01/1990                           | Publication Type | Journal                                              |
| Language          | English                              |                  |                                                      |

**REQUEST DETAILS**

|                                                        |                          |                             |                                  |
|--------------------------------------------------------|--------------------------|-----------------------------|----------------------------------|
| Portion Type                                           | Chart/graph/table/figure | Distribution                | Canada                           |
| Number of Charts / Graphs / Tables / Figures Requested | 1                        | Translation                 | Original language of publication |
| Format (select all that apply)                         | Print, Electronic        | Copies for the Disabled?    | No                               |
| Who Will Republish the Content?                        | Academic institution     | Minor Editing Privileges?   | No                               |
| Duration of Use                                        | Life of current edition  | Incidental Promotional Use? | No                               |
| Lifetime Unit Quantity                                 | Up to 499                | Currency                    | CAD                              |
| Rights Requested                                       | Main product             |                             |                                  |

**NEW WORK DETAILS**

|                 |                                                                                                                                           |                            |                         |
|-----------------|-------------------------------------------------------------------------------------------------------------------------------------------|----------------------------|-------------------------|
| Title           | Performance Assessment of Au SERS Substrates Prepared by Deposition of Au Nanoparticles on Screen-Printed SiO <sub>2</sub> Particle Films | Institution Name           | Ontario Tech University |
| Instructor Name | Raquel E. Simpson                                                                                                                         | Expected Presentation Date | 2023-01-11              |

**ADDITIONAL DETAILS**

|                        |     |
|------------------------|-----|
| Order Reference Number | N/A |
|------------------------|-----|